High-Efficiency Solar Fuel Devices: Protection and Light Management Utilizing TiO_2

Thesis by

Erik Verlage

In Partial Fulfillment of the Requirements for the
degree of
Doctor of Philosophy

CALIFORNIA INSTITUTE OF TECHNOLOGY
Pasadena, California

2017
(Defended May 9th, 2017)

© 2017

Erik Verlage
ORCID: 0000-0001-5940-0859

All rights reserved

ACKNOWLEDGEMENTS

First and foremost I would like to thank my advisor, Prof. Harry Atwater. Since I first met him I have been impressed by his positive outlook and his passion for scientific research. He has overseen my personal and professional growth, and has always been enthusiastically supportive of me and every person in his research group. He is my role model for how to be a good mentor and leader.

I would also like to thank Professors Harry Gray, Nathan Lewis, and William Johnson for serving on my thesis committee. I truly appreciate their time and expertise.

I have gained much help and knowledge from Dr. Ke Sun, who is one of the most kind and hard-working researchers I have ever known. I relied heavily on his knowledge and advice through most of my time in the lab. Early in my research, I benefited tremendously from collaborating with Prof. Shu Hu. Without his help and his breakthrough with the ALD-TiO_2 protection scheme, I would not have been able to complete the work in this thesis. Another huge influence on my research was Dr. C.X. Xiang, who guided me through many hurdles and organized many of the collaborations I enjoyed.

I want to further thank Professors Nathan Lewis and Carl Koval for their roles as directors of JCAP, and for their invaluable electrochemistry lectures. All of the members of JCAP that I worked with through the years deserve my thanks, including Josh Spurgeon, Chris Karp, Matt Shaner, Matt McDowell, Andrew Leenheer, Charles McCrory, Joachim Lewerentz, Ragip Pala, Kate Fountaine, Sonja Francis, Marika Letilly, Rui Liu, Ryan Jones, my SURF Alec Ho, Ivan Moreno-Hernandez, Michael Lichterman, Chance Crompton, Matthias Richter, Teddy Huang, Joel Ager, Ian Sharp, Slobodan Mitrovic, Kyle Cummins, Dan Torelli, John Gregoire, Jesus Velazquez, Ivonne Ferrer, Will Royea, Xenia Amashukeli, Jack Baricuatro, and Manuel Soriaga. I also want to acknowledge Darius Siwek, who provided artwork for the solar fuels prototype that appeared on the front cover of our EES publication.

I will have fond memories of the Atwater group, and all of the group members I overlapped with during my time at Caltech, including Christopher Flowers, Dan Turner-Evans, Emily Kosten, Hal Emmer, Chris Chen, Carissa Eisler, Emily Warmann, Rebecca Saive, Dagny Fleischman, Colton Bukowski, Phil Jahelka, Sophia Cheng, Siying Peng, Yulia Tolstova, Amanda Shing, and many more. I was also

very grateful to Ali for keeping the Atwater group labs running smoothly, and for access to his PDMS lab.

I want to thank the wonderful administrators: Christy Jenstad, Jennifer Blankenship, Tiffany Kimoto, Elizabeth Jennings, Lyann Lau, Susan Fuhs, Julianne Just, and Mabby Howard. Your hard work makes all of our research possible.

I am grateful to my office mates for providing a fun work environment. Stefan Omelchenko for keeping me honest and on task, even if it meant I lost a bet or two. Kimberly Papadantonakis for her guiding hand through JCAP research. Sisir Yalamanchili for helping out with much of the fabrication and being a very easygoing lab partner. Paul Nunez and Azhar Carim for many entertaining conversations. Xinghao Zhou, Jingjing Jiang, Fan Yang, and the hilarious friend from across the pond Billy Hale, for livening up the Jorgensen office.

Lastly, I want to thank my friends and family. My productivity group kept me focused and on task. Sunita Darbe, Sam Johnson, and Jackie Villadsen, I enjoyed your company immensely. I want to thank Renee McVay for being my piano/violin partner in our duets as the String Theorists. Fadl Saadi for being hillarious and agreeing to be a part of the webseries. Andrew Hoff for being an excellent roommate. Kevin Fiedler for many lunchtable discussions. John Lloyd and Saurabh Bajaj for countless rounds of squash. Nicolas Batara for being my gym buddy and keeping me fit and healthy. Max Jones, Mark Harfouche, and Ivan Papusha for the many outings and events. Evan Miyazono and Jeremy Brouillet for challenging games of Go. Michael Burd for many puzzling riddles. Max Murialdo for attending our poker nights. I also want to thank Dr. Amanda Cassil for being a great resource and encouraging me to pursue my dream career. From the bottom of my heart I thank my siblings Alex and Megan, my girlfriend Midori Shibuya, and my parents, for their unwavering support and for the love they have shown me through all the years. I would not have made it without you.

ABSTRACT

Global climate change coupled with increasing global energy consumption drives the need for renewable and carbon-neutral alternatives to fossil fuels. Photoelectrochemical devices store solar energy in chemical bonds, and have the potential to provide cost-effective fuel for grid-scale energy storage as well as to serve as a feedstock for the production of carbon-neutral transportation fuels. A widely recognized goal is the demonstration of a monolithically-integrated solar-fuels system that is simultaneously efficient, stable, intrinsically safe, and scalably manufacturable. This thesis presents the development of three separate high-efficiency solar fuel devices protected by thin films of amorphous TiO_2, and develops light management strategies to increase the performance of these devices.

First, high-efficiency monolithic cells were designed to perform solar water-splitting and CO_2 reduction. These designs are driven by high-quality single-crystalline III-V semiconductors that are unstable when placed in direct contact with aqueous electrolytes but can be protected against corrosion by hole-conducting amorphous films. Experimental fabrication and characterization of this tandem device was realized in the form of a fully-integrated water-splitting prototype with a solar-to-hydrogen efficiency of 10% showing stability for over 80 hours of operation. This was followed by the demonstration of water-splitting and CO_2 reduction devices enabled by bipolar membranes, which increased stability and alleviated materials-compatibility constraints by creating a pH difference between the anolyte and catholyte, maintained at steady-state. Finally, universal light management strategies were developed using high-aspect-ratio TiO_2 nanocones, resulting in an increase in catalyst loading with ultrahigh broadband transmission.

PUBLISHED CONTENT AND CONTRIBUTIONS

The work in this thesis has been drawn from the following publications:

- Verlage, E., Hu, S., Liu, R., Jones, R. J. R., Sun, K., Xiang, C., Lewis, N. S. & Atwater, H. A. A monolithically integrated, intrinsically safe, 10% efficient, solar-driven water-splitting system based on active, stable earth-abundant electrocatalysts in conjunction with tandem III-V light absorbers protected by amorphous TiO_2 films. *Energy & Environmental Science* **8,** 3166–3172 (2015).
  DOI: 10.1039/C5EE01786F
  Contribution: conception and design, data collection, data analysis and interpretation, manuscript drafting and revision.

- Sun, K., Liu, R., Chen, Y., Verlage, E., Lewis, N. S. & Xiang, C. Solar-Driven Water Splitting: A Stabilized, Intrinsically Safe, 10% Efficient, Solar-Driven Water-Splitting Cell Incorporating Earth-Abundant Electrocatalysts with Steady-State pH Gradients and Product Separation Enabled by a Bipolar Membrane. *Advanced Energy Materials* **6,** 1600379 (2016).
  DOI: 10.1002/aenm.201670077
  Contribution: experimental design, III-V photoelectrochemical cell design and processing.

- Zhou, X., Liu, R., Sun, K., Chen, Y. K., Verlage, E., Francis, S. A., Lewis, N. S. & Xiang, C. X. Solar-Driven Reduction of 1 atm of CO_2 to Formate at 10% Energy-Conversion Efficiency by Use of a TiO_2-Protected III–V Tandem Photoanode in Conjunction with a Bipolar Membrane and a Pd/C Cathode. *ACS Energy Letters* **1,** 764–770 (2016).
  DOI: 10.1021/acsenergylett.6b00317
  Contribution: III-V photoelectrochemical cell design and processing.

Content from the following publications has been referenced where appropriate:

- Sun, K., Kuang, Y., Verlage, E., Brunschwig, B. S., Tu, C. W. & Lewis, N. S. Functional Coatings: Sputtered NiO_x Films for Stabilization of p^+n-InP Photoanodes for Solar-Driven Water Oxidation. *Advanced Energy Materials* **5,** 1402276 (2015).
  DOI: 10.1002/aenm.201570059
  Contribution: data collection and analysis.

- Saadi, F. H., Carim, A. I., Verlage, E., Hemminger, J. C., Lewis, N. S. & Soriaga, M. P. CoP as an Acid-Stable Active Electrocatalyst for the Hydrogen-Evolution Reaction: Electrochemical Synthesis, Interfacial Characterization and Performance Evaluation. *The Journal of Physical Chemistry C* **118,** 29294–29300 (2014).
  DOI: 10.1021/jp5054452
  Contribution: data collection and analysis.

TABLE OF CONTENTS

LIST OF ILLUSTRATIONS

LIST OF TABLES

NOMENCLATURE

η_{STF}. solar to fuel efficiency.

η_{STH}. solar to hydrogen efficiency.

f_c. geometric catalytic filling fraction.

E_g. band gap energy.

J_{sc}. short-circuit current density.

V_{oc}. open-circuit voltage.

AEM. anion-exchange membrane.

ALD. atomic layer deposition.

AM1.5. air mass 1.5 solar spectrum.

ARC. anti-reflection coating.

BPM. bipolar membrane.

CEM. cation-exchange membrane.

CO_2R. carbon dioxide reduction.

CV. cyclic voltammetry.

EQE. external quantum efficiency.

FF. fill factor.

HER. hydrogen evolution reaction.

IPA. poly(isopropyl alcohol).

KOH. potassium hydroxide.

MOCVD. metal-organic chemical vapour deposition.

n^{++}. degenerately-doped n-type material.

n^{+}. highly-doped n-type material.

OER. oxygen evolution reaction.

p^{++}. degenerately-doped p-type material.

p^{+}. highly-doped p-type material.

PEC. phtoelectrochemical.

PMMA. poly(methyl methacrylate).

PV. photovoltaic.

SCE. saturated calomel electrode.

SEM. scanning-electron microscopy.

TDMAT. tetrakis(dimethylamido)titanium.

Chapter 1

INTRODUCTION TO SOLAR FUEL DEVICES

Sunlight is an abundant renewable energy resource. However, there is a large mismatch between the availability of sunlight and peak demand for the electrical power grid. This requires efficient energy storage to enable large-scale power generation using photovoltaic solar panels. Photoelectrochemical (PEC) cells convert energy from the sun into chemical fuel, which can be stored and used on demand.

A fully-integrated photoelectrochemical water-splitting device that efficiently produces hydrogen directly from sunlight would provide a scalable, sustainable source of energy that can be used for grid storage as well as the transportation sector. In such a system all components must safely operate under mutually compatible conditions. Furthermore, a half-cell that performs water oxidation could also be used for the photoelectrochemical reduction of CO_2, opening up a variety of fuel products that can be used for energy storage.

The following chapter is an introduction to the basics of solar water splitting, and provides motivation for the creation of integrated, high-efficiency, III-V solar fuel devices that are intrinsically safe, operate in extreme pH, and use highly-active earth-abundant electrocatalysts.

1.1 Solar Fuels

The direct production of fuels from sunlight could provide scalable grid storage that would offset the intermittent nature of renewable energy sources like wind and photovoltaics. PEC systems require the following: light-absorbing materials, fuel-forming electrocatalysts, an electrolyte, and an ability to perform product separation. These materials must operate together under mutually compatible conditions, and the highest performing components cannot necessarily be combined to create a viable and efficient device [1]. In addition, there are many viable device architectures for the production of fuel from sunlight [2].

Hydrogen produced via solar water splitting has been viewed as a viable means of renewable energy production that can be used to power sources in homes, as a feedstock for industrial processes, and as fuel for transport to realize a sustainable hydrogen economy [3].

The multielectron reduction of CO_2 to a liquid fuel, while more challenging than water splitting, also promises to produce energy-dense fuels from sunlight that would be particularly useful for the transportation sector [4]. Liquid fuel requirements for ships, aircraft, and heavy-duty trucks create 40% of the current global transportation fuel demand [4], and a renewable alternative could have a significant impact on fossil fuels emissions.

Solar fuel devices for solar water splitting and CO_2 reduction must be efficient, stable, cost-effective, and intrinsically safe for scalable deployment in order to demonstrate commercial viability.

1.2 Solar-Driven Water Splitting

The production of H_2(g) from water and sunlight requires the electrolysis of water, and **Equation 1.1** shows the water-splitting reaction

$$H_2O \rightarrow H_2 + \frac{1}{2}O_2 \tag{1.1}$$

which can be separated into two half reactions. In acidic conditions this is

$$4H^+ + 4e^- \rightarrow 2H_2 \tag{1.2}$$

$$2H_2O \rightarrow O_2 + 4H^+ + 4e^- \tag{1.3}$$

and in alkaline conditions, these half reactions become

$$4H_2O + 4e^- \rightarrow 2H_2 + 4OH^- \tag{1.4}$$

$$4OH^- \rightarrow O_2 + 2H_2O + 4e^- \tag{1.5}$$

Equations 1.2 and **1.4** are referred to as the hydrogen evolution reaction (HER), and correspondingly **Equations 1.3** and **1.5** are the oxygen evolution reaction (OER).

To create a semiconductor device that performs unassisted solar water splitting, the band edges of the semiconductors must straddle the electrochemical potentials E° (H^+/H_2) and E° (O_2/H_2O) in order to deliver holes and electrons to catalytic surfaces that simultaneously drive the HER and OER. As shown in **Figure 1.1** , this can be accomplished using two p-n PV junctions in series that form a photovoltaic-biased electrosynthetic cell.

An idealized three-electrode measurement of the current-potential characteristics of water electrolysis is shown in **Figure 1.2** (green curve). Anodic current (+)

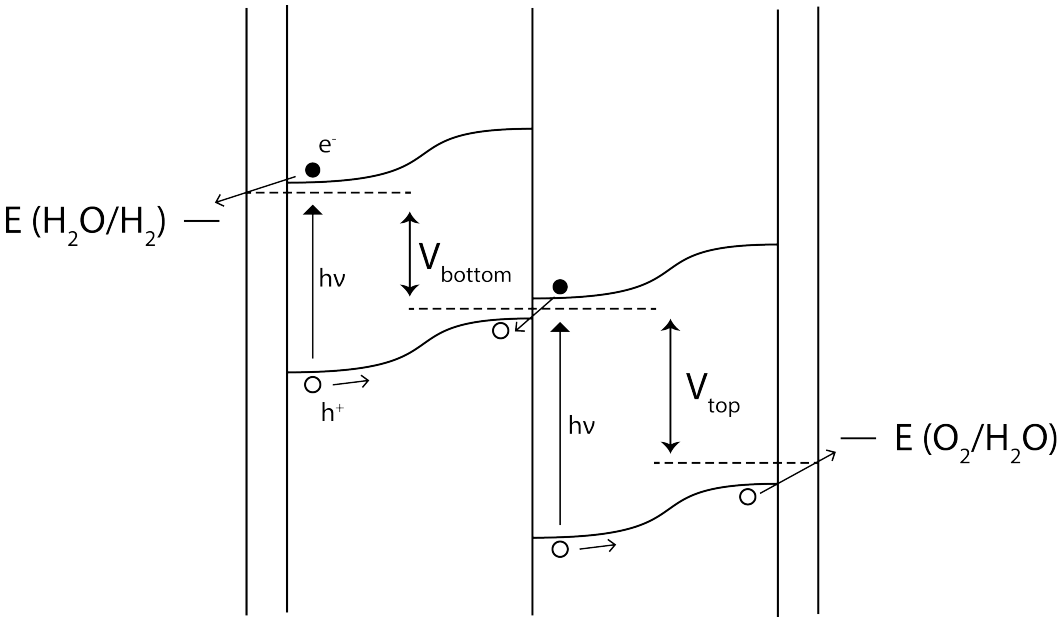

Figure 1.1: Energy diagram for a tandem photovoltaic-biased electrosynthetic cell. Electron energy (in eV) increases in the ordinate vertically. Photons absorbed in the semiconductor excite electron-hole pairs, with holes moving from the cathodic surface (left) to the anodic surface (right) of the device.

drives the OER, and, in the presence of dissolved O_2(g), reductive current (-) drives the oxygen reduction reaction (ORR). When combined with a solid state device to form a photovoltaic-biased electrosynthetic cell, also shown in **Figure 1.2** (purple curve), the energy barrier created by the ideal diode behavior prevents hole conduction to the surface, and OER does not occur in the dark. Upon illumination, the diode behavior shifts upward due to photoexcited carriers (cyan curve in **Figure 1.2**), and anodic current drives the OER. It is important to note that the onset potential for the OER at the surface of the device does not change, it is the voltage drop across the semiconductor device that creates the shift in measured potential.

To extract the solid-state photovoltaic I-V behavior (dashed curve), load-line analysis can be performed using a simplified equivalent circuit . The electrochemical load for the device (green) can be subtracted from the, gives the dashed curve in **Figure 1.2** which can give the photovoltaic parameters of the buried junctions including open-circuit voltage (V_{oc}), short-circuit current density (J_{sc}), and fill factor (FF).

The production of H_2(g) fuel is subject to the constraints imposed by the minimum voltage requirements needed to sustain water-splitting. On top of thermodynamic requirements to drive the reaction, there are charge separation and reaction

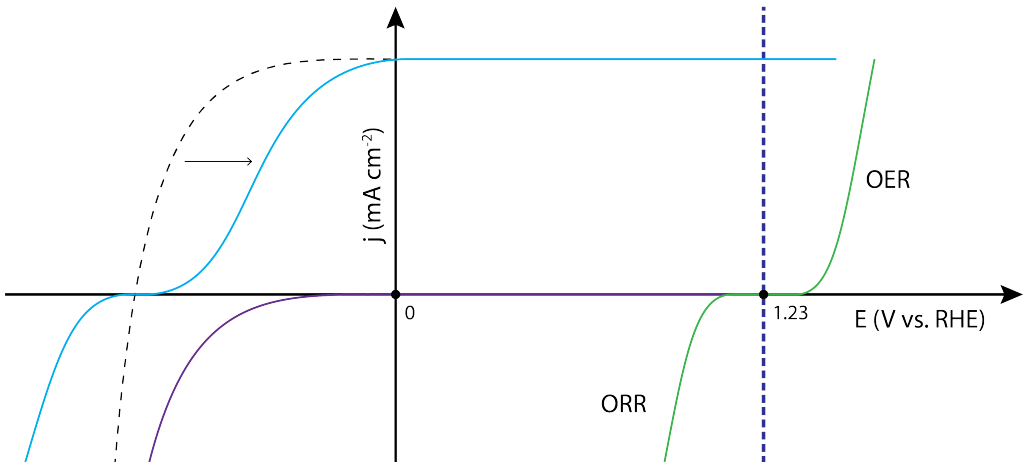

Figure 1.2: Oxygen evolution for an photovoltaic-biased electrosynthetic cell in the dark (purple) and under illumination (cyan). Anodic current drives the oxygen evolution reaction (OER), and cathodic current drives the oxygen reduction reaction (ORR). The electrochemical load of water splitting (green) has an onset for the OER at the expected electrochemical potential E° (O_2/H_2O) at 1.23 V vs. RHE. The solid-state photovoltaic I-V behavior (dashed curve) can be derived using load line analysis.

overpotentials, as well as entropic losses in the device. The conversion efficiency for solar water splitting devices is calculated using the thermodynamic requirement of 1.23 eV to perform water electrolysis. This solar-to-hydrogen efficiency is defined as:

$$\eta = \frac{\text{voltage} \times \text{current density}}{\text{total input power}} \tag{1.6}$$

$$\eta_{STH} = \frac{1.23\ (\text{V}) \times j_{op}\ (\text{mA cm}^{-2})}{S_{tot}\ (\text{mW cm}^{-2})} \tag{1.7}$$

where j_{op} is the operating short-circuit current density, and S_{tot} is the total incident solar irradiance.

1.3 Operational Criteria for Safe, Efficient Electrolyzers

Commercial electrolyzers must meet several criteria to be considered safe and reliable for operation and sale into the marketplace. They must be intrinsically safe, and not produce a flammable, potentially explosive mixture of H_2(g) and O_2(g) in the reactor at any point in space or time, especially because the reactor contains active catalysts for the recombination of the gases and is operating in the presence of light and heat. Electrolyzers must be able to withstand pressure differentials without undesirable crossover of gases or flooding and flow of the liquid electrolyte across

the membrane separator, because the stoichiometry of the evolved H_2 and O_2 is 2:1. The membrane must be able to hold back pressure because a pressure differential is required to beneficially collect the H_2(g) in a pipeline, as opposed to evolving the gas at atmospheric pressure in a laboratory demonstration device.

1.4 Discrete Photovoltaic / Electrolyzer Systems

One approach to solar-driven hydrogen production involves use of photovoltaic (PV) panels, modules or cells connected physically and electrically in series with an electrolyzer. For a combined photovoltaic/electrolyzer system, efficiency is calculated using the efficiency of the individual components, as shown in **Equation 1.8** .

$$\eta_{STH} = \eta_{PV} \times \eta_{electrolyzer} \tag{1.8}$$

Commercial electrolyzers typically are designed to operate at 70% efficiency [5–8]. To obtain optimal impedance matching in view of hourly, daily and seasonal variability in the solar irradiance, a dynamic DC-to-DC converter, with an estimated efficiency of 85%, would be used to connect the electrolyzer to the PV unit. Therefore a solar-to-hydrogen efficiency based on any specific PV + electrolyzer system can be estimated by taking the peak PV efficiency and multiplying by ~0.60 [9]. Thus, peak system efficiencies of 12.6% and 24.6%, respectively, could be obtained by use of an electrolyzer in conjunction with a high-efficiency (21%) Si PV module or a high-efficiency (41%) III-V triple junction PV operated under optical concentration [9]. Such systems have been demonstrated at commercial scale, laboratory scale, and research scale [10–17]. For example, Si PV mini-modules and perovskite-based solar cells, respectively, have been used recently in the PV + electrolyzer configuration[11, 12]. Significant advances include series interconnected $CuIn_xGa_{1-x}Se_2$ (CIGS) absorbers in conjunction with two Pt electrodes in 3.0 M H_2SO_4(aq) with a solar-to-hydrogen efficiency η_{STH} > 10% [10], and a bismuth vanadate photoanode in combination with a thin-film silicon solar cell has produced η_{STH} = 5.2% [18]. At the commercial level, the high balance of systems cost and low capacity factor of stand-alone PV-electrolyzer systems results in high levelized hydrogen costs relative to hydrogen produced by steam reforming or grid electrolysis using fossil or low-carbon electricity [19].

1.5 Fully-Integrated Photoelectrochemical Water-Splitting Devices

Integrated solar-to-fuel devices provide many potential advantages relative to a discrete PV + electrolyzer system and offer a unique design space for the balance

of systems [1, 20–22]. Modeling and simulation has revealed a range of integrated device architectures that can allow for efficient operation and scalable deployment of solar-driven water splitting systems that can produce renewable H_2(g) as an energy carrier [22–28]. A compilation of reported devices [21] shows a wide range of efficiency, integration, and stability. Many monolithically integrated solar-driven water-splitting devices based on tandem structures or triple junctions have been described previously [21]. Some of those devices are compatible with operation in an efficient, intrinsically safe system.

"Wireless" monolithically integrated photoelectrochemical water-splitting devices were reported in 1977 using platinized $SrTiO_3$ [29]. However, the band gaps, E_g, of $SrTiO_3$ and related metal oxides are too large to allow for highly efficient use of the solar spectrum [30]. Smaller band gap materials are generally unstable to photocorrosion in aqueous solutions, and need to be protected, generally with coatings of transparent, conductive oxides (TCO), to provide stable operation [31–34].

TCO-coated amorphous hydrogenated Si (a-Si:H) triple junction structures have been widely explored in monolithically integrated water-splitting systems in which the photoelectrode, protection layer(s), and electrocatalytic species share a common optical path [35–37]. Use of a-Si:H triple junctions in monolithically integrated structures protected by TCOs, in conjunction with either Pt or with earth-abundant electrocatalysts for the hydrogen-evolution reaction (HER) and oxygen-evolution reaction (OER), have yielded solar-to-hydrogen efficiencies of up to 5% [35]. In monolithically integrated solar-fuels devices, tandem structures can provide significantly higher efficiencies than triple junctions [38].

Near-neutral devices

Both modeling/simulation results and experimental data have shown that electrolyzers operated in solutions buffered to near-neutral pH are inefficient and/or not intrinsically safe. For example, operation of a membrane-free near-neutral pH a-Si:H device with ITO protective layers and earth-abundant, high overpotential electrocatalysts at η_{STH} = 3.2% produced 10% O_2(g) in the cathode chamber and up to 40% H_2(g) in the anode chamber, presenting an explosion hazard [39]. Introduction of a membrane was shown to yield a large reduction in the system efficiency and resulted in significant pH gradients near the electrode surfaces. Further modeling and simulation has shown that steady-state operation in such a geometry even in

buffered solutions will result in pH gradients between the anode and cathode that produce local pH changes near the electrode surfaces, due to the consumption of protons associated with evolution of H_2(g) from water and concomitant production of protons associated with production of O_2(g) from H_2O [39, 40]. The overpotentials associated with the pH gradients and electrodialysis exceeded the combined overpotentials associated with the oxygen-evolving and hydrogen-evolving electrocatalysts, precluding the construction of an efficient (photo)electrolysis system. Further modeling and simulation efforts have shown that active convection by bubble evolution, for example, can minimize the formation of pH gradients but results in the loss of intrinsic safety, due to the concomitant co-evolution of stoichiometric, potentially explosive, mixtures of H_2(g) and O_2(g) at atmospheric pressure in the reaction vessel, in the presence of active catalysts for the recombination of these gases as well as in the presence of light and heat [40].

Triple junction a-Si:H devices, protected by ITO on one side in conjunction with phosphate-containing Co oxide as an OER electrocatalyst [41–44] and on the other side by stainless steel in conjunction with a Ni–Mo–Zn HER catalyst, yielded η_{STH} = 1.75–2.5% for 10 h in aqueous solutions buffered to pH = 9 with borate [41]. The combined HER and OER overpotentials of the electrocatalysts at 10 mA cm^{-2} of current density exceeded 1 V [45], and the OER catalyst delaminated from the electrode at current densities of <10 mA cm^{-2} [46, 47], precluding construction of robust, efficient monolithically integrated devices. Moreover, such devices co-evolve stoichiometric mixtures of hydrogen and oxygen gas, precluding intrinsically safe operation.

When a cation-exchange or anion exchange membrane is included in the system, severe pH gradients and electrodialysis of the solution occurs. These effects are a consequence of the low transference number [48] at near-neutral pH of protons or hydroxide ions across the membrane, relative to the transference number of other, higher concentration, charge-carrying ions in the buffered solution [39, 40]. In the absence of a membrane and with adequate convection of the electrolyte, the losses due to electrodialysis and ohmic resistance can be minimized, but potentially explosive mixtures of H_2(g) and O_2(g) are produced over active catalysts for recombination of the gases, in the presence of light and heat. Thus, electrolysis or photoelectrolysis systems that are operated in buffered or unbuffered bulk near-neutral pH electrolytes are inefficient and/or not intrinsically safe [23, 39, 40, 49].

Integrated devices operating in extreme pH

Integrated water-splitting devices that utilize a single electrolyte need to operate in extreme pH, as the unity transference number for protons or hydroxide ions in cells that include a CEM or an AEM in strongly acidic or strongly alkaline electrolytes (pH 0 or 14) minimizes the voltage lost due to resistance, pH gradients, and electrodialysis.

For example, a-Si:H triple junction devices, with RuO_2 on a Ti substrate used for the OER and Pt islands deposited directly onto the a-Si:H as the HER catalyst, have been used to split water in 1.0 M H_2SO_4(aq) [35]. Those devices exhibited steady-state η_{STH} = 5% over >4 h of operation. Triple-junction and quadruple-junction a-Si:H devices, coated with Pt as a HER catalyst and RuO_2 as an OER catalyst, have yielded η_{STH} = 2.6% in 5.0 M H_2SO_4(aq) [36, 37]. Such structures would benefit by the use of more advanced a-Si:H triple junction structures [50] that could produce higher current densities at the ~1.7 V optimal operating voltage that results from the relatively low combined HER and OER overpotentials of Pt in 1.0 M H_2SO_4(aq) at 10 mA cm^{-2} of current density [51]. Such devices have the capability of being incorporated into intrinsically safe systems because the transference number of protons in acidic media is essentially unity across gas blocking, cation-exchange membranes such as Nafion [52]. Monolithically integrated a-Si:H devices, protected on one side by ZnO in conjunction with a Co-Mo HER catalyst, and protected on the other side by SnO_2 in conjunction with an Fe–NiO_x OER catalyst, have yielded η_{STH} = 2.5–3.0% in 1.0 M KOH(aq), with stability for >18 h of operation [53]. Such devices also have the capability of operating in intrinsically safe systems, due to the essentially unity transference numbers of hydroxide ions across anion exchange membranes in alkaline media. In 1.0 M KOH(aq), the combined HER and OER Ni-based catalyst overpotentials are <0.5 V at 10 mA cm^{-2} of current density [51]. Hence relatively high efficiency systems can potentially be achieved through improvements in the performance of the light absorber, especially in conjunction with the Ni islands on protective TiO_2 films deposited by ALD. Indeed, prior attempts to fabricate monolithically integrated solar-driven water-splitting devices and systems based on a-Si:H triple junctions in 1.0 M KOH(aq) failed due to the lack of a suitable, stable protective anode coating [41, 54, 55].

Operation in aqueous alkaline electrolytes allows the construction of efficient, intrinsically safe systems and allows use of highly active, low overpotential, earth-abundant electrocatalysts based on Ni and related alloys [51]. In accord with

established properties of commercial electrolyzers, an intrinsically safe electrolysis or photoelectrolysis system does not produce a flammable, potentially explosive mixture of H_2(g) and O_2(g) in the reactor at any point in space or time. Common TCO's, such as indium tin oxide (ITO), are not stable in alkaline electrolytes [41, 54].

Efficient III-V photoelectrochemical devices

GaAs and other III-V semiconductors are ideal materials for photovoltaic and photoelectrochemical energy conversion. Many III-Vs have a direct band gap, can be epitaxially grown to produce high-quality single crystals, and can be passivated by other epitaxial III-V materials in the same growth. Single-crystalline thin films of these materials can provide a wide range of band gaps, and thus voltages, for incorporation into a PEC device, a crucial advantage in solar fuel generation. Because catalyst performance can dramatically change the overpotential needed to drive fuel-forming electrochemical reactions, voltage requirements for water electrolysis and CO_2 reduction systems can change dramatically when a complete prototype is assembled. For the large variety in voltage demands, tunable band gaps ensure optimized device performance over a range of architectures and materials.

For example, a photovoltaic-biased photoelectrosynthetic device based on a III–V tandem structure has exhibited 12.4% solar-to- hydrogen conversion efficiency, η_{STH}, under concentrated solar illumination [56]. However, III-V semiconductors are thermodynamically unstable under operating conditions and, without protection, undergo self-corrosion in alkaline and acidic environments [57]. The design of the III-V layer stack must account for t operation in solution. The III–V semiconductors photocorrode both under hydrogen-evolution reaction (HER) and oxygen–evolution reaction (OER) operating conditions [56–58], and therefore require protection to be utilized in such applications.

Tandem structures based on on InGaP/GaAs structures, but where the InGaP is exposed to the electrolyte as a photocathode, in conjunction with Pt/Ru and Pt as HER and OER electrocatalysts, respectively, have been used to produce monolithically integrated solar-driven water-splitting devices in 1.0 M H_2SO_4(aq) or in >1 M KOH(aq) [59]. Such devices yielded η_{STH} = 4–6% under ~11 sun illumination [59], whereas related structures based on a two-electrode photoelectrosynthetic cell configuration have yielded η_{STH} = 12.4% under 11 suns of concentrated illumination for <20 h of operation in 1.0 M H_2SO_4(aq) [56]. Another option for surface

protection of III-V tandems that has been the chemical and photoelectrochemical surface transformation of AlInP window layers using an aqueous solution of RhCl that serves to deposit Rh catalyst and to prevent corrosion of the underlying substrate [60]. This system decayed rapidly over time, decreasing steadily from η_{STH} = 17% to half of that performance over 40 hours [60]. The stability of these systems is limited due to cathodic decomposition processes characteristic of III–V materials in aqueous electrolytes [57].

Protection of III–V materials as photoanodes has also been a valuable and unrealized objective. Such devices are well-suited for use in efficient, intrinsically-safe water-splitting systems, and increases in the stability of such devices will require the development of robust protective coatings that are compatible with operation in aqueous acidic media, and/or the use of the protection schemes.

1.6 Devices for the Reduction of CO_2

CO_2 reduction (CO_2R) involves very different optimal electrolyte conditions than water-splitting reactions. Electrocatalysts for CO_2R have been developed mainly for near-neutral pH values [61, 62]. In alkaline conditions, the low concentration of dissolved CO_2 imposes severe mass-transport limitations for the cathodic CO_2R reaction, while in acidic conditions the high proton concentration favors H_2(g) production. Currently the only efficient and selective operation of CO_2R catalysts in near-neutral pH and at high operating current densities (e.g. 101 mA cm^{-2}) involve the two-electron/two-proton reduction of CO_2 to produce either CO or formate. [61, 63–66].

Just as with the water-splitting cells described previously, the OER half-reaction is required to provide electrons and protons for the sustainable electrochemical reduction of CO_2 [4]. Mixed-metal oxides have been extensively studied in strongly alkaline conditions, with state-of-the-art catalysts exhibiting ~250-300 mV overpotentials at 10 mA cm^{-2} of anodic current density [51, 67]. In contrast, electrocatalysts for the OER in near-neutral electrolytes exhibit substantially larger overpotentials [51, 68] because the negatively charged hydroxide ion is more readily oxidized than a neutral water molecule, and because hydroxide is present in high concentration in alkaline solutions [69]. For this reason, laboratory demonstrations of solar-driven CO_2R devices at near-neutral pH values suffer substantial overpotential losses for the OER [64, 70–72]. A device that used a Au catalyst for CO generation in 0.5 M $NaHCO_3$(aq) electrolyte had a solar-to-fuel conversion efficiency (η_{STF}) of 6.5%

[64]. A polymeric Ru complex for formate generation in 0.1 M aqueous phosphate buffer achieved an $\eta_{STF} = 4.6\%$ [70]. However, in addition to increased efficiencies, a full solar-driven CO_2R device requires a robust means to separate the end products. To improve efficiencies in a sustainable device, transitioning the OER catalysts to extreme pH can resolve these overpotential losses, but will require anodic protection of semiconductors in solution.

1.7 Scientific Gap

For more than four decades, the cathodic and anodic protection of small-bandgap semiconductor electrodes for use in photoelectrochemical devices has been an important drive in the solar fuels community [31, 73]. Corrosion is an issue for many non-oxide semiconductors used in photoelectrochemistry, and depending on pH and potential, they exhibit either passivation, where the production of insoluble species on the exposed surface prevents further corrosion, or dissolution into surrounding medium. To date, all known non-oxide semiconductors are unstable during anodic oxygen evolution [31]. Stabilization of large-area photoelectrodes for operational lifetimes sufficient to allow practical or commercial deployment of an integrated solar fuel system requires defect-tolerant surface protection of semiconductor materials.

In order to protect high-quality single-crystalline semiconductors without changing their electrochemical properties for hole or electron transfer through the electrode-solution interface, many different strategies have emerged. Alternate redox couples have been added to the solution to allow a preferential electrode reaction rather than the dissolution of the semiconductor. Thin metal films have been deposited on the surface of the semiconductor, sometimes requiring constant cathodic current on the exposed III-V surface during operation for stability [56], a severe impairment for long-term stability with an intermittent energy source and the day-night cycle. Using large bandgap semiconductors like n-type TiO_2, SnO_2, and SrTiO, originally used as light absorbers in low-efficiency water-splitting devices for their stability during the photo-oxidation of water, is yet another strategy towards stable device architectures.

The challenge when utilizing protection schemes with large-bandgap materials that are stable under operating (and non-operating) conditions is band alignment with the underlying substrate, as well as surface conformity. Protection schemes that utilize CVD-deposited TiO_2 to protect photocathodic materials have been around

since the 1970s Kohl:1977, and recent advances have been made towards protecting III-Vs like InP for use in solar water splitting [74] and CO_2 reduction [75].

1.8 Protecting Semiconductors with Hole-Conducting TiO_2

The energy bands of TiO_2 , while aligned with the conduction band of InP and Si, has a large valence band offset that creates a tunneling barrier for photogenerated holes [76]. Previous attempts to create oxide protection layers for photoanodes relied on a tunneling mechanism for charge carrier transfer to solution, and thus underlying layers were prone to corrosion due to pinholes in the thin oxide films [34]. While TiO_2 has been used to protect semiconductors for water reduction by taking advantage of energy band alignments for electron transport through the conduction band [77], charge transfer for water oxidation was unexpected due to the large band gap offset between the protective film and the underlying semiconductor.

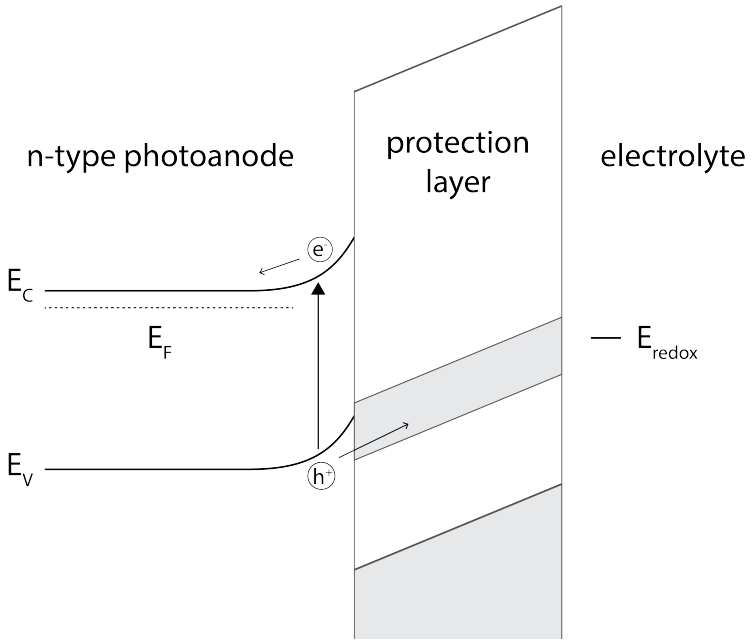

Figure 1.3: Hole conduction through a defect band within the protection layer band gap. Without this miniature band, the large mismatch in valence band energies between the photoanode and thick oxide protection layer would block hole conduction to the electrolyte.

Work performed at the Joint Center for Artificial Photosynthesis (JCAP) found conformal growth of thick TiO_2 via atomic layer deposition (ALD) can enable hole conduction through the oxide film [78], creating an opportunity for the construction of stable and highly efficient solar-fuel generators. An illustration of the hole conduction mechanism is shown in **Figure 1.3**, where a miniature band in the

protection layer explains the behavoir of these TiO_2-coated electrodes. One of the many advantages of using the ALD process is the conformal nature of the growth. The thickness of these films can be controlled very precisely, as each layer is assembled monolayer by monolayer. The deposition utilizes alternating gas phase chemical processes that are self-limiting, ensuring every exposed surface is covered uniformly during each step. This allows for conformal coating of not only planar films, but of any 3D structure, which enables the protection of many different cell architectures.

Figure 1.4: Corrosion of GaAs in 1.0 M KOH(aq) using a compression cell (top) and epoxied electrode (bottom) with and without an ALD-TiO_2 protection layer.

As can be seen in **Figure 1.4**, III-V materials that actively corrode under OER conditions in 1.0 M KOH can be successfully protected for long-term operation using amorphous TiO_2 films deposited using atomic-layer deposition (ALD). These films were shown to protect a variety of photoanode materials under operation in alkaline electrolytes including Si, GaAs, GaP, and CdTe [78–80]. This opens up a wide variety of high quality semiconducting materials that can be incorporated in devices that operate in alkaline conditions. While anodic protection is an important goal for stable water-splitting devices, it can also increase stability for a large variety of integrated devices. Any device that operates in aqueous environments with extreme

pH will also require anodic protection, regardless of the fuel that is produced on the cathodic surface. Many constraints on the fuel production, such as large catalytic overpotential requirements, are likely to interfere with light absorption, and would necessitate illumination from the anodic side of the device. A protection scheme that chemically passivates photoanodic surfaces designed for oxygen evolution in a solar-driven water-splitting device could be modified for use as the anodic component for other purposes, such as a CO_2 reduction device. Thus, demonstration of a device that incorporates a long-term stable photoanode opens up a wide number of architectures for solar fuel devices.

1.9 Contents of this Thesis

In this thesis the ALD-TiO_2 protection scheme is used to create highly efficient, stable, earth-abundant, intrinsically safe, and fully-integrated solar fuel prototypes that use high-quality III-V materials to perform unassisted solar water splitting and CO_2 reduction. Light management strategies are also developed to improve efficiencies of solar fuel devices, with potential use for a variety of optoelectronic technologies.

- In Chapter 2, two optimized III-V multijunction architectures are presented, and an MOCVD-grown high-quality InGaP/GaAs tandem cell is fabricated and characterized. Optical simulations lead to the design of a TiO_2 protective coating that serves as a single-layer antireflecion coating.
- In Chapter 3, this III-V design is used to create a monolithically integrated device for solar-driven water splitting in 1.0 M KOH(aq) to achieve record stability using the TiO_2 protective coating. A large area (1 cm^2) and intrinsically safe solar-hydrogen prototype system performed unassisted water splitting, and collection of H_2(g) and O_2(g) confirmed 100% faradaic efficiency.
- In Chapter 4, bipolar membranes are incorporated into PEC devices for solar water splitting and CO_2 reduction, enabling large pH gradients between anode and cathode compartments. This allows for the stable pairing of previously incompatible materials leading to increased efficiency and stability.
- In Chapter 5, the properties of dielectric waveguide structures for light trapping on planar PEC surfaces are explored. Two light management schemes are designed using TiO_2 nanocone arrays and double-layer antireflection coatings, and show broadband transmission through thick metal electrocatalysts.

Finally, the work is summarized and the directions for future research are discussed.

Chapter 2

DESIGN OF MONOLITHIC III-V LIGHT ABSORBERS FOR PEC DEVICES

2.1 Material Choices and Constraints

Light absorbing materials selected for use in monolithically stacked, efficient, fully integrated photoelectrochemical devices must meet three major material constraints. They must (1) be high quality semiconducting materials to facilitate light absorption and carrier collection, (2) have band gaps that are within the range of interest, and (3) be stable in the electrochemical environment during operation (if they are exposed to solution). While there has been extensive work on developing materials for use in solar fuel devices, there are currently no viable materials that meet all three of these requirements [1, 31]. To achieve long-term stability, fully integrated water-splitting prototypes have generally relied on stable but inefficient light-absorbing materials. These devices generally have large band gaps that supply excess voltage for the fuel-generating reaction, resulting in low current densities and low efficiencies.

The optimal band gaps for use in a tandem photoelectochemical cell will depend upon the geometry of the device and the performance of other components in the system. The device design in this chapter was motivated by a detailed-balance analysis of the Shockley–Queisser limits of light absorbers with a variety of bandgap combinations [81]. The iso-efficiency plots are derived from a model that accounted for light absorbers, filling fractions, electrocatalysts, solution electrolyte, and ion exchange membranes. Utilizing the highest performing earth-abundant electrocatalysts available (Ni-Mo HER and $NiFeO_x$ OER) and a 1.65/1.0 eV bandgap combination, devices can achieve an efficiency of η_{STH} = 28.5%. However, this is assuming ideal light absorption conditions, with 280 mV overpotential for the OER electrocatalyst at 10 mA cm^{-2}, and solution resistance of 5 ohm cm^{-2}. Any deviation from the ideal conditions presented in this analysis might fail to meet the voltage requirements to drive the water-splitting reaction, resulting in a sharp decrease in performance. A more achievable efficiency goal using earth-abundant electrocatalysts, accounting for realistic overpotential requirements from non-ideal materials, is a 1.8/1.2 eV bandgap combination with a maximum η_{STH} of 24%, assuming FF of 0.85, a non-optmized 560 mV overpotential for the OER electrocatalyst at 10 mA

cm^{-2}, and solution resistance of 5 ohm cm^{-2} [81].

Multijunction III–V compound semiconductor solar cells have been the dominant choice for high-efficiency photovoltaic devices. This material system displays excellent optical and electronic properties, and offers a wide array of bandgaps for use in multijunction devices that can be used to achieve the bandgap combination required for high-efficiency photoelectrochemistry.

Deposition of III-V materials

Once a material system is selected, many different deposition processes are available, each yielding varying quality semiconductor growths. Multi-crystalline films cut down on cell manufacturing costs, but majority and minority carrier recombination at grain boundaries limit conversion efficiencies. Single-crystalline films grown epitaxially using techniques like metal-organic chemical vapor deposition (MOCVD) produce higher quality semiconductor materials. To ensure single-crystalline growth and prevent the propagation of defects and dislocations through the epilayer, the semiconductor must be lattice-matched to the substrate.

Most III–V multijunction cells are grown epitaxially on either GaAs, Ge, or InP substrates. InGaP is a high-quality material often used as the top cell in triple-junction or dual-junction stacks, and control of atomic ordering in the InGaP layers provides a range of bandgaps from 1.78 to 1.9 eV. Another option is AlGaAs, which has a tunable bandgap that ranges from the 1.424 eV direct-gap GaAs to the indirect 2.12 eV AlAs bandgap, all with only a small deviation in lattice constant. For the lower bandgap, the elementary compostion of quaternary $In_xGa_{1-x}As_yP_{1-y}$ can be tuned to create a film of desired bandgap in the 0.74-1.34 eV range that is lattice-matched to InP. Alternatively, metamorphic growth of a InGaP/InGaAs tandem on a Ge substrate can yield 1.78/1.26 eV bandgaps if grown on a Ge substrate using stepgraded buffer layers to account for lattice mismatch of the epilayers [60].

Epitaxial liftoff of MOCVD-grown multijunction devices

One opportunity to decrease material costs of III-V MOCVD is to utilize epitaxial liftoff (ELO) to create thin film devices [82–84]. This process has multiple benefits over conventional MOCVD growth, and the company Alta Devices has utilized this new technology to create record-breaking thin film GaAs heterojunction solar cells while significantly reducing the cost of GaAs thin film photovoltaics.

After an initial seed layer, a thin, lattice-matched sacrificial layer is deposited

on the substrate. For growths on GaAs a layer with a high percentage of aluminum is chosen, such as AlAs (or $Al_xGa_{1-x}As$ with x > 0.3) that is selectively etched in hydrofluoric acid [84]. After post-treatment, this process allows reuse of the substrate wafer for additional epitaxial growths, which has the potential to dramatically cut down on fabrication costs by decreasing source wafer material.

This process also enables an increase in efficiency of the final device architecture. A more traditional multijunction cell grown on the (roughly index matched) substrate wafer only allows incident photons a single pass through the active device. Because the inactive substrate is hundreds of microns thick, any photons not absorbed in the first pass will be lost to the substrate. With thin films lifted off from the substrate, a back reflector or scattering surface can be used to increase the number of passes of incident light inside the cell, allowing increased absorption in thinner films and further reducing the material cost for the growth.

While ELO avoids many of the disadvantages of regular epitaxial growth, multijunction devices grown epitaxially on a single substrate have a limited range of available bandgaps for use in PEC devices. Inverted metamorphic multijunction (IMM) growths that use ELO can help alleviate the bandgap constraints [85]; for instance, an InGaP/(In)GaAs tandem cell can be grown epitaxially on GaAs using an AlAs sacrificial liftoff layer. The composition of InGaAs junctions can be controlled though the use of metamorphic buffers, allowing bandgaps that range in principle from 0.33 eV for InAs to 1.42 eV for GaAs. However, these designs must contend with losses in material quality of all lattice-mismatched materials due to the propagation of defects after the stepgraded buffer layer.

Direct wafer bonding of independent semiconductor devices

Ternary and quaternary III-V semiconductor growths on GaAs and InP substrates can be used to create high-quality single-junction devices with a large variety of band gaps. While growths on GaAs are ideal for the 1.6-1.8 eV bandgap range described above, the 1.42 eV bandgap of GaAs is a lower bound for lattice-matched epitaxial growth; on the other hand, lattice-matched growths on InP, while ideal for a low-bandgap subcell, cannot accomodate the high-bandgap junction to deliver the voltage required to drive water electrolysis in a tandem structure.

Direct wafer bonding of sulfide-passivated p^+-GaAs and n^+-InP layers has been used to make high-quailty tunnel diodes between GaAs and InP substrates at a relatively low temperature of 300 °C [86]. The sulfide-passivated improve

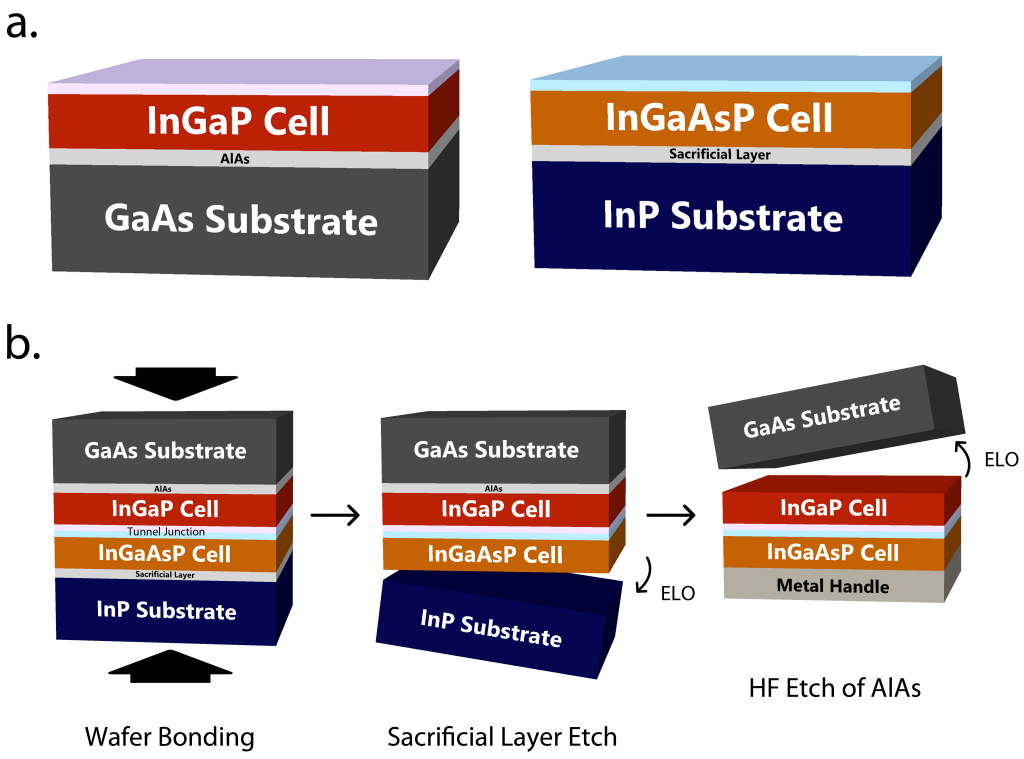

Figure 2.1: Wafer-bonding and epitaxial liftoff process to produce ideal bandgap combinations using single-junction III-V cells grown epitaxially on GaAs and InP. (a) High-quality growth of ternary InGaP (~1.84 eV) on GaAs, and quaternary InGaAsP cell with tunable band gap. (b) Cell processing to create wafer-bonded thin film device.

the interfacial electrical conductivities and direct bonding of the heavily-doped *p*-GaAs/*n*-InP heterojunction. Subcells grown on GaAs and InP can connected in series using a wafer-bonded tunnel diode to create a multijunction device with an ideal bandgap combination.

When coupled with ELO of inverted cells, wafer-bonding technologies allow the combination of high-quality III-V semiconductors grown on substrates with different lattice constants into a single device. This strategy, shown in **Figure 2.1**, would facilitate planar thin-film devices with desired material properties and tunable bandgaps, achieving optimal bandgap combinations for solar fuels. The process in **Figure 2.1b** can be used to create standalone tandem thin-film structures, decreasing cost and providing optical benefs from the metal back reflector; alternatively, on-wafer testing can be performed after ELO of the GaAs substrate following the

wafer-bonding process.

2.2 Device Physics Modeling of III-V Tandem Architectures

The Helmholtz-Zentrum Berlin's AFORS-HET simulation software for 1-D numerical device physics modeling of single-junction semiconductor devices was used to predict cell performance and optimize layer thickness. Material parameters for quaternary and ternary alloys were linearly interpolated from available III-V material properties. A commercial epitaxial manufacturing company Sumika Electronic Materials Inc. was consulted during the design process, and provided feedback on the capabilities of their MOCVD growth process.

No.	Material	Thickness (nm)	Doping	Density (cm^{-3})	Dopant
9	$Al_{0.3}Ga_{0.7}As$	20	p^{++}	$>2 \times 10^{19}$	C
8	$In_{0.48}Al_{0.52}P$	20	p^{+}	2×10^{17}	Zn
7	$In_{0.49}Ga_{0.51}P$	1000	p	1×10^{16}	Zn
6	$In_{0.49}Ga_{0.51}P$	70	n^{+}	1×10^{17}	Si
5	$In_{0.48}Al_{0.52}P$	30	n^{+}	5×10^{17}	Si
4	$In_{0.49}Ga_{0.51}P$	10	n^{+}	3×10^{18}	Si
3	GaAs	7	n^{+}	5×10^{18}	Si
2	AlAs	15	n^{+}	1×10^{18}	Si
1	GaAs	50	n^{+}	5×10^{18}	Si
0	GaAs	Substrate	n^{+}	5×10^{18}	Si

Table 2.1: Epitaxial structure for single-junction reversed n^{+}-p InGaP subcell grown on GaAs.

No.	Material	Thickness (nm)	Doping	Density (cm^{-3})	Dopant
8	InP	30	n^{+}	$>3 \times 10^{19}$	Si
7	$In_{0.52}Al_{0.48}As$	10	n^{+}	5×10^{18}	Si
6	$In_{0.87}Ga_{0.13}As_{0.28}P_{0.72}$	150	n^{+}	1×10^{18}	Si
5	$In_{0.87}Ga_{0.13}As_{0.28}P_{0.72}$	3000	p	5×10^{17}	Zn
4	$In_{0.52}Al_{0.48}As$	10	p^{+}	1×10^{18}	Zn
3	InP	30	p^{+}	1×10^{19}	Zn
2	$In_{0.53}Ga_{0.47}As$	30	p^{+}	1×10^{19}	Zn
1	InP	30	p^{+}	1×10^{19}	Zn
0	InP	Substrate	p^{+}	1×10^{19}	Zn

Table 2.2: Epitaxial structure for single-junction n^{+}-p InGaAsP subcell grown on InP.

The optimized 1.84/1.2 eV dual-junction InGaP/InGaAsP cells were designed

for growth on GaAs and InP substrates, respectively, and are listed in **Table 2.1** and **Table 2.2** . The InGaP cell is grown in inverted order, with removal of the substrate using the 15 nm AlAs thin film (layer 2) as the epitaxial lifoff layer leaving behind the highly-doped 7 nm GaAs layer (layer 3) on the surface of the device. Layers 6 and 7 show the n/p solid-state buried junction. Each growth included a highly-doped thin tunnel junction layer for the wafer-bonding process. In **Table 2.1** an AlGaAs layer was chosen, increasing the bandgap of the tunnel junction layer to prevent shading of the low-bandgap cell. Layer 2 in the growth on the InP substrate in **Table 2.2** is meant as an etch stop layer in order to enable etching of the InP substrate layer. This allows liftoff of the bonded GaAs cell without the complications of a second liftoff step. Initial laboratory-scale demonstrations can be performued using on-wafer testing. Afterwards, with the sidewalls of the wafer-bonded device chemically protected, and the InP substrate can be selectively etched to produce the final thin film device. Future designs could include a sacrificial liftoff layer lattice-matched to InP instead of the etch stop layer.

No.	Material	Thickness (nm)	Doping	Density (cm^{-3})	Dopant
14	GaAs	100	p^{++}	$>1 \times 10^{19}$	Zn
13	$In_{0.48}Al_{0.52}P$	30	p^{+}	3×10^{17}	Zn
12	$In_{0.49}Ga_{0.51}P$	70	p^{+}	1×10^{17}	Zn
11	$In_{0.49}Ga_{0.51}P$	430	n	1×10^{16}	Si
10	$In_{0.48}Al_{0.52}P$	20	n^{+}	1×10^{17}	Si
9	GaAs	20	n^{++}	$>2 \times 10^{19}$	Te
8	$Al_{0.3}Ga_{0.7}As$	20	p^{++}	$>2 \times 10^{19}$	C
7	$In_{0.49}Ga_{0.51}P$	20	p^{+}	5×10^{18}	Zn
6	$Al_{0.2}Ga_{0.8}As$	150	p^{+}	1×10^{18}	Zn
5	GaAs	3000	n	2×10^{17}	Si
4	$In_{0.49}Ga_{0.51}P$	30	n^{+}	3×10^{18}	Si
3	GaAs	300	n^{+}	5×10^{18}	Si
2	AlAs	150	n^{+}	1×10^{18}	Si
1	GaAs	50	n^{+}	5×10^{18}	Si
0	GaAs	Substrate	n^{+}	5×10^{18}	Si

Table 2.3: Epitaxial structure for dual-junction InGaP/GaAs III-V cell.

A second tandem structure was also modeled and optimized using a single epitaxial growth on GaAs. While this design delivers a lower current which would limit efficiency, it can provide an increase of 600 mV compared to the InGaP/InGaAsP cell. This InGaP/GaAs structure had a bandgap combination of 1.84/1.42 eV and was designed for PEC applications that require a larger voltage for operation. For

optimal performance under the AM1.5 spectrum, thinning of the InGaP top cell is required to allow current matching between both junction. The 100 nm surface layer of GaAs was included for solid state testing, meant to be etched away with a selective etch for use in the PEC device. However, this process created many complications in the cell fabrication process, and future iterations of this growth did not include this thick film.

The predicted cell performance and solar-to-hydrogen efficiencies of these two cell architectures are shown in **Table 2.4**. The remaining sections cover the growth and characterization of the higher-voltage InGaP/GaAs design that will lead to the demonstration of a full solar water-splitting device using the ALD-TiO_2 protection scheme.

Subcells	Bandgaps	V_{oc} (V)	J_{sc} (mA cm^{-2})	η_{STH} (%)
InGaP/InGaAsP	1.84/1.20	1.9	16.4	20.2
InGaP/GaAs	1.84/1.42	2.5	13.19	16.2

Table 2.4: Results from AFORS-HET 1D numerical simulation of the multijunction devices under the 1-sun AM1.5 solar spectrum.

2.3 Epitaxial MOCVD Growth and Cell Processing

The initial dual junction device was grown commercially through Sumika Electronic Materials, Inc. according to specifications shown in **Figure reffig:VER1a**. Planar III-V layers were grown epitaxially by metal-organic chemical vapor deposition (MOCVD) on an n^+-GaAs wafer with a (100)-oriented polished surface with 2 deg offcut towards (110) (Si-doped, acceptor concentration of 1×10^{19} cm^{-3}, 6" diameter).

A tandem-junction photoabsorber consisting of an InGaP top cell (E_g = 1.84 eV) and GaAs bottom cell (E_g = 1.42 eV) was designed and modeled using a 1-D numerical simulator for operation under the Air Mass (AM) 1.5 solar spectrum [87]. **Figure 2.2** shows the structure of the InGaP/GaAs tandem cell. The GaAs bottom cell consisted of an n^+-InGaP back surface field (BSF) layer, an n-GaAs base layer, a p^+-AlGaAs emitter, and a p^+-InGaP window layer. The InGaP top cell consisted of an n^+-InAlP BSF layer, an n-InGaP base layer, a p^+-InGaP emitter, an p^+-InAlP window, and a p^+-GaAs contact layer. The InGaP top cell and GaAs bottom cell were connected electrically by an GaAs/AlGaAs tunnel junction.

Ohmic contact to the n^+-GaAs wafer was formed using a Ge-Au eutectic (20 nm

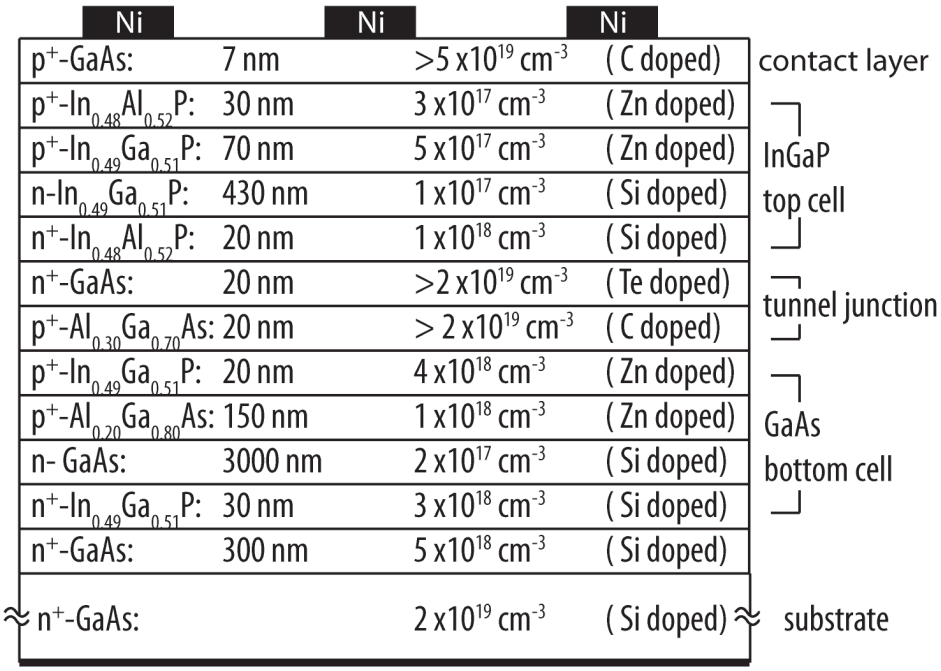

Figure 2.2: Structure of the InGaP/GaAs tandem cell architecture using an AlGaAs/GaAs tunnel junction.

Ge/ 30 nm Au/ 15 nm Ni/ 100 nm Au) deposited by radio-frequency (RF) sputtering and annealed under N_2(g) at 400 °C for 30 s using rapid thermal annealing. Solid-state devices were formed by RF sputtering a metal grid of 100 nm thick Ni onto the p^+-GaAs surface.

2.4 Non-Aqueous PEC Characterization

In order to test the quality of the III-V epilayer growth, especially the performance of the thin and degenerately doped layers of the n^{++}-GaAs / p^{++}-AlGaAs tunnel junction, our first step was to design an experiment to verify the voltage of the device under illumination. In order to avoid any cell processing on the surface of the device, which would complicate this first round of testing, initial characterization of the tandem structure was made using the ferrocene/ferrocenium (Fc/Fc+) redox couple is shown in **Figure 2.3**.

This characterization was performed in the inert atmosphere of a N_2 glovebox. The non-aqueous solution of 50 mM ferrocene (Fc) and 0.5 mM Ferrocenium (Fc+)

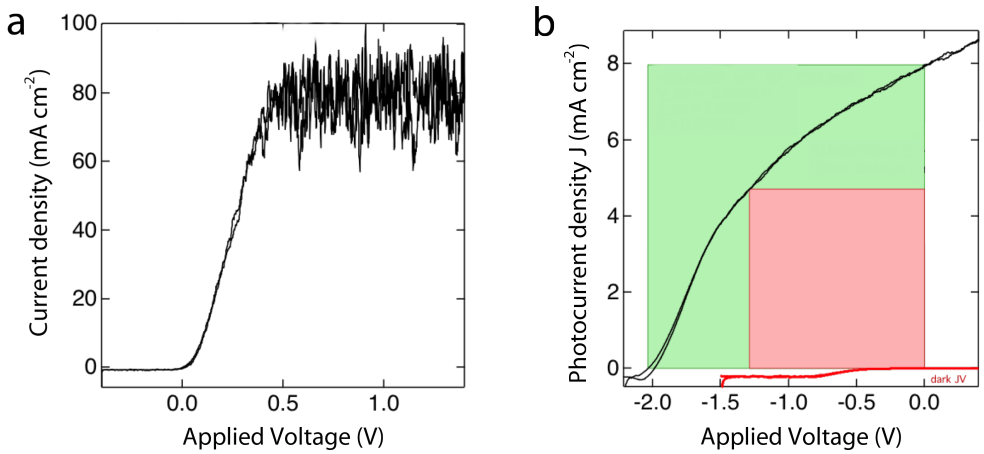

Figure 2.3: Non-aqueous two-electrode cyclic voltammetry using (a) a platinum wire, and (b) the tandem InGaP/GaAs device.

was prepared inside the glovebox, and all glass and electrode surfaces were rinsed in methanol before testing. An ELH-type W-halogen lamp was used to simulate 1-Sun illumination, and was calibrated using a Si photodiode.

Figure2.3a shows the characteristic curve that results from two-electrode cyclic voltammetry using a Pt wire as the counter electrode. In **Figure 2.3b** the Pt wire was used as a reference electrode, and the result is an illuminated cyclic voltammetry (CV) curve of the III-V multijunction stack. Although this curve is not indicative of the fill factor (FF) or current density of the tandem, the open-circuit voltage (V_{oc}) is shown to be greater than 2.0 V, which is indicative of a good quality growth with a high-performing tunnel junction, as neither the InGaP nor the GaAs subcells could individually supply such a large V_{oc}.

2.5 Dual-Junction Solid State Device Performance

A Xe lamp-based solar simulator and probe station was used to measure the solid-state device performance. The light intensity was adjusted based on an NREL-calibrated Si photovoltaic reference cell.

Figure 2.4a shows the solid-state current density vs. voltage (J-V) performance of the tandem cell. Under simulated 1 sun illumination, the short-circuit current density (J_{sc}), the open-circuit voltage (V_{oc}) and the fill factor (FF) were 7.6 mA cm^{-2}, 2.4 V, and 0.76, respectively. **Figure 2.4b** shows the spectral response behavior of the tandem device. The integrated short-circuit current density under AM 1.5 illumination for the top cell and the bottom cell were $J_{top,int}$ = 7.6 mA cm^{-2} and $J_{bot,int}$ = 9.3 mA cm^{-2}, respectively. The large band gap InGaP top cell was

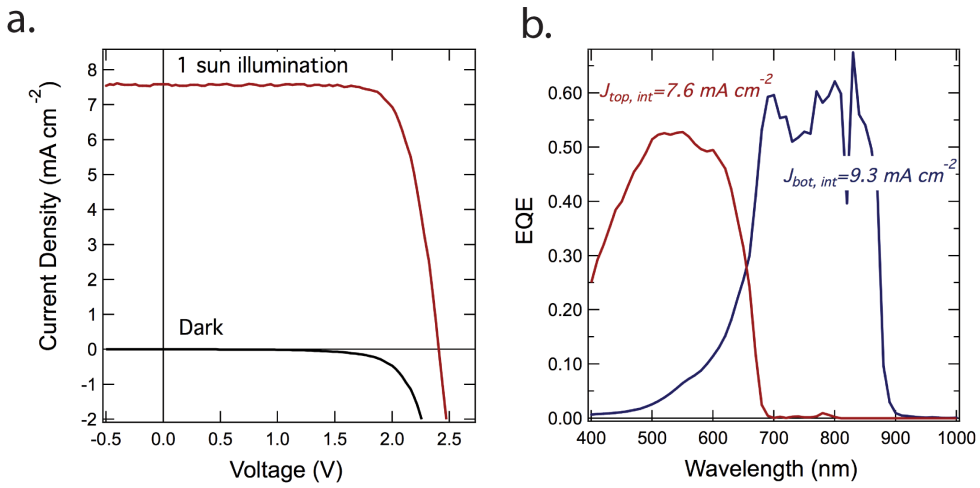

Figure 2.4: Solid state performance of III-V dual junction cell using a Ni metal front contact. (a) J-V performance in the dark (black) and under 1 sun illumination (red). (b) Spectral response behavior of the tandem cell, for which the integrated light-limiting current densities under AM 1.5 illumination were $J_{top,int}$ = 7.6 mA cm^{-2} and $J_{bot,int}$ = 9.3 mA cm^{-2}, respectively.

current limiting, and the calculated $J_{top,int}$ matched the measured J_{sc} in **Figure 2.4a**.

The EQE of the solid state device and the photoelectrochemical electrodes made from this III-V stack explored in **Chapter 3** are not optimal and have room for improvement in future designs. The solid-state measurements were obtained without any surface treatment or anti-reflection coating, which results in reflection losses of ~30% for most wavelengths in the solar spectrum. A second cause of reduced EQE is parasitic absorption by the ~7 nm GaAs contact layer, which absorbs photons that have energies above the band gap of GaAs, 1.42 eV. The presence of this layer was needed to obtain facile for hole conduction through the TiO_2 protection layer, since ALD-TiO_2 grown on window layers that contained exposed aluminum did not exhibit the desired electrical properties. Simulations indicated that parasitic absorption of short wavelength light was especially detrimental to the performance of the high bandgap InGaP cell.

2.6 TiO_2 as an Antireflective Coating for Photoelectrochemical Devices

Given a a surface with a single antireflective coating of thickness d and index n_1, the expression for the fraction of energy reflected off of the surface from a

monochromatic beam with normal incidence is

$$R = \frac{r_1^2 + r_2^2 + 2r_1 r_2 \cos 2\theta}{1 + r_1^2 r_2^2 + 2r_1 r_2 \cos 2\theta} \tag{2.1}$$

with

$$\theta = \frac{2\pi n_1 d}{\lambda} \tag{2.2}$$

and where r_1 and r_2 are

$$r_1 = \frac{n_0 - n_1}{n_0 + n_1} \quad , \quad r_2 = \frac{n_1 - n_2}{n_1 + n_2} \tag{2.3}$$

with n_0, n_1, and n_2 being the indices of refraction for the solution, antireflective layer, and substrate, respectively. The reflection is minimized when $n_1 d_1 = \lambda_0/4$, which gives:

$$R_{min} = \left(\frac{n_1^2 - n_0 n_2}{n_1^2 + n_0 n_2} \right)^2 \tag{2.4}$$

and is zero when $n_1 = \sqrt{n_0\, n_2}$.

For a Si ($n \approx 3.9$) or InGaP ($n \approx 3.5$) device in solution ($n_{sol} \approx 1.3$), the optimum refractive index for the ARC is $n_1 = \sqrt{n_{sol}\, n_{cell}}$ which gives an optimal index range of $n_1 \approx 2.0$–2.2. The index of ALD-TiO_2 at around 600 nm is 1.9, close to ideal for a single-layer ARC.

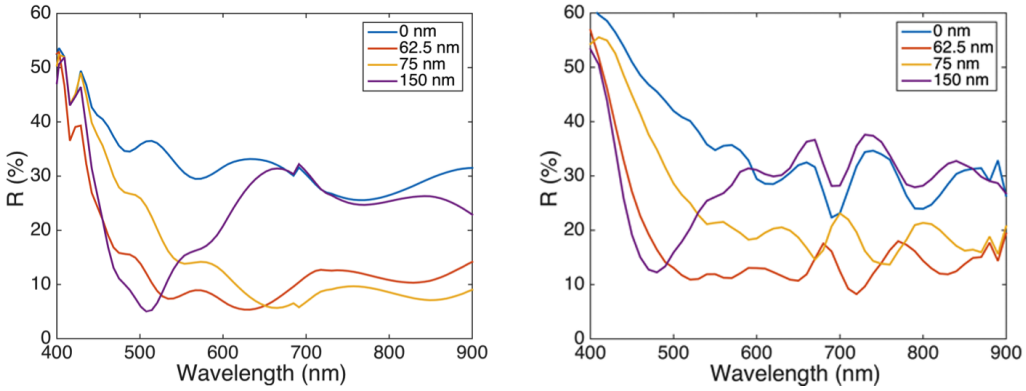

Figure 2.5: Reflectance of InGaP/GaAs structure with varying thicknesses of TiO_2 that serves as a single-layer anti-reflection coating. Left: Optical model. Right: Integrating sphere.

In order to design the optimal thickness of TiO_2, simulations were performed and compared to experiment. Reflectance spectra of the tandem III-V substrate with TiO_2 coatings of different thicknesses were calculated by solving the transfer matrix (**Figure 2.5**). Refractive indices of all the layers were obtained or interpolated

from experimental data at http://www.ioffe.ru/SVA/NSM/nk/. The refractive index of protective TiO_2 from atomic layer deposition was obtained from spectroscopic ellipsometry. The Matlab function (multidiel), developed by Sophocles J. Orfanidis from Rutgers University, was used to calculate the reflection responses of the isotropic lossy multilayer dielectric structures [88]. The structural information used in the calculation is shown in **Figure 2.2**.

The optical reflectance of the III-V tandem substrates as a function of TiO_2 thickness (**Figure 2.5**) was determined by using an integrating sphere at normal incidence (Agilent Cary 5000 UV-Vis spectrometer). The absorptance (A) of TiO_2-coated substrates was calculated from the measured total reflectance (R) and transmittance (T) of the electrode as $A = 1-R-T$. All optical measurements were performed in air on fresh samples without chemical/electrochemical treatment. These results motivated the design of a TiO_2 anti-reflection coating, explored in **Chapter 3** .

2.7 Summary

Following the design of two III-V multijunction stacks optimized for use in PEC devices, an InGaP/GaAs tandem cell was grown via MOCVD. It was characterized using non-aqueous electrochemistry and also found to have good solid-state J-V performance with a large V_oc and relatively high current densities, with room for improvement. In the following chapters, removal of the surface GaAs cap layer and improved current matching between the two junctions will be used to increase performance.

Chapter 3

FULLY-INTEGRATED, HIGH-EFFICIENCY III-V DEVICE FOR SOLAR WATER SPLITTING

The following chapter discusses the assembly of a fully integrated, unassisted water-splitting solar fuels prototype with solar-to-hydrogen efficiency $\eta_{STH} > 10\%$, culminating in the final design shown in **Figure 3.1**.

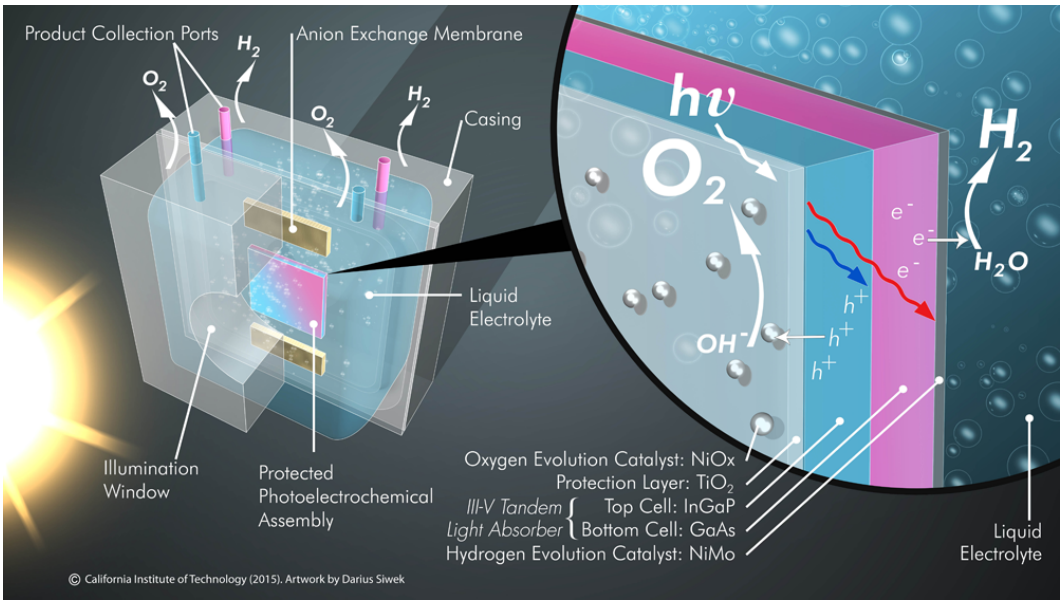

Figure 3.1: Fully integrated III-V unassisted water-splitting prototype.

Content in this chapter is drawn from the following publication:

- Verlage, E., Hu, S., Liu, R., Jones, R. J. R., Sun, K., Xiang, C., Lewis, N. S. & Atwater, H. A. A monolithically integrated, intrinsically safe, 10% efficient, solar-driven water-splitting system based on active, stable earth-abundant electrocatalysts in conjunction with tandem III-V light absorbers protected by amorphous TiO_2 films. *Energy & Environmental Science* **8,** 3166–3172 (2015).

3.1 Hole Conduction Through Amorphous TiO_2

It has recently been shown that thick films of amorphous TiO_2 deposited using atomic-layer deposition (ALD) capped with a Ni electrocatalyst can be used to pro-

tect a variety of photoanode materials under OER conditions in alkaline electrolytes [78–80].

The sputtered Ni electrocatalyst is essential for conduction through thick layers of TiO_2. While high work function metal contacts such as Ir produce lower conductivity through the TiO_2 film [78, 89], the deposition of low work function metals like Ni removes the rectifying barrier of the TiO_2/solution interface that blocks charge conduction to the surface [78]. Cyclic voltammetry can be performed to age the Ni film, transforming it into $NiFeO_x$, which is a highly-active and earth-abundant electrocatalyst.

This phenomena of hole conduction in TiO_2 has previously been ascribed to many different processes, from intrinsic conductivity through the conduction band [90], to mid-gap energy levels due to carbon and nitrogen impurities and/or Ti^{3+} electronic defect states [89]. This conductivity is not dependent on deposition method or the amorphous structure, as sputtered and crystalline TiO_2 have been shown to conduct charge on n-Si/TiO_2/Ni photoanodes[89]. Operando X-ray phtoelectron spectroscopy performed on the Si/TiO_2 interface has elucidated the junction characteristics that lead to TiO_2 conduction under operating conditions [91].

Current work indicates Ti^{3+}, from oxygen vacancies or disordered structure, is responsible for creating the energetic defect states within the band gap of amorphous TiO_2 [92]. Changing the TiO_2 deposition processes and temperatures produces a variety of different concentrations of Ti^{3+}, which affects the hole conduction through these films. If the metallic top contact has a work function below ~5.2 eV, the Ti^{3+} states remain on the surface; however, higher work functions cause local states to be converted into Ti^{4+}, which leads to a decrease in conductivity [92].

3.2 Design of the ALD-TiO_2 Protection Layer for III-V PECs

The protective films were deposited on the exposed p^+-GaAs epilayer at 150 °C using an Ultratech Fiji 200 plasma atomic-layer deposition (ALD) system (**Figure 3.2**). In order to prevent corrosion of the III-V epilayers, care was taken to clean surfaces prior to deposition of ALD-TiO_2 in order to prevent pinhole formation. Prior to ALD, the epitaxial surface was immersed for 30 s in 1.0 M KOH (aqueous solution of potassium hydroxide pellets, semiconductor grade, 99.99% trace metals basis, Sigma-Aldrich), rinsed with copious amounts of deionized water, dried using a stream of N_2(g), and loaded immediately into the ALD chamber. Each ALD cycle consisted of a 0.06 s pulse of H_2O (18 MΩ·cm resistivity, Millipore), followed by a

0.25 s pulse of tetrakis(dimethylamido)titanium (TDMAT, Sigma-Aldrich, 99.999%, used as received). A 15 s purge under a constant 0.13 L min^{-1} flow of research-grade Ar (g) was performed between each precursor pulse. The base pressure during the TiO_2 growth was maintained at ~0.1 Torr. Though care was taken to clean surfaces to prevent defect formation in the TiO_2 film, and small area samples were routinely found to be chemically passivated under operation, large area samples on the order of 1 cm^2 were likely to develop at least one pinhole. The yield of stable > 1 cm^2 devices was low, most likely due to particulates in the environment. Access to an ALD system in a class 100 cleanroom would likely reduce this issue, increasing yields of pinhole-free films.

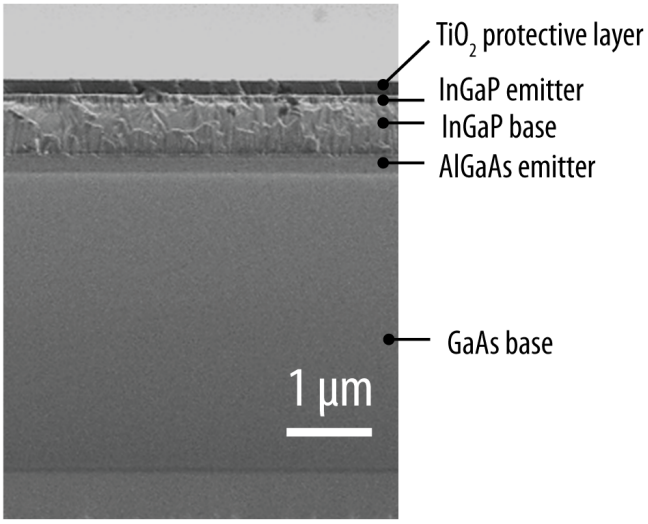

Figure 3.2: Cross-sectional SEM image of a GaAs/InGaP/TiO_2/Ni photoelectrode.

The results from **Section 2.6** were used to select a TiO_2 anti-reflection coating thickness that increased current density in the current-limiting InGaP cell. While ALD-TiO_2 thicknesses around 62.5 nm were ideal for light absorption in the device, thicker films were found to provide more conformal coverage to serve as a protection layer. For large-area devices, thicker protection layers were grown to provide improved longevity during stability tests. ALD-TiO_2 films with thicknesses of 62.5 nm and 150 nm were used to protect III-V surfaces.

3.3 Catalyst and Ion-Exchange Membrane Incorporation

The scalability of III-V devices for use in solar water-splitting depends upon the exclusion of noble metal catalysts in favor of earth-abundant components, and the creation of intrinsically-safe architectures that use anion and/or cation exchange membranes avoid explosive mixtures of hydrogen and oxygen.

Electrocatalyst selection and preparation

The chemical stability and catalytic overpotential of electrocatalysts in acidic or alkaline environments are important considerations for the design of a fully-integrated water-splitting device, and determine the electrolyte used in the final design.

Molecular electrocatalysts, both soluble and attached to an electrode, have created many systems that exhibit high turnover frequencies; however, this metric is often at the expense of catalytic overpotential [1]. On top of this, many molecular catalysts are active in nonaqueous electrocatalytic conditions and not stable in aqueous solutions. In the design process, we chose to focus on metal-oxide heterogeneous catalysis.

From literature, and from a comprehensive benchmarking studies by the Joint Center for Artificial Photosynthesis (JCAP) that looked at OER electrocatalysts for use in acidic and alkaline environments [51, 68], it is clear there are many earth-abundant OER electrocatalysts for use in strong base, and currently no viable options in acidic environments. The only highly active catalysts suitable for operation in acidic environments are expensive IrO_x and RuO_x. Until earth-abundant alternatives to Ir and Ru-based electrocatalysts are available, a photoanode that utilizes earth-abundant materials must operate in alkaline conditions.

Available active and earth-abundant OER electocatalysts that show stability in strong base include $NiFeO_x$, $CoFeO_x$, $NiCoO_x$, and NiO_x [51], all of which show catalytic activity that rivals that of IrO_x in 1.0 M NaOH at 10 mA cm^{-2}. Of these options, $NiFeO_x$ has the lowest overpotential. Oxidation/aging of Ni films in aqueous solutions (1.0 M KOH solution) by cyclic voltammetry, initially thought to form $Ni(OH)_2$/NiOOH surfaces, leads to the absorption of Fe impurities in the film, causing a large increase in OER activity for these electrocatalysts [93]. In fact when the aging process is performed under inert conditions to produce $Ni(OH)_2$/NiOOH, the activity of the film is drastically reduced [93]. In the aged $Ni_{1-x}Fe_x(OH)_2$/$Ni_{1-x}Fe_xOOH$, Fe-induced partial-charge-transfer mechanisms activate Ni centers throughout the film. Long-range order is unimportant for the

catalytic activity of $Ni_{1-x}Fe_xOOH$ systems [93], and no annealing is required for activation. $Ni_{1-x}Fe_xO_x$ electrocatalytic films can easily be formed on electrode surfaces by physical vapor deposition of Ni films (through sputtering or e-beam evaporation techniques) followed by the aging process in the aqueous alkaline electrolyte of the cell.

The design of these films for use on III-V photoanode surfaces must also take into account optical transparency of the electrocatalyst, as well as interfacial properties when combined with the protective oxide. In thick metal films patterned onto the surface of tandem light-absorber structures, there is a trade-off between optical obscuration and concentrated operational current densities at the catalyst surface. Low filling fractions, which decrease parasitic absorption in the films, force operation at high current densities, resulting in an increase in the kinetic overpotentials of the electrocatalytic films [94]. In the case of $NiFeO_x$, patterning was not required as the oxidation process applied to very thin Ni films decreases obscuration significantly.

For all photoanode surfaces in this chapter, an optically transparent nominally 2 nm thick Ni film was deposited on TiO_2 surfaces using RF sputtering. Before all electrochemical measurements, Ni aging was performed in 1.0 M KOH(aq) to activate the $NiFeO_x$ and decrease obscuration of the device.

Looking at compatible electrocatalysts for the HER in alkaline solutions, NiMo was a very attractive option. In a benchmarking study, it was shown to outperform Pt at 10 mA cm^{-2} per geometric area in 1.0 M NaOH [68]. Previous work has used NiMo nanoparticles [95, 96], and this method was used to create large area cathodic counter electrodes for 3-electrode testing of the photoanode surface.

Counter electrodes were formed by drop casting NiMo nanoparticles on Ni foil and annealing under forming gas (5% H_2, 95% N_2, 500 sccm, Airliquide) at 450 °C for 30 min, then cooling the electrodes to room temperature under forming gas [95]. For the fully integrated prototype, a Ti/NiMo electrocatalyst was deposited using RF sputtering onto the Au-Ge back contact of the III-V device.

Anion exchange membrane (AEM) selection and incorporation

Following the discussion in **Section 1.5** about intrinsically safe operation, it is clear that a water-splitting cell must consist of two electrolyte-containing compartments: a cathode compartment in which protons and/or water molecules are reduced to H_2(g), and an anode compartment in which hydroxide ions and/or water molecules

are oxidized to O_2(g). The compartments are bridged by a membrane that provides the ionic transport necessary to complete the oxidation-reduction circuit while maintaining separation of the products.

The incorporation of planar III-V cells into a photoelectrochemical cell requires a module design that allows transport through ion exchange membranes without significant reduction in the illuminated active area. For a planar device, the oxygen and hydrogen evolution reactions occur on opposite sides of the semiconductor stack. The louvered cell geometry shown in **Figure 3.3** [97] allows incorporation of a vertically-mounted membranes that separate the anode and cathode of angled planar light-absorbing structures, while minimizing ionic pathway between the oxygen and hydrogen evolution reaction surfaces [97, 98].

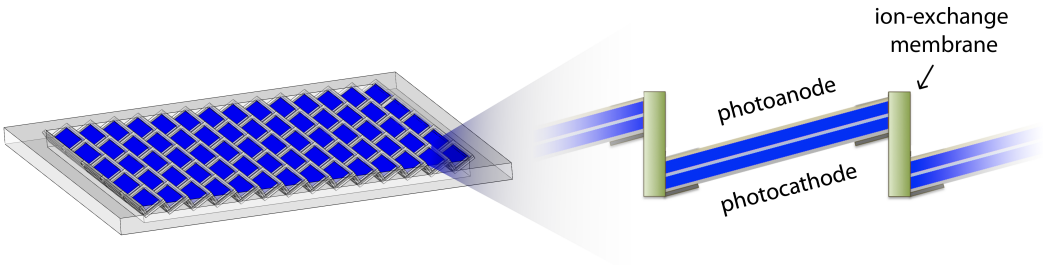

Figure 3.3: Module design for a planar PEC device. Photoelectrodes and the membrane separators are interconnected in a louvered system configuration, with optimized light absorption and solution-transport pathways.

For our device, a commercial AHA-type NEOSEPTA anion exchange membrane was selected for use in 1.0 M KOH. Simulations were performed using the membrane resistance of this AEM to optimize cell architecture dimensions for both a small prototype with a single planar light absorber, and for the more advanced louvered design that incorporated multiple tilted light absorbing slats separated by a vertical membrane. The dimensions of the final prototype design shown in **Figure 3.1** were established using these calculations.

3.4 Cell Processing and Compression Cell Assembly

To measure the current density during photoelectrochemical operation, wafers were cleaved into samples 0.5~1 cm^2 in area, and samples were mounted onto a Cu film using a Ag-based conductive epoxy. Samples were then assembled into custom-made compression cells (**Figure 3.4** and **Figure 3.6a**) that were equipped with

fluorosilicone O-rings (0.0314 cm^2 Teflon, 0.34 cm^2 polymethyl methacrylate).

The fully-integrated prototype chassis (**Figure 3.6a**) consisted of 1x PEC assemblies (10.0 mm x 10.0 mm), 2 x AHA-type NEOSEPTA anion exchange membrane (2 x 10 mm), 2 x acrylic chassis that were 3-D printed, 1 x quartz window (15 mm in diameter), 8 x inlet and outlet ports (PEEK, ID 0.75 mm, OD 1.5875 mm), and 16 x bolts (2-56" x 1") and/or epoxy (Loctite 9460, Hysol).

All transparent sections of the compression cells were covered using high-performance black masking tape purchased from Thorlabs to prevent illumination of electrochemically inactive surfaces.

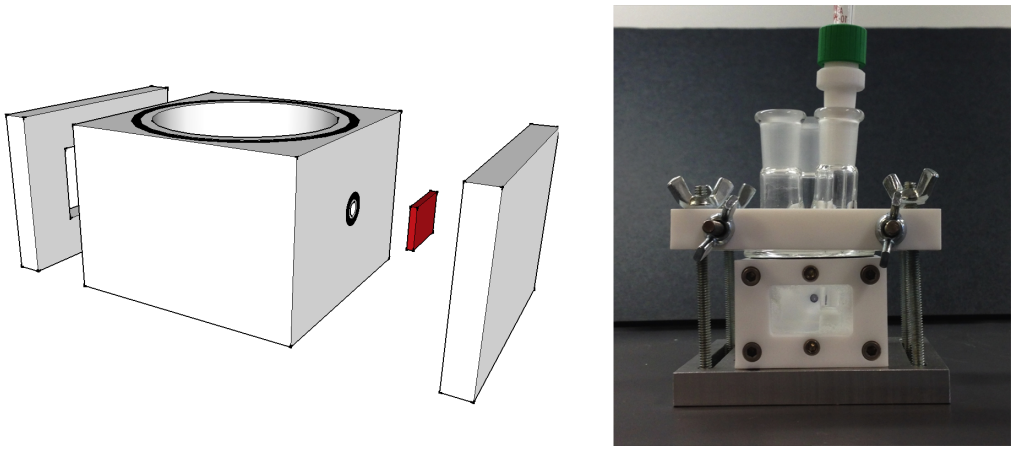

Figure 3.4: Teflon O-Ring compression cell for aqueous photoelectrochemical testing.

3.5 PEC Characterization

For photoelectrochemical experiments, illumination intensity from a Xe arc lamp with an AM 1.5 filter was calibrated by placing a Si photodiode (Thor Labs) in the Teflon compression cell, in the same location occupied by the exposed area of the photoelectrode. The Si photodiode was previously calibrated by measurement of the short-circuit current-density value under AM 1.5 simulated sunlight at 100 mW cm-2 (1- Sun) of irradiance from a Xe arc lamp with an AM 1.5 filter.

To obtain spectral response data, monochromatic light was chopped at 17 Hz and was focused onto the sample surface. An unchopped light-emitting diode (LED) was used to saturate the AlGaAs/GaAs heterojunction (850 nm) or the InGaP homojunction (405 nm), to measure the external quantum yield of the unsaturated subcell. Photoelectrochemical spectral response data were obtained at the formal potential for water oxidation using a side- facing chassis with a 0.34 cm^2 O-ring.

A saturated calomel electrode (SCE, CH Instruments) was used as a reference electrode for all three-electrode photoelectrochemical measurements, including spectral response data. The pH of the 1.0 M KOH(aq) solution was 13.7, as measured using a VWR SympHony SB70P Digital, Bench-model pH Meter. The equilibrium potential for water oxidation in 1.0 M KOH(aq) was calculated to be 0.18 V vs. SCE. The active cell area was determined by the size of the O-ring. For stability tests the custom-built Teflon compression cell (**Figure 3.4**) O-ring size was 0.031 cm^2, and a liquid pumping system was used to facilitate removal of bubbles from the sample surface and to decrease mass transfer effects. All data for three-electrode electrochemical measurements in aqueous solutions included compensation for solution series resistance as obtained from high-frequency electrical-impedance measurements.

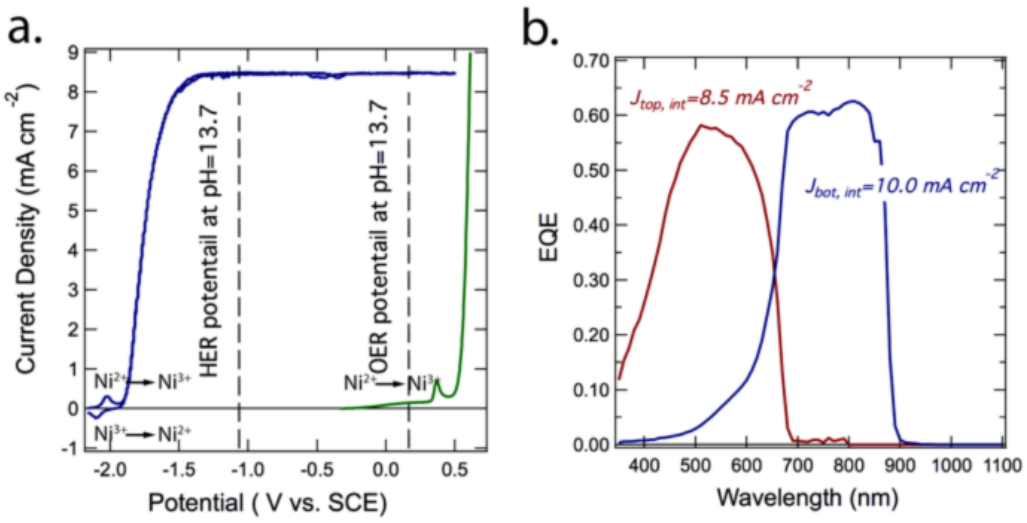

Figure 3.5: Photoelectrochemical performance of III-V water-splitting device. (a) Cyclic voltammetry of the photoanode in 1.0 M KOH(aq) under 1 sun illumination, and dark electrolysis of the TiO_2/Ni protection layer on p^+-GaAs. The formal potential for the oxygen evolution reaction (OER) and the hydrogen evolution reaction (HER) are indicated by dotted lines at 0.18 V and 1.05 V versus SCE. (b) Spectral response of the tandem photoelectrode, for which the integrated light limiting current densities under AM 1.5 illumination were $J_{top,int}$ = 8.5 mA cm^{-2} and $J_{bot,int}$ = mA cm^{-2}, respectively.

For water oxidation, the photoanode surface was protected from corrosion by a 62.5 nm layer of amorphous, hole-conducting TiO_2 that was grown by atomic-layer deposition (ALD). **Figure 3.2** shows a cross-sectional scanning-electron microscopy (SEM) image of the cell structure. The thickness of the TiO_2 layer was chosen to

minimize reflection as a single-layer anti-reflection coating. A 2 nm layer of Ni metal provided an ohmic contact to the TiO_2 surface and, upon activation, formed a highly active, stable, OER catalyst. **Figure 3.5a** shows the cyclic voltammetry of the photoelectrode at 1 sun illumination in 1.0 M KOH(aq). The cyclic voltammetric behavior closely matched the solid-state J-V performance of the device structure, with a light-limited photocurrent density of 8.5 mA cm^{-2}. **Figure 3.5a** also shows the dark electrochemical behavior of the TiO_2/Ni protection layer on highly-doped p^+-GaAs anodes. A load-line analysis using an equivalent-circuit model that consisted of a photodiode connected in series with the dark electrolysis cell indicated that a photodiode with a V_{oc} = 2.25 V, FF = 0.82 and J_{sc} = 8.5 mA cm^{-2} (i.e. η = 15.7%) would be required to produce the same shift in current density vs. potential, J-E, properties as was produced by use of the TiO_2-coated InGaP/GaAs photoelectrode. **Figure 3.5b** shows the spectral response of the photoanode. The integrated light-limiting current densities under AM 1.5 illumination were calculated to be $J_{top,int}$ = 8.5 mA cm^{-2} and $J_{bot,int}$ = 10.0 mA cm^{-2}, respectively. The slightly larger light-limited photocurrent density for the photoelectrode relative to the solid-state device is ascribable to decreased reflection losses in the PEC cell configuration with a TiO_2 protection/anti-reflective coating.

3.6 PEC Stability Under Operating Conditions

Unassisted solar-driven water-splitting was performed in 1.0 M KOH(aq) by wiring the 0.031 cm^2 photoanode to a ~1 cm^2 Ni-Mo cathode, to form a full photoelectrosynthetic cell (**Figure 3.6a**). The photoanode and the cathode were separated by an anion- exchange membrane (AHA-type, NEOSEPTA membrane). The compression cells were covered using high-performance black masking tape to prevent illumination of electrochemically inactive surfaces outside of the O-ring area. Two-electrode chronoamperometry of the device (**Figure 3.6b**) was measured under simulated 1 sun illumination in 1.0 M KOH(aq) through two quartz windows and without an external voltage bias. Initially, a short-circuit photocurrent density, $J_{photo,short}$ = 8.5 mA cm^{-2}, which corresponds to η_{STH} = 10.5%, was observed. $J_{photo,short}$ decreased to 7.3 mA cm^{-2} after 80 hours of operation, maintaining η_{STH} > 10% for 40 h of continuous operation. At these current densities, dissolution of the entire epilayer at 100% Faradaic efficiency would require only 3% of the total charge passed. The use of a round and thick fluorosilicone O-ring caused occasional bubble accumulation inside the O-ring compartment. The transient blocking of the photoelectrodes from the electrolyte due to bubble accumulation caused a sudden

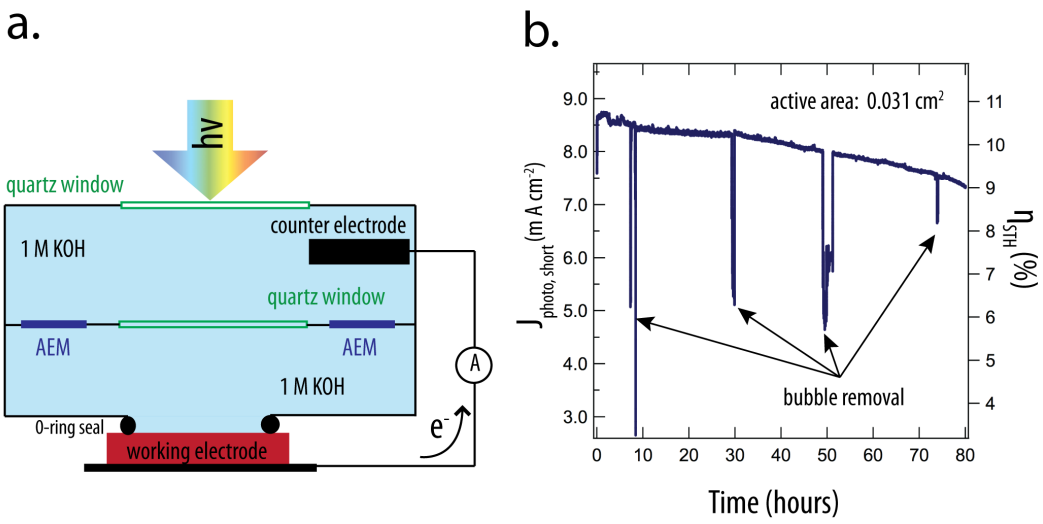

Figure 3.6: Long-term stability test of III-V water-splitting device with TiO_2 protection layer. (a) A schematic illustration of the two-electrode cell configuration, in which the photoanode and the cathode were separated by an anion-exchange membrane. (b) The short-circuit photocurrent density, $J_{photo,short}$, and the corresponding solar-to-hydrogen conversion efficiency, η_{STH}, as a function of time in a two-electrode configuration under 1 sun illumination in 1.0 M KOH(aq).

decrease in $J_{photo,short}$ during the chronoamperometric measurements. However, the dislodging of bubbles did not noticeably affect device performance.

The gradual decrease in current density could be attributed to multiple causes. One potential cause is the evolution of pathways in the TiO_2 film, possibly due to cell processing in a non-cleanroom environment, leading to minimal corrosion on the III-V surface. Over time, more and more of the underlying film is etched away slowly, resulting in a breaking point when the TiO_2 film is compromised. Another explanation for the diminishing current is due to issues with the NiO_x catalyst. While it is possible that the catalyst is delaminating from the surface, over tens of hours of operation, Ni-based oxygen evolution reaction electrocatalysts [93] undergo complex transformations that can cause electrochromism [99, 100] and lead to a gradual change in transmittance.

3.7 Fully-Integrated Water-Splitting Prototype

Following the characterization of a small-scale 3-electrode device, and after verifying the potential for long-term stability of planar structures using amorphous

ALD-TiO_2, the next step was to design a stand-alone device for solar H_2(g) fuel production.

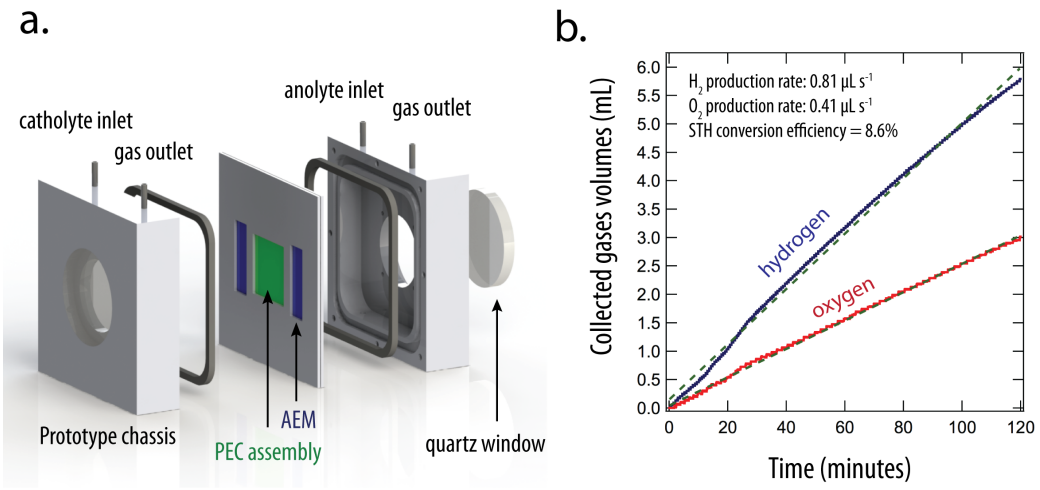

Figure 3.7: Hydrogen fuel collection in unassisted water-splitting prototype. (a) Schematic illustration of a fully monolithically integrated intrinsically safe, solar-hydrogen system prototype. (b) Collected hydrogen and oxygen as a function of time for the integrated prototype (active area = 1.0 cm^2 for both the photoanode and cathode, ALD-TiO_2 thickness of 150 nm) under 1 sun illumination in 1.0 M KOH(aq). Linear fits (dashed lines) during the first two hours of operation were employed to estimate the production rate for H_2(g) (0.81 mL s^{-1}) and O_2(g) (0.41 mL s^{-1}).

A membrane-based, wireless prototype was constructed to demonstrate operation of a full, intrinsically safe, solar-driven water-splitting system. The system was based on a monolithically integrated device that included tandem light absorbers with two sets of protection layers, as well as the HER and OER electrocatalysts. The dimensions of the chassis were designed using a multi-physics model to minimize the transport losses in the electrolyte and in the membrane [23], and a thicker 150 nm layer of ALD-TiO_2 served as a protection layer. The thicker TiO_2 film did not function optimally as an anti-reflection coating, but was required to ensure complete coverage of the anodic surface of the device and long-term stability.

A custom-built polymethyl methacrylate (PMMA) chassis with anion exchange membrane partitions shown in **Figure 3.7a** was used to separate the gas products. A system of Teflon tubing at the top of each chamber allowed H_2(g) and O_2(g) to flow into two eudiometers (0.05 mL precision) that were filled with deionized water and suspended over large water reservoirs. To prevent escape of hydrogen gas through

the solution, the reservoir for H_2(g) collection was saturated with pure H_2(g) for 30 min before operation.

The respective conduits transported gas products from the chassis chambers to the eudiometers (inverted burette geometry), terminating at the water reservoir level to insure that the chassis continuously operated at STP without any buildup of backpressure. High precision manometers (Extech HD755) were used to sample the pressure variation inside the eudiometers due to increasing gas volume every second. The pressure was measured in inches water column, resulting in a well-defined meniscus velocity during the experiment. A simple conversion factor between the eudiometer length and the eudiometer volume allowed determination of the gas production rate (ml/s) from measurement of the meniscus velocity (in/s). As produced gases were introduced to the inverted burette and the water level decreased, the pressure of the gases inside the burette increased. An additional conversion factor was applied to obtain the volume of produced gas at STP, which was used to obtain the solar-to-hydrogen conversion efficiency.

The prototype exhibited an average hydrogen and oxygen production rate of 0.81 mL s^{-1} and 0.41 mL s^{-1} as measured by the two eudiometers (**Figure 3.7b**). The gas evolved from the cathode chamber and from the anode chamber showed minimal (<0.5%) product gas crossover. The near 2:1 ratio of the product gas and the minimal product crossover also indicated that minimal photocorrosion of the III-V materials occurred during the testing period. The gas production rate decreased around 10% after 4 h of operation of the monolithically integrated device, likely due to pinhole formation around dust particles that were present on the photoanode surface before the protection coating process.

The performance attributes exhibited by the fully operational system resulted from adherence to the optoelectronic and electrochemical engineering design principles that have been developed to guide the fabrication of efficient, intrinsically safe, solar-fuels generators [22, 23, 39, 81, 101, 102]. The system geometry and sample dimensions produced maximal light absorption while minimizing the ohmic losses in the electrolyte [23, 39]. In the absence of product separation, co-evolved, stoichiometric mixtures of H_2(g) and O_2(g) would be produced, and this explosive mixture would prevent safe operation of the device. The membrane allowed for robust product separation [23, 39], and low gas crossover rates through the membrane ensured intrinsically safe operation of the system. The pressure differential between the anolyte and catholyte allowed for beneficial collection of the H_2(g) into a pipeline

without fluid flow across the membrane, resulting from Darcy's law, which would produce catastrophic failure of the system [23]. The alkaline electrolyte insured a transference number of essentially unity for flow of hydroxide ions across the anion exchange membrane, to allow for neutralization of the pH gradient that would otherwise occur between the surface of the anode and cathode in the system [23, 39]. The band gaps and photovoltages of the light absorbers were optimized to produce a photovoltage at the maximum power point of the system that would be sufficient to drive the electrolysis reactions as facilitated by earth-abundant, active, stable, HER and OER electrocatalysts in conjunction with the residual ohmic losses in the device.48 Further improvements in efficiency are possible by minimizing reflection losses and by optimization of the subcell current densities for current matching. Note that the electrolyte need not be a liquid, and polymeric electrolytes in conjunction with a pure water feed are generally used in analogous systems such as PEM-based electrolyzers [103].

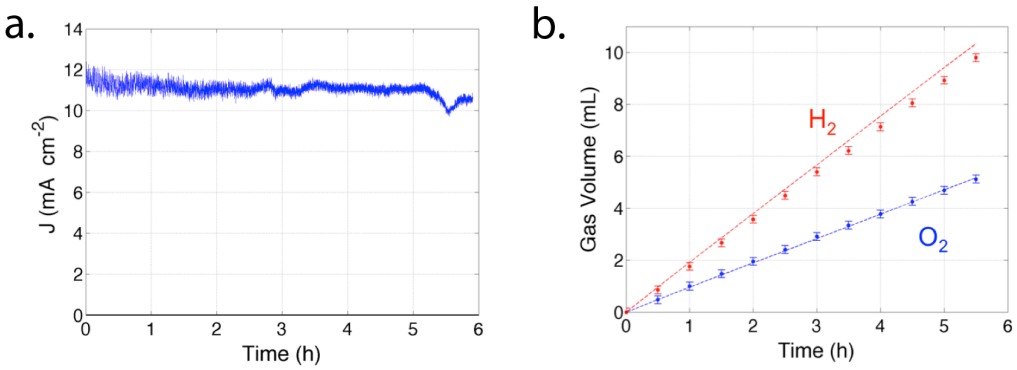

Figure 3.8: Faradaic efficiency of water-splitting prototype. (a) Short-circuit photocurrent density J_{photo}, short under 1.5 Suns using AM 1.5 illumination. (b) Gas volume was measured at regular intervals, and is compared to expected gas production (dotted lines) based on total charge passed.

Faradaic Efficiency

Additional gas collection measurements were made using the chassis from **Figure 2.5a** to determine the faradaic efficiency of the system, as shown in **Figure 3.8**. The current density from spontaneous water splitting was measured at zero external bias under 1.5 Sun illumination from a Xe arc lamp with an AM 1.5 filter. This system was used to calculate the expected gas production. Measurements were made at regular intervals over a 5 h period. The Faradaic efficiency was 100% for O_2(g), and was 90% for H_2(g) collection, probably due to hydrogen leaks in the chassis

and tubing. The final products were analyzed using gas chromatography (GC) by thermal conductivity detectors (TCD), and the composition of the products was confirmed as well with a ~2% gas crossover rate.

3.8 Device Failure Mechanisms

For all samples, device failure was followed by a large increase in current density (as shown in **Figure 3.9**) caused by a breach in the TiO_2 protective film that led to photocorrosion of the III-V layers. Lateral corrosion of the III-V device caused cracks in the TiO_2 that would eventually lead to liftoff of the protection layer, as can be seen in **Figure 3.10**. The large increase in current density is due to corrosion of the underlying III-V epilayers. Cyclic voltammetry of the device during the corrosion process (**Figure 3.9**) reveal a decay in voltage over time and a corrosion onset around the OER redox potential. When the protection layer is breached, shunting occurs for the current-limiting top junction as the InGaP cell as it is corroded away, leaving exposed the GaAs subcell leading to a drop in voltage and larger J_{sc}. This increase in current density contributes further to lateral etching of the pretection layer.

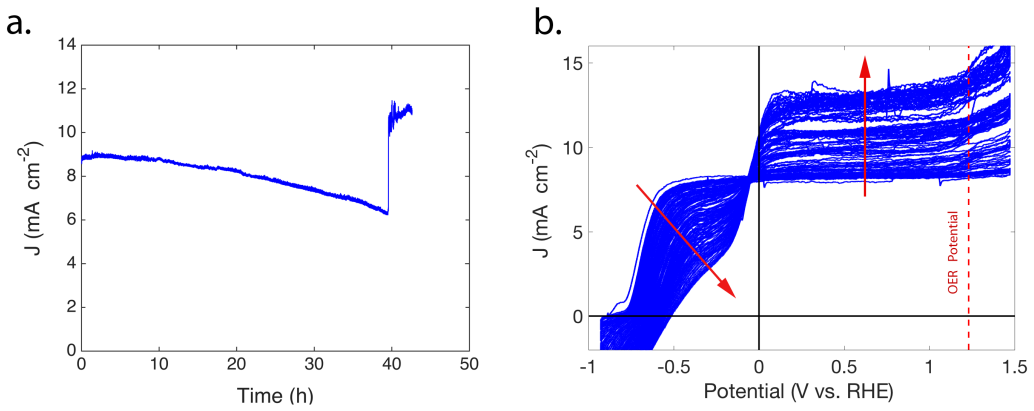

Figure 3.9: Example of III-V device corrosion due to pinhole formation during long-term stability test (representative sample). (a) Chronoamperometry (CA) of device. (b) Cyclic voltammetry (CV) during corrosion process.

This behavior is expected because GaAs and the underlying III-V layers undergo active corrosion by dissolution under anodic conditions in alkaline electrolytes [30, 57, 58]. Therefore, for such materials, the presence of macroscale defects or pinholes in the protective film, due to the presence of dust particles on the semiconductor surface prior to and during film deposition, can lead to etching and undercutting of the TiO_2 that eventually results in catastrophic failure of the device.

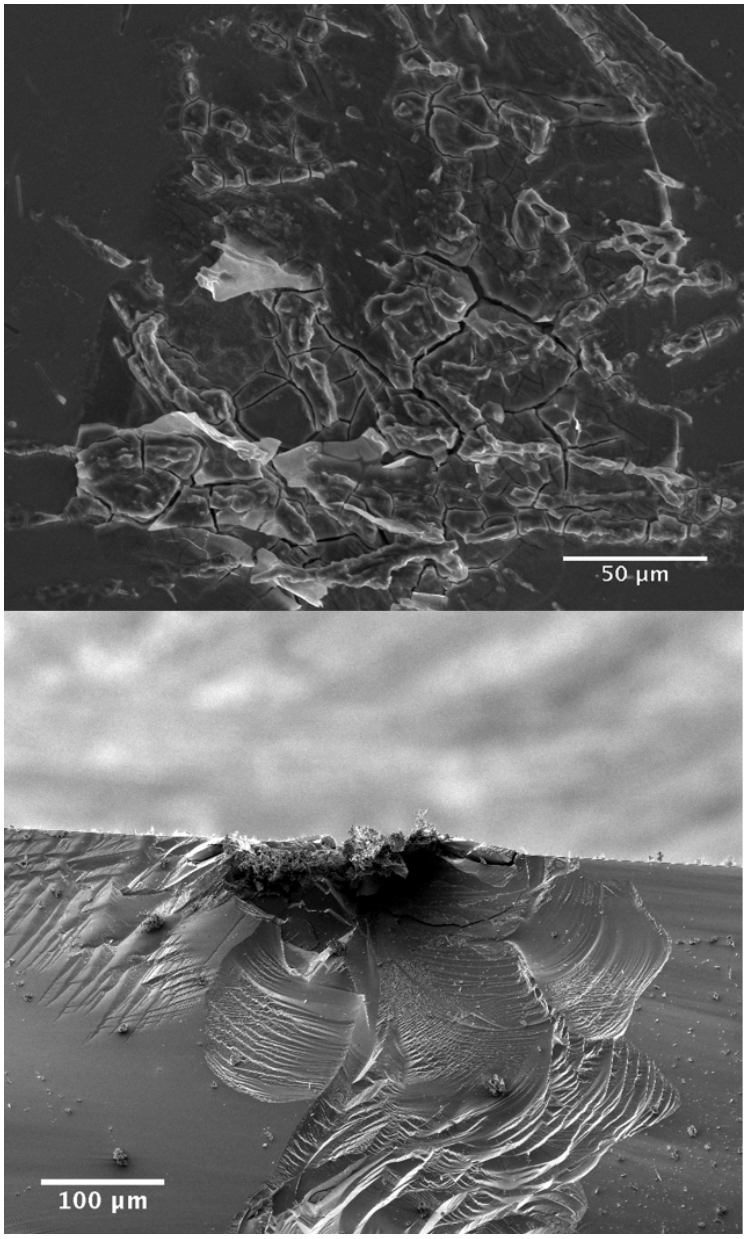

Figure 3.10: SEM images of device failure after 6.5 hours of operation. (top) cracking of ALD-TiO_2 protection layer and corrosion of underlying III-V semiconductors. (bottom) Cross section of III-V corrosion.

3.9 Stability of Large-Area Prototypes and Future Protection Strategies

The ~1 cm^2 protected III-V photoelectrodes used in the functioning prototype system were less photochemically stable than the protected III-V photoelectrochemical devices with smaller exposed surface area. One approach to mitigate this issue and create scalable devices is to mutually electrochemically isolate the defects, such as by use of nanostructured arrays. In this way, only small areas that possess a defect

will be etched, leaving the other structures in the device protected and operational.

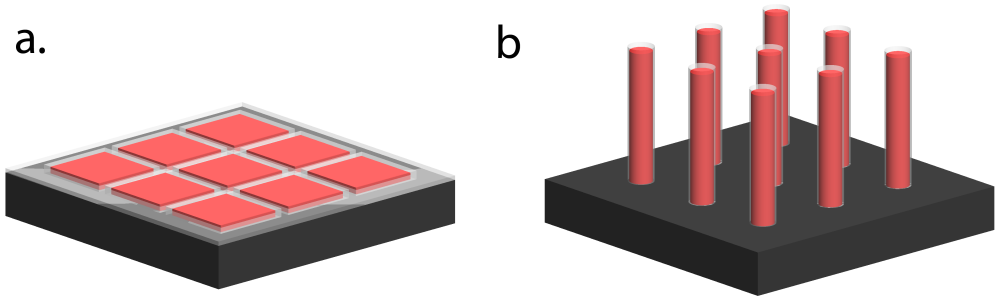

Figure 3.11: Protection scheme for chemically-isolated III-V structures on a self-passivating substrate using ALD-TiO_2. (a) Mesa-etched planar films. (b) Microwire/nanowire array.

One method is to mesa-etch planar III-V films that have been deposited on or wafer-bonded to a stable or self-passivating substrate (**Figure 3.11a**). This can be achieved by the combination of epitaxial liftoff (ELO) and wafer bonding. Recently this has been demonstrated for high-throughput fabrication of MOCVD-grown III-V films on Si [104], which has the potential to dramatically reduce the cost of creating an ideal bandgap combination for use in solar fuels.

A second strategy is to grow microwire or nanowire III-V semiconductors on Si (**Figure 3.11b**). Planar metamorphic growth of III-V films on a Si substrate is limited by defect propogation due to lattice mismatch, causing dislocations to propagate through the film [105]. III-V nanowire growth on Si relaxes strain due to the high surface-area-to-volume ratio of the sidewall surfaces of nanowires. This allows growth of high-quality single-crystalline III-V materials that allow for bandgap tuning to create a tandem partner with Si. Another benefit of high-aspect-ratio structures is lower photocurrent density over the internal surface area favors fuel production relative to corrosion, and thus enhances functional device lifetimes relative to planar structures operated under the same illumination [80]. This was further explored by work at the Joint Center for Artificial Photosynthesis (JCAP) using GaAs nanowires grown on Si substrates with a semiconductor/liquid junction formed in the ferrocenium/ferrocene redox couple ($FeCp_2^{+/0}$) in dry acetonitrile (CH_3CN) that contained lithium perchlorate as the supporting electrolyte [106]. This work was continued by coating the nanowires with ALD-TiO_2 and using a conformal NiO_x electrocatalyst [107]. In these structures, the radius of the nanowires was small enough to mitigate strain due to lattice mismatch of GaAs and Si, and

the protective TiO_2 film passivated the entire photoanode surface. The photoanode displayed resistance to corrosion and performed continuous water oxidation for over 200 h in 1.0 M KOH(aq) [107].

3.10 Summary and Outlook

A monolithically integrated device consisting of a tandem-junction GaAs/InGaP photoanode coated by an amorphous TiO_2 stabilization layer, in conjunction with $NiFeO_x$/NiMo earth-abundant active electrocatalysts for the hydrogen-evolution and oxygen-evolution reactions, was used to effect unassisted, solar-driven water splitting in 1.0 M KOH(aq). When connected to a Ni-Mo-coated counterelectrode in a two-electrode cell configuration, the TiO_2-protected III-V tandem device exhibited an η_{STH} of 10.5% under 1 sun illumination, with stable performance for > 80 h of continuous operation, and for 40 hours at an efficiency of η_{STH} > 10%. The protected tandem device also formed the basis for a monolithically integrated, intrinsically safe solar-hydrogen prototype system (1 cm^2) driven by a NiMo/GaAs/InGaP/TiO_2/Ni structure. The intrinsically safe system exhibited a hydrogen production rate of 0.81 μL s^{-1} and a solar-to-hydrogen conversion efficiency of 8.6% under 1 sun illumination in 1.0 M KOH(aq), with minimal product gas crossover while allowing for beneficial collection of separate streams of H_2(g) and O_2(g).

Future directions for these protection schemes with III-V devices include IMM devices to create more ideal bandgap combinations for increased efficiency, as well as mesa-etched structures and nanowires on stable or self-passivating substrates for corrosion resistance to promote longer device operation.

In addition, this work demonstrates the effectiveness of conductive ALD-TiO_2 films for use in any future device that requires stable photoanodes in corrosive environments, including CO_2 reduction for carbon-based liquid fuel production. The voltages we demonstrate would be ideal for fuel formation in CO_2R devices, which would benefit from combining a TiO_2-protected photoanode with a CO_2R cathode. This will be explored further in **Chapter 4** .

Chapter 4

BIPOLAR MEMBRANE DEVICES FOR SOLAR FUEL PRODUCTION

Content in this chapter is drawn from the following publications:

- Sun, K., Liu, R., Chen, Y., Verlage, E., Lewis, N. S. & Xiang, C. Solar-Driven Water Splitting: A Stabilized, Intrinsically Safe, 10% Efficient, Solar-Driven Water-Splitting Cell Incorporating Earth-Abundant Electrocatalysts with Steady-State pH Gradients and Product Separation Enabled by a Bipolar Membrane. *Advanced Energy Materials* **6,** 1600379 (2016).
  DOI: 10.1002/aenm.201670077
  Contribution: experimental design, III-V photoelectrochemical cell design and processing.
- Zhou, X., Liu, R., Sun, K., Chen, Y. K., Verlage, E., Francis, S. A., Lewis, N. S. & Xiang, C. X. Solar-Driven Reduction of 1 atm of CO_2 to Formate at 10% Energy-Conversion Efficiency by Use of a TiO_2-Protected III–V Tandem Photoanode in Conjunction with a Bipolar Membrane and a Pd/C Cathode. *ACS Energy Letters* **1,** 764–770 (2016).
  DOI: 10.1021/acsenergylett.6b00317
  Contribution: III-V photoelectrochemical cell design and processing.

4.1 Introduction and Motivation

Typically, laboratory-scale solar fuel devices have utilized a single electrolyte in both the anode and cathode compartments, necessitating compatible materials for use in each half-reaction. The devices described in **Chapter 1**, as well as our own highly-efficient and stable water-splitting device presented in **Chapter 3**, operate in either strongly acidic or in strongly alkaline electrolytes. This necessitates compatible material choices for cathodic and anodic reactions, and prevents desired combinations of OER and HER technologies.

In the absence of earth-abundant OER catalysts that are stable in acid, devices that operate in acidic electrolytes and use a Nafion membrane require the use of IrO_x or RuO_x. As described in **Section 3.3**, the lack of stable, earth-abundant electrocatalysts for oxygen evolution in acid [51] prevents the incorporation of useful materials for the HER in acid. For instance, an acid-stable photocathode like Si, combined with highly active, stable, and earth-abundant HER electrocatalysts

(like transition-metal phosphides) have the potential to dramatically decrease the cost of solar water splitting.

In this chapter we explore device architectures that allow a variety of different pH combinations for the anolyte and catholyte, and we create novel, efficient, and stable prototypes for water-splitting and CO_2 reduction.

4.2 Water Dissociation using a Bipolar Membrane

To ensure continual and intrinsically safe operation, scalable devices must include either a cation-exchange membrane (CEM) or an anion-exchange membrane (AEM) to provide proton and hydroxide-ion transport for acidic and alkaline media, respectively. Membranes with high ionic conductivities, such as Nafion in acid and SELEMION membranes in alkaline solutions, are used to separate the anode and cathode chambers to minimize product gas crossover.

Hybrid anion and cation exchange membranes are widely used in industrial electrodialysis processes to separate anions from cations in a salt solution. These bipolar membranes (BPMs) account for charge balance by performing water electrolysis at the interface between the AEM and CEM, producing protons and hydroxide ions. For charge balance, and to maintain a pH gradient between the two chambers, these systems split water to produce protons and hydroxide ions at the interface between the AEM and CEM [108, 109].

Recently the incorporation of BPMs with $BiVO_4$ photoanodes and Pt cathodes for light-assisted water splitting has been shown to maintain steady-state differences of 0-14 pH units and 0-7 pH units [110], showing much potential for the inclusion of BPMs in photoelectrochemical devices [108].

4.3 Cell Architecture Redesign

The current density and external quantum efficiency of both the solid state device and the photoelectrochemical device, shown in **Figure 2.4** and **Figure 3.5**, are not optimal and have much room for improvement.

Record dual-junction GaAs/InGaP devices in literature include double layer anti-reflection coatings (DL-ARCs) with optimized indices of refraction and thicknesses for a III-V layer stack. Many of these DL-ARCs are unstable in alkaline electrolyte or are unsuitable for operation in a planar PEC device. The solid-state measurements reported in Chapter 2 were obtained without any surface treatment or anti-reflection coatings, which results in reflection losses of ~30% for most wave-

lengths in the solar spectrum. The behavior of the photoelectrode benefits slightly from being submerged in solution that has a higher index of refraction than air, as well as from the TiO_2 coating which acts as a (sub-optimal) single-layer anti-reflection coating (ARC). A second cause of reduced EQE is parasitic absorption by the 7 nm GaAs contact layer, which absorbs photons that have energies above the band gap of GaAs (1.42 eV). The presence of this layer was needed to obtain facile for hole conduction through the TiO_2 protection layer, since ALD-TiO_2 grown on window layers that contained exposed aluminum did not exhibit the desired electrical properties. Simulations indicated that parasitic absorption of short wavelength light was especially detrimental to the performance of the high bandgap InGaP cell.

No.	Material	Thickness (nm)	Doping	Density (cm^{-3})	Dopant
14	GaAs	4	p^{++}	$>1 \times 10^{19}$	Zn
13	$In_{0.48}Al_{0.52}P$	30	p^{+}	3×10^{17}	Zn
12	$In_{0.49}Ga_{0.51}P$	70	p^{+}	1×10^{17}	Zn
11	$In_{0.49}Ga_{0.51}P$	530	n	1×10^{16}	Si
10	$In_{0.48}Al_{0.52}P$	10	n^{+}	1×10^{17}	Si
9	GaAs	20	n^{++}	$>2 \times 10^{19}$	Te
8	$Al_{0.3}Ga_{0.7}As$	20	p^{++}	$>2 \times 10^{19}$	C
7	$In_{0.49}Ga_{0.51}P$	20	p^{+}	5×10^{18}	Zn
6	$Al_{0.2}Ga_{0.8}As$	250	p^{+}	1×10^{18}	Zn
5	GaAs	2000	n	2×10^{17}	Si
4	$In_{0.49}Ga_{0.51}P$	30	n^{+}	3×10^{18}	Si
3	GaAs	300	n^{+}	5×10^{18}	Si
2	AlAs	150	n^{+}	1×10^{18}	Si
1	GaAs	50	n^{+}	5×10^{18}	Si
0	GaAs	Substrate	n^{+}	5×10^{18}	Si

Table 4.1: Epitaxial structure for dual-junction InGaP/GaAs III-V cell.

A re-design of the original multijunction III-V MOCVD growth on GaAs was performed using AFORS-HET simulations to avoid these losses in future devices and to ensure current matching of the InGaP and GaAs subcells. Additionally, these cell growths were designed to deliver increased voltages for use beyond water splitting in 1.0 M KOH. The InGaP n-type base was increased to 530 nm. In addition, the GaAs top contact layer was reduced to 4 nm in order to decrease the obscuration of the device after cell processing. The final structure from these simulations is shown in **Table 4.1**. In the rest of this chapter we use the tandem cell to drive water electrolysis and CO_2 reduction using bipolar membranes, where larger overpotential requirements will utilize the voltage supplied by the InGaP/GaAs structure.

4.4 High-Efficiency Water-Splitting Device Enabled by a Bipolar Membrane

Operation in lower pH has the potential to increase performance and stability for the water-splitting protection scheme described in **Chapter 3**. Substituting the anion exchange membrane with a bipolar membrane could allow near-neutral operation with the TiO_2 protection scheme while avoiding complications described in **Section 1.5**. This would also open up the possibility of using earth-abundant acid-stable HER electrocatalysts, which have no acid-stable OER pairing and could not be used in a purely alkaline device.

Using the improved III-V multijunction design, we created a sustained, intrinsically safe, efficient, solar-driven water-splitting cell based on CoP/H_2SO_4 (aq, pH = 0)/BPM/KBi (aq, pH 9.3)/Ni/TiO_2/InGaP/GaAs. The photoanode was coated by a 62.5 nm thick layer of amorphous ALD-TiO_2, optimized by optical modeling to minimize the reflection loss at the water/dielectric layer interface.

Counter electrodes were made from a Ti mesh coated by electrodeposition of CoP [111]. To minimize leaching of Co into the catholyte, the CoP counter electrode was electrochemically conditioned in a separate home-made cell with 1.0 M H_2SO_4(aq) in the dark using a three-electrode configuration, prior to transferring the cathode to the water-splitting cell. This electrochemical conditioning was conducted using cyclic voltammetry with a potential window of -0.15~0.05 V vs. RHE at a scan rate of 10 mV s^{-1} for at least 20 cycles, to remove excess Co metal in the Co phosphide film.

The catholyte was 1.0 M H_2SO_4(aq) and the anolyte was a 0.5 M potassium borate solution. The two electrolytes were separated by a bipolar membrane (fumasep FBM). The pH of the 0.5 M KBi(aq) solution was measured to be 9.3, and the SCE reference electrodes were calibrated in 0.5 M KBi(aq) using a reversible hydrogen electrode (RHE) fabricated from a homemade Pt disc in contact with a continuous purge of 1 atm of H_2(g). The equilibrium potential for water oxidation in 0.5 M KBi(aq) was therefore calculated to be 0.434 V vs. SCE.

A custom electrochemical cell with a flat glass (Pyrex) bottom was used for all of the 3-electrode (photo)electrochemical measurements (**Figure 4.1a**). Sample sizes in the 3-electrode measurement were typically ~0.2 cm^2. Two custom-made three-necked cells, with a flat quartz window for side-facing illumination and side connectors, were used in the 2-electrode BPM electrochemical measurements (**Figure 4.1b**). In addition to the stirring described above, a peristaltic pumping sys-

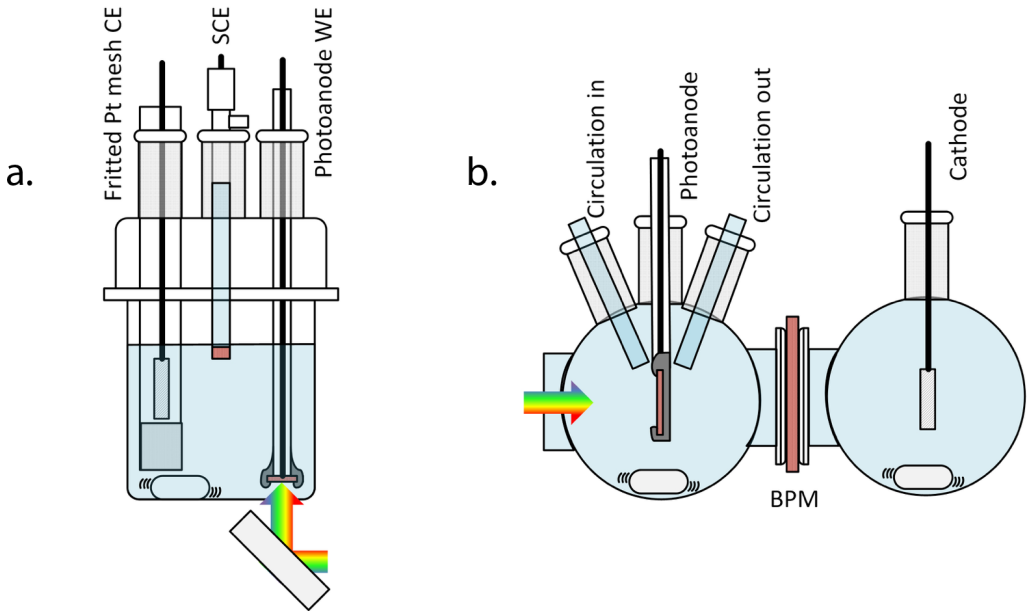

Figure 4.1: Schematic showing the BPM measurement setup for 3-electrode (a) and 2-electrode (b) electrochemical measurements.

tem (Simply Pumps PM300F) with a minimal flow rate of ~500 mL min controlled by a tunable power supply was used to facilitate the removal of bubbles from the sample surface and to minimize the dissolution of the Ni catalysts at near-neutral pH. Curved glass tubing was connected to the pump through polyimide tubing, and was placed close to the sample surfaces for efficient circulation.

The current density versus potential (J–E) behavior of a 0.23 cm^2 tandem-junction GaAs/InGaP/TiO_2/Ni photoanode in contact with the KBi solution is shown in **Figure 4.2a**, both in the dark and under simulated 1 sun illumination. For comparison purposes, **Figure 4.2a** also shows the J-E behavior of the OER using the TiO_2/Ni layers deposited onto a nonphotoactive p^+-Si substrate (p^+-Si/TiO_2/Ni), where the amorphous TiO_2 layer provided ohmic contacts with low contact resistance to the degenerately doped semiconductor as well as to the Ni metal catalyst. After correction for uncompensated resistance, an overpotential of ≈660 mV was required to drive the OER at a rate corresponding to 10 mA cm^{-2} of current density, using the activated thin Ni metal catalyst in contact with the 0.5 M KBi solution. The Ni metal catalyst required the application of an additional ≈300 mV overpotential when operated in KBi relative to the overpotential required to drive the OER at the same current density and catalyst loading in 1.0 M KOH(aq) shown in **Chapter 3**.

The photocurrent density of the GaAs/InGaP/TiO_2/Ni photoanode during a

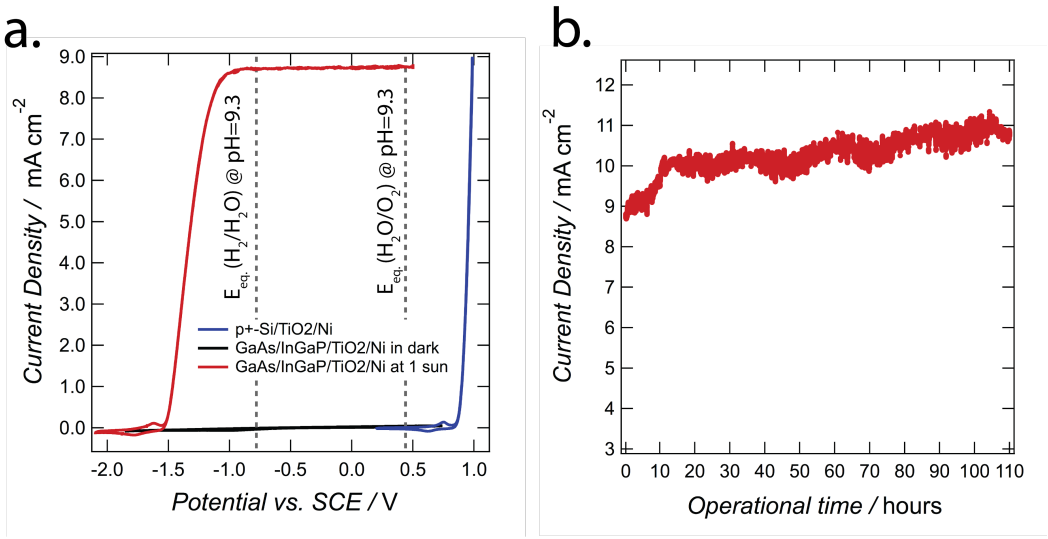

Figure 4.2: BPM water-splitting device performance in 3-electrode setup. (a) Cyclic voltammetry of a freshly prepared GaAs/InGaP/TiO_2/Ni photoanode in contact with a 0.5 M potassium borate buffer solution (KBi) at pH 9.3 in the dark (black) and under 1 sun of simulated solar illumination (red). The current density versus potential (J-E) characteristic for a non-photoactive p^+-Si/TiO_2/Ni electrode effecting the oxygen-evolution reaction under the same conditions is shown in blue. The equilibrium potentials at pH 9.3 for the oxygen-evolution reaction (OER) and the hydrogen-evolution reaction (HER) are indicated by the dotted lines. (b) The photocurrent density, J_{photo}, as a function of operational time for a GaAs/InGaP/TiO_2/Ni photoanode biased potentiostatically to -0.016 V versus a reversible hydrogen electrode (RHE) (blue dotted line).

100-hour stability test is shown in **Figure 4.2b**. It was biased potentiostatically at the formal potential for the OER (-0.016 V versus a reversible hydrogen electrode, RHE) while in contact with 0.5 M KBi(aq) and illuminated by a halogen lamp at 1 sun, in a three-electrode configuration with a standard calomel reference electrode (SCE) and a Pt mesh counter electrode. The photocurrent density at this applied bias, J_{photo} (–0.016), increased from 9.0 to 10.5 mA cm^{-2} during the 100 h test. After the 100 h stability test, the photoanode exhibited negligible change in onset potential or equivalent open- circuit voltage relative to the beginning of the test. The increase in J_{photo} (-0.016), particularly during the first 20 h of operation, may reflect changes in the refractive index and/or optical absorptivity of the Ni layer due to electrochemically induced changes in the morphology and thickness of the layer [100].

A schematic illustration of the BPM-containing device, with a 0.5 M KBi(aq) anolyte and 1.0 m H_2SO_4(aq) catholyte, is shown in **Figure 4.3a**. Dissociation

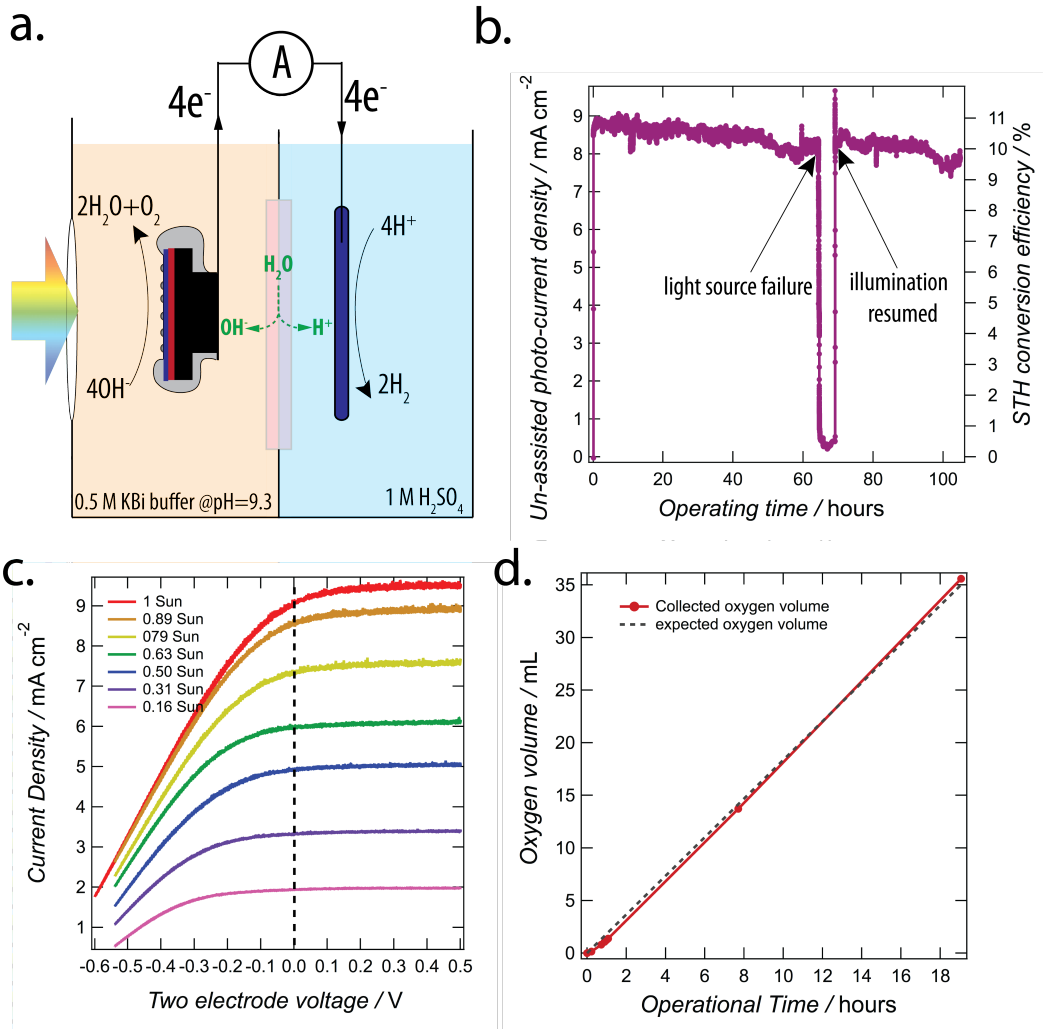

Figure 4.3: Bipolar membrane water-splitting device performance. (a) Schematic illustration of a spontaneous solar-driven water-splitting system that incorporates a BPM to maintain steady-state pH gradients. (b) The photocurrent density and corresponding solar-to-hydrogen conversion efficiency, η_{STH}, observed during unassisted water splitting using a BPM-containing GaAs/InGaP/TiO_2/Ni cell in a two-electrode con guration incorporating a CoP/Ti mesh cathode and under 1 sun of simulated solar illumination from a halogen lamp. The light source failed after ~70 h of operation and illumination was resumed ~5 h later. (c) Photocurrent density as a function of voltage applied between the GaAs/InGaP/TiO_2/Ni photoanode and a CoP/Ti mesh cathode at a range of illumination intensities. The short-circuit condition (i.e., with no applied bias) is indicated by the dotted black line. (d) The volume of oxygen produced as a function of time, as determined from gas-collection measurements (solid red line), and the volume of oxygen that would be produced based on the current passed as a function of time assuming 100% Faradaic efficiency for oxygen evolution (dotted line).

of water at the AEM-CEM interface within the BPM releases hydroxide ions and protons, which migrate into the anolyte and catholyte, respectively. When the rate of water dissociation in the BPM is equal to the rate of consumption of the protons and hydroxide ions at the electrode surfaces, a steady-state pH gradient is maintained. **Figure 4.3b** shows chronoamperometric (CA) data for a two-electrode BPM-containing cell using a 1.06 cm^2 area photoelectrode, a ~4.5 cm^2 BPM, and a Ti mesh/CoP counter electrode under 100 mW cm^{-2} of simulated solar illumination, with no external bias. The Ti/ CoP cathode exhibited a quantitative faradaic yield for H_2(g) evolution [111].

The electrocatalytic performance of the Ti/CoP cathode was separately characterized in a three-electrode electrochemical setup in 1.0 m H_2SO_4 (aq), and an overpotential of ~100 mV was observed at a cathodic current density of 10 mA cm^{-2} for the HER, comparable to previous observations for CoP. At the beginning of the measurement, $J_{photo}(0)$ was 8.2 mA cm^{-2}, which corresponds to a solar-to-hydrogen (STH) conversion efficiency, η_{STH}, of 10.0%. The current density and efficiency of this cell were lower than the performance expected from the short-circuit photocurrent density observed using smaller area (~0.2 cm^2) photoelectrodes (**Figure 4.2**), with the difference in performance for cells using the larger (1.06 cm^2) photoelectrode most likely resulting from the additional overpotential for the HER as well as the increased path length for ion transport around the edge of the larger electrode, which would increase the solution-based resistance losses in the cell. Nonuniformity or defects in the junction would also be expected to have a greater effect on larger-area electrodes, because larger samples should statistically contain a greater absolute number of defects than smaller electrodes. After 100 h of operation, $J_{photo}(0)$ decreased to 7.5 mA cm^{-2}, corresponding to a 9.3% relative decrease in η_{STH} over the 100 h period. At an operational photoelectrode current density of ≈ 8.0 mA cm^{-2}, the kinetic overpotentials for the OER and HER in the system were ≈ 600 and ≈ 100 mV, respectively. The membrane voltage loss, Vmembrane,loss, was ≈ 300 mV at the membrane current density (≈ 1.8 mA cm^{-2}) in the operating cell. Hence, the total voltage required to drive the water-splitting cell at ~8.0 mA cm^{-2} of photoelectrode current density was ≈1.23 + 0.6 + 0.1 + 0.3 ≈ 2.2 V, which was close to the photovoltage provided by the photodiode at that photocurrent density. At the current densities observed during the stability test, dissolution of the entire epilayer (InGaP/GaAs layer) of the photoelectrode at 100% Faradaic efficiency would require <2% of the total charge passed (see Supporting Information for calculation). Negligible change in the pH of the electrolyte in either compartment of the cell was

expected even if the BPM exhibited a substantial leakage current, because of the relatively large volume of the anolyte (15 mL) and the catholyte (15 mL) compared to the pH change expected in those volumes if every electron passed in the circuit were accompanied by transfer of a co-cation or a co-anion through the membrane.

The current density at various illumination intensities was recorded as a function of the two-electrode bias voltage applied to the BPM-containing cell (**Figure 4.3c**). At zero applied bias (black dotted line) and for lower illumination intensities (≤0.5 suns), $J_{photo}(0)$ approached the light-limited photocurrent density, resulting in an improvement in efficiency from η_{STH} = 9.6% under 1 sun illumination to η_{STH} = 10.4% at 0.5 sun illumination and to η_{STH} = 13.0% under 0.2 sun illumination. Under 1 sun illumination, $J_{photo}(0)$ = 7.8 mA cm^{-2} was close to the light-limited photocurrent density (8.2 mA cm^{-2}). Higher efficiencies could be reached by reducing the residual voltage losses in the cell. This can be accomplished by reducing the resistive losses from the membrane, reducing the solution resistive loss, or by improving the performance of the catalysts.

Figure 4.3d shows the volume of oxygen collected as a function of time from the anolyte, compared to the expected volume of oxygen that should be produced as a function of time based on the charge passed and assuming 100% Faradaic efficiency for oxygen evolution. A near-unity Faradaic efficiency for O_2(g) production at the photoanode was observed over the course of ~20 h of continuous operation in 0.5 M KBi(aq), suggesting minimal corrosion of the GaAs/InGaP/TiO_2/Ni photoelectrode under such conditions.

After 100 h of operation, while visible defects were observed on the large-area sample surfaces (~1 cm^2), these samples showed great improvements in stability over the device in alkaline media from **Chapter 3** . This is due to the fact that many of the III-V epilayers, including GaAs, InAlP, InGaP, and AlGaAs, have reduced dissolution rates in 0.5 M KBi(aq) compared to dissolution 1.0 M KOH(aq). Small pinholes formed around dust particles during cell processing in a non-cleanroom environment were once again the most likely cause of the decrease in efficiency. In separate experiments, the BPM was shown to maintain the pH gradient and had excellent stability in these solutions. The BPM was not one of the contributing sources to drops in performance over time.

A potential disadvantage of BPM-containing devices is the additional voltage requirement compared to similar devices that use earth-abundant catalysts. There were voltage losses due to the BPM resistive loss, as well as a loss for driving

electrodialysis at the FUMASEP FBM/anolyte and electrode/anolyte interfaces. For this device, the voltage loss across the FUMASEP FBM bipolar membrane was 400–500 mV at $J_{membrane}$ = 4.36 mA cm^{-2} and is expected to exceed 1.0 V at $J_{membrane}$ = 10 mA cm^{-2}. On top of this, the lack of unity permselectivity across the BPM will also eventually lead to electrodialysis of the solution, requiring active management of the buffer species and of the pH of the electrolytes to achieve true steady-state cell operation.

Additionally, while the Ni OER electrocatalyst is more stable in a borate buffer than with phosphate or bicarbonate buffers at pH 9.3, there are still issues with chemical corrosion. Oxidized Ni is partially soluble in pH 9.3 borate buffer, and eventually the electrocatalyst will be completely removed from the surface and/or the Ni species will contaminate the catholyte and membrane. An interesting option is to embed light absorbing materials inside the BPM. However, near the electrode surfaces local pH conditions will be either highly alkaline or highly acidic, canceling the benefit from operating in a buffered solution at near-neutral pH.

4.5 Bipolar Membrane Device for CO_2 Reduction

Just as in the case for solar water splitting, BPMs can enable the combination of electrolytes with different pH for the reduction of CO_2 into fuel. Devices that have a single electrolyte and by necessity perform the CO_2 reduction (CO_2R) reaction in neutral pH conditions have large overpotential losses for the OER, and suffer from similar issues described in **Section 1.5** for near-neutral water-splitting devices. Utilizing a BPM relaxes electrolyte constraints and allows use of Ni-based OER catalysts, which are not stable for OER at near-neutral pH. This allows for the incorporation of the photoanode from **Chapter 3** into a CO_2R system.

The ALD-protected GaAs/InGaP/TiO_2/Ni photoanode was used to perform the OER in 1.0 M KOH(aq) (pH = 13.7) and drive the reduction of CO_2 to formate. For the cathodic electrodes, Ti foils and mesh were coated with Pd/C nanoparticles designed to perform the CO_2R reaction in 2.8 M $KHCO_3$(aq) (pH = 8.0) under 1 atm of CO_2(g). Together with a bipolar membrane (fumasep FBM), these electrodes were used to create a full solar-driven CO_2R system with effective ionic coupling between the catholyte and anoylyte to create modest combined cell overvoltages at the desired operational current density.

As seen in the schematic illustration in **Figure 4.4a**, a dual compartment glass cell was used for the two-electrode electrochemical setup. A peristaltic pumping

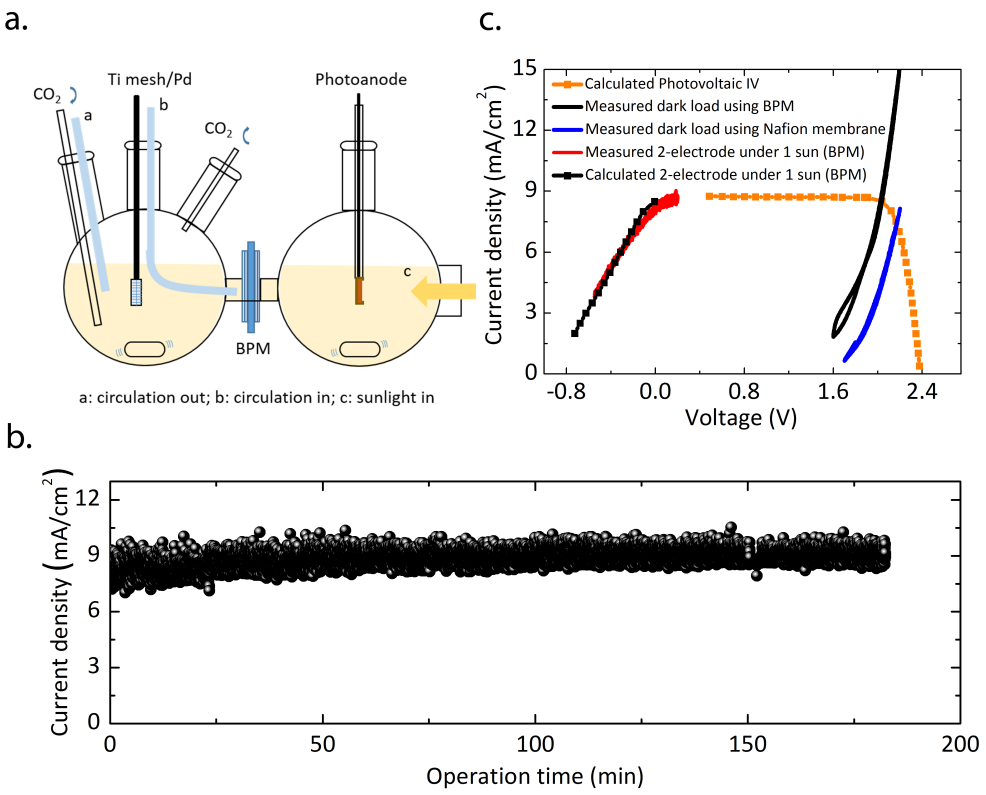

Figure 4.4: Solar-driven CO_2 reduction to formate using a bipolar membrane. (a) Schematic illustration of a two-electrode electrochemical setup. (b) The unassisted CO_2R current density as a function of operational time using a GaAs/InGaP/TiO_2/Ni photoanode and a Pd/C-coated Ti mesh cathode in a two-electrode electrochemical configuration under 100 mW cm^{-2} of simulated AM1.5 illumination. (c) The overall polarization characteristics for the $CO_2$2R reaction and the OER using a p^+-Si/TiO_2/Ni anode and a Pd/C-coated Ti mesh cathode in the two-electrode BMP configuration ($KHCO_3$/Nafion/KOH) (black) as well as in the two-electrode Nafion membrane configuration ($KHCO_3$/Nafion/$KHCO_3$) (blue). The measured (red) and calculated (black) two-electrode current-voltage behavior of the GaAs/InGaP/TiO_2/Ni photoanode wired to a Pd/C-coated Ti mesh cathode was measured under 100 mW cm^{-2} of simulated AM1.5 illumination. The calculated current density-voltage characteristic of the solid-state tandem cell (orange).

system, shown by the blue tubes in **Figure 4.4a**, facilitated removal of CO_2(g) bubbles from the electrode and membrane surfaces. CO_2 at 1 atm (ALPHAGAZ 1) was bubbled continuously into the 2.8 M $KHCO_3$(aq) catholyte. The geometric areas of the GaAs/InGaP/TiO_2/Ni photoanode, BPM, Nafion membrane were all 0.030, cm^2, and the Pd/C/Ti cathode was 0.040 cm^2. As in **Chapter 3**, the active area of the III-V device was kept small due to pinhole formation and corrosion

1.0 M KOH(aq), which prevented a larger photoanode area. The stability test in **Figure 4.4b** shows the current density for unassisted CO_2R under 100 mW cm^{-2} of simulated AM1.5 illumination. For these measurements, the GaAs/InGaP/ TiO_2/Ni photoanode was wired directly to the Pd/C nanoparticle-coated Ti mesh cathode with no external bias. The faradaic efficiency of CO_2 reduction to formate fuel was ~94% after 3 h, corresponding to a solar-to-formate efficiency (or, alternatively, a solar-to-fuel conversion efficiency, η_{STF}) of 9.9%.

Cyclic voltammetry (CV) sweeps and calculations of the current density vs. voltage behavior of the cell components are presented in **Figure 4.4c**. There is good agreement between the calculated (dotted black) and measured (red) two-electrode current density vs voltage behavior of the GaAs/InGaP/TiO_2/Ni photoanode wired to a Pd/C-coated Ti mesh cathode under 100 mW cm^{-2} of simulated AM1.5 illumination. The calculated behavior of the GaAs/InGaP/TiO_2/Ni photoanode was obtained by using the current-voltage behavior of the tandem solid-state photoabsorber (dotted orange) in conjunction with the overall polarization characteristic of a p^+-Si/TiO_2/Ni anode and a Pd/ C-coated Ti mesh cathode in the two-electrode BMP configuration ($KHCO_3$/BPM/KOH) (black). Notice the intersection of the dark load line using the BPM (black) with a region close to the maximum power point of the photovoltaic tandem junction component of the photoanode (orange) at an applied voltage of around 2.04 V, which indicates the buried junction cell is a good match for the voltage requirements of the CO_2R device. This is in contrast to the two-electrode Nafion membrane configuration ($KHCO_3$/Nafion/$KHCO_3$) (blue) using the same electrode materials, which has additional ~180 mV of voltage required for operation. Meeting these voltage demands would require a significant decrease in performance. Additionally, transport of K^+ between the anolyte and catholyte during steady-state operation using a Nafion membrane would also electrodialyze the electrolytes. While circulation of the electrolyte might potentially minimize the steady-state K^+ ion concentration polarization of the system, it would be difficult to separate formate from the catholyte due to low concentrations of the liquid product. The BPM causes robust product separation and allows for the production of a high concentration of formate.

4.6 Summary and Outlook

In this chapter bipolar membranes were incorporated into two photoelectrochemical solar fuel devices, maintaining a large pH gradient between anolyte and catholyte and allowing the stable pairing of previously incompatible half-cells and materials.

Although the BPM increased overpotential requirements with additional membrane voltage losses, it was shown to prevent product gas crossover and maintain the pH levels of each electrolyte.

First, unassisted and intrinsically safe solar-driven water splitting was demonstrated at η_{STH} = 10% for >100 h with a pH 9.3 anolyte and pH 0 catholyte for a >1 cm^2 tandem photoelectrode. For this device, the BPM prevented the need for an active and acid-stable OER electrocatalyst, and improved the stability of the larger area III-V photoanode by allowing operation in near-neutral conditions.

Returning to the high-pH conditions of the device in **Chapter 3** , a second BPM device performed solar-driven CO_2 reduction to produce formate at an η_{STF} of 9.9%. The tandem GaAs/InGaP/TiO_2/Ni photoanode in 1.0 M KOH(aq) (pH = 13.7) was used to drive CO_2 reduction using a Pd/C nanoparticle-coated Ti mesh cathode in 2.8 M $KHCO_3$(aq) (pH = 8.0) and 1 atm of CO_2(g). Again, the BPM was instrumental for allowing simultaneous operation in two different electrolytes, with a lower total overpotential and higher efficiency than any currently-available single-electrolyte CO_2 reduction cell.

These laboratory-scale devices demonstrate the many benefits that can be achieved by the incorporation of bipolar membranes and ALD-TiO_2-coated III-V photoanodes in future devices for solar-driven water-splitting and CO_2R reactions. While we have explored acidic/near-neutral and near-neutral/alkaline pH combinations, we did not explore the full pH range of pH 0/14 electrolytes, a combination that would entirely avoid the complications due to buffered solutions.

Chapter 5

IMPROVING DEVICE PERFORMANCE: OPTICAL WAVEGUIDES AND STRUCTURED CATALYST ISLAND ARRAYS

The III-V photoanode surfaces presented in the previous chapters have shown impressive stability in alkaline and near-neutral conditions. However, when it comes to light absorption and electrocatalyst transparency/stability, there is much room for improvement. The thin, optically-transparent Ni films used for operation in 1.0 M KOH in **Chapter 3** and **Chapter 4** degraded over time and caused a decrease in performance, and limits light management on the III-V surface.

Light management is a challenge not only for III-V photoanodes but for any fully-integrated PEC device that combines electrocatalytic and light-absorbing components. A new approach that does not require thin and/or transparent electrocatalysts would alleviate many constraints on device design. Beyond improving Ni-based photoanodes for solar water splitting, such a scheme could dramatically increase the performance of CO_2 reduction photocathodes, where large overpotentials require an increase in catalyst loading, making transparency difficult. Creating a general-purpose light management scheme, one that can incorporate thick and/or non-transparent catalysts while not obscuring the device, would increase the efficiency of a wide range of architectures.

In this chapter we explore strategies for light management on planar photoelectrodes. First we explore a novel dielectric waveguide array that allows large area (>50%) coverage of thick, non-transparent electrocatalyst on PEC surfaces. Second, we design a conventional antireflection coating that can be combined with catalyst islands or a structured catalyst array. Finally, we perform simulations that compare the performance of these light management designs. We will find both strategies have the potential to increase electrocatalyst lifetime under operating conditions, and to significantly enhance light absorption while decreasing overpotential requirements.

5.1 Waveguide Modes in Cylindrical and Conical Nanostructures

As was previously discussed at the end of **Chapter 3** , broadband absorption can be achieved using sparse (<5% fill fraction) arrays of GaAs nanowires on Si for use in photovoltaics and photoelectrochemistry, reducing material usage and improving performance relative to thin film or bulk materials [106].

The light-trapping properties of these high-index nanowire arrays are due to robust coupling into waveguide modes of individual nanowires. These waveguide modes lead to absorption peaks that are dependent on the dimensions of the wire. Arrays of nanowires with different radii can be used to create multiple absorption peaks, enhancing absorption above the band edge of the semiconductor [112, 113]. Further, the scattering cross section of each wire at its peak absorption wavelength is large enough to absorb most of the incoming radiation [112].

For a single, infinitely long cylindrical dielectric waveguide in air, the eignenvalue equation derived from Maxwell's equations (**Equation 5.1**), describes the waveguide mode resonances:

$$\pm\left(\frac{1}{k_{cyl}^2-k_{air}^2}\right)^2\left(\frac{k_z m}{k_0 a}\right)^2=\left(\frac{\epsilon_{cyl}}{k_{cyl}}\frac{J_m'(k_{cyl}a)}{J_m(k_{cyl}a)}-\frac{1}{k_{air}}\frac{H_m'(k_{air}a)}{H_m(k_{air}a)}\right)\times\left(\frac{1}{k_{cyl}}\frac{J_m'(k_{cyl}a)}{J_m(k_{cyl}a)}-\frac{1}{k_{air}}\frac{H_m'(k_{air}a)}{H_m(k_{air}a)}\right) \tag{5.1}$$

where a is the cylinder radius, ϵ_{cyl} is the complex permittivity of the cylinder, k_0 is the free space wavevector, k_z is the wavevector along the cylinder axis, k_{cyl} and k_{air} are the transverse components of the wavevector in the interior and exterior of the cylinder, respectively, m is the azimuthal mode order, and J_m and H_m are the mth order Bessel and Hankel functions of the first kind, respectively [114].

In sparse arrays of high-index nanowires, the modes responsible for the enhancement in absorption arise from the waveguide modes of individual wires, and these modes are only slightly perturbed by the lattice [114, 115]. For m > 0, mode solutions are HE (magnoelectric, TM-like) or EH (electromagnetic, TE-like). These modes are labeled as EH_{mn} or HE_{mn}, where m is the azimuthal and n is the radial mode number.

Previous simulations have shown that tapering of GaAs nanowires into vertically-oriented nanocones increases absorption of the AM1.5 spectrum, resulting in a 3%

increase in absorbed photocurrent compared to multi-radii nanowire arrays [112]. The gradual change in radius down the length of the cone creates enhanced absorption at specific heights for each wavelength. By modifying the tip and base radius, this can be tuned for optimal broadband absorption above the band edge of GaAs.

While light absorption inside semiconductor wire/cone arrays decreases material costs due to low filling fraction of expensive III-V materials, there are many constraints on the available bandgaps and on the optoelectronic properties for these structures. In order to achieve high efficiency, this normally requires growth of high-quality semiconductors on lattice-mismatched substrates. Manufacturing processes for these structures will vary depending on substrate material, and are further complicated by the necessary deposition of electrocatalyst, which could lead to obscuration of the wire array or of the underlying substrate.

However, coupling into waveguide structures also occurs below the band edge of the semiconductor; this provides an opportunity to use waveguide modes for transmission directly into the underlying substrate. In the rest of this chapter, we explore high-aspect-ratio dielectric nanocones which have the potential to dramatically increase light absorption on the surfaces of planar PEC and PV devices.

5.2 Broadband Transmission Through Optically Thick Metal Films

For planar devices, a novel solution to the issue of catalyst obscuration of photoelectrode surfaces is to transmit light directly to the semiconductor film through a dielectric waveguide. Coupling into waveguide modes of high-index dielectric nanostructures (as discussed in the previous section) would allow confinement of incoming light in order to bypass opaque electrocatalysts on the surface of the device, creating a general light management scheme for use on any planar photosurface. Such a scheme could allow a large increase in geometric filling fraction of opaque electrocatalysts on electrode surfaces, increasing the efficiency of many existing architectures. Ideally, the incorporation of these dielectric structures would not interfere with protection schemes used to stabilize high-efficiency PEC devices.

Dielectric nanostructures for broadband absorption in semiconductor devices have been explored for many optoelectronic applications. These structures include nanocones [116], nanopillars [117, 118], nanowires [119–121], inverted pyramids [122], nanodomes [123], nanoshells [124], and nanospheres [125]. For many of these structures, electrical conductivity at the interface is achieved by depositiong transparent conducting materials, such as sputtered indium-doped tin oxide (ITO),

which is not stable in many electrolytes.

One of the most notable nanostructured surfaces with increased optical performance and high conductivity uses a patterned Au film on Si to perform metal-assisted chemical etching, creating square Si nanopillars with small aspect ratios. Together with a 50 nm SiN_x antireflection coating, this structure displayed very high absorptance (> 90%) in both simulation and experiment, while achieving high surface conductivity across the 16 nm Au film that covered 65% of the Si surface [118]. However, this method is very dependent on the chemical process that allows the selective etching of the underlying semiconductor. Also, in previous experiments on Au-coated photoanodes, we found catalytic films like Pt and Ni lifted off from Au surfaces during operation in 1.0 M KOH, even with a Ti adhesion layer. This was due to a slow etching of the Au film. It would be useful to create a dielectric structure that is decoupled from other device components and does not require modification of the underlying cell or of the semiconductor/catalyst interface.

We will explore a more universal approach to the deposition of high-index dielectric waveguides on planar electrode surfaces. The deposition process for these nanostructures will be generally compatible with current device fabrication, and will allow large surface area coverage of optically thick metal films.

5.3 Transmission Through Thick Ni Films Using Two-Photon Lithography

In order to confirm increased transmission through a thick metal film using waveguide modes in dielectric nanocones, an initial experiment was conducted to determine the correct dimensions for optical coupling of the visible spectrum, and to verify transmission through the cone/substrate interface. Nanoscribe IP-Dip, a liquid photoresist for high resolution two-photon lithography, was selected for the ability to rapidly print complex structures, as well as the potential for replicating these structures with other dielectric materials using nanoimprint lithography [126].

However, the smallest feature size for this photolithographic process was on the order of ~200 nm, which presented a barrier to reliable writing of high-aspect-ratio nanostructures with a fine tip. Initial attempts to produce a sharp tip resulted in rounded features. Post-processing of the structures were used to reduce the tip radius below the voxel size.

Figure 5.1 shows cell processing to create dielectric structures surrounded by a metal hole array of non-transparent catalyst. This process allows for the deposition of the nanocone arrays with electrodeposited Ni film, as well as a method for

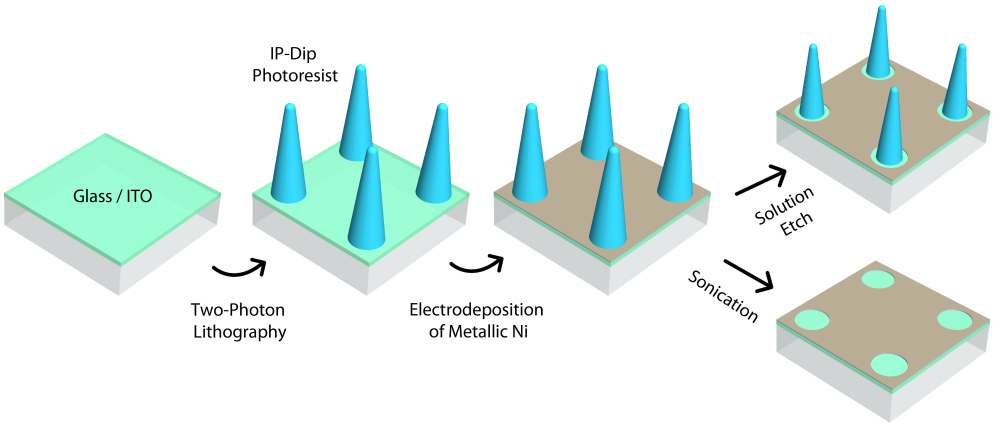

Figure 5.1: Overview of nanocone array cell processing steps. Photoresist structures for light management on electrode surfaces are created using two-photon lithography and electroplated Ni OER electrocatalyst.

comparing the optical properties of the empty Ni hole array after removal of the photoresist cones. Glass/ITO was selected as a substrate to easily electrodepsit the metal electrocatalyst, and allowed optical measurement of transmission through the metal film. The ITO thickness used in all measurements was 150 nm.

An added benefit of the final etching process shown in **Figure 5.1** is the buffer zone left between the dielectric cones and the Ni electrocatalyst (see **Figures 5.4** and **5.11**). Since the electric fields of waveguide modes decay away from the nanocone outer radius, this buffer zone prevents absorption in the metal film.

Geometric filling fraction of metal catalyst on the electrode surface, f_c, is defined as the ratio of the geometric area of the catalyst to the total geometric area of the photoelectrode.

Figure 5.2a shows an SEM image of the IP-Dip cones on ITO before metal electrodeposition. These cones have larger feature sizes than our simulations. **Figure 5.2b** shows reflectance measurements performed in an integrating sphere setup. There is a significant change in reflectance, shown in **Figure 5.2b**, compared to bare Glass/ITO, that has an onset around 800 nm. The reason for this change is the scattering cross section of the nanostrucutres that causes increased reflection at the back surface of the ITO and the glass slide. Light travels out of the edges of the glass slide and are collected by the detector, and is therefore not transmitted to the photon sink. **Figure 5.2b** shows us which wavelengths of light are affected by the IP-Dip structures.

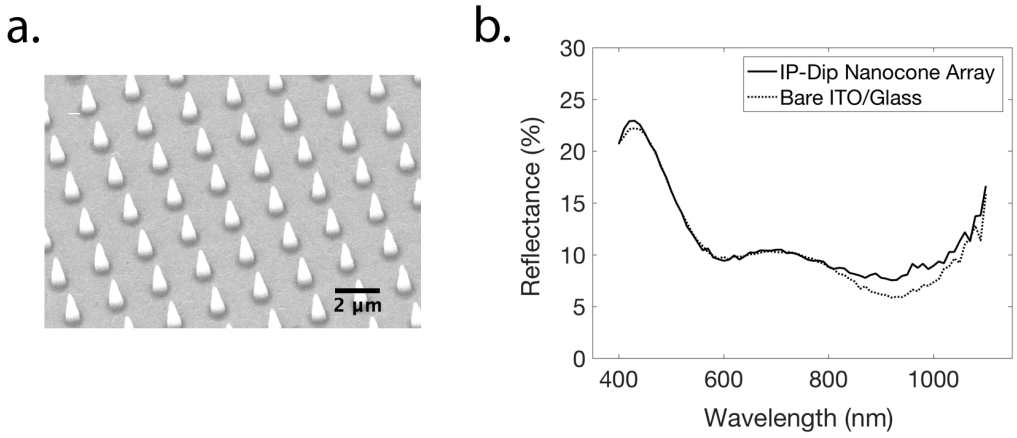

Figure 5.2: IP-Dip photoresist cone array on Glass/ITO substrate. (a) SEM image of nanocone array, base radius ~350 nm (b) Integrating sphere measurement performed on glass slide which shows increased reflectance from $\lambda \approx$ 800-1100 nm due to nanocone array.

Finite-Difference Time-Domain (FDTD) simulations of the structures after Ni deposition are shown in **Figure 5.3**. **Figure 5.3a** is a schematic of the dimensions that were used for the FDTD simulations. These dimensions were selected based on expected coupling radii into a cone with an index of refraction of ~1.52, the index of IP-Dip photoresist. **Figure 5.3b** shows the optical properties of these surface films. For λ > 500 nm, transmission through the Ni film increases significantly and exceeds the 6-8% expected for an empty Ni hole array.

This increase in transmittance is due to the waveguide modes of the structure. A vertical cross section of the averaged electric field intensity profiles is shown in **Figure 5.3c** for λ = 400-1000 nm in 200 nm increments. For each wavelength, coupling occurs at specific radii along the cone and propagates down the length of the waveguide, funneling into the glass/ITO substrate.

Simulations were also performed with a plane wave source originating inside the glass substrate directed at the underside of the nanocone surface to observe the escape of reflected beams. The IP-Dip cones did not cause any increase in transmission through the reverse structure, both for the bare ITO surface and for the Ni hole array.

The ITO surfaces were contacted using conductive Cu tape and dipped into a Grobet CES Nickel-Mirror electroplating solution. After an initial sweep to -1.4 V vs. SCE, metallic Ni was electrodeposited for ~5 min at 0.8 mA/cm^2 and -1.1 V vs.

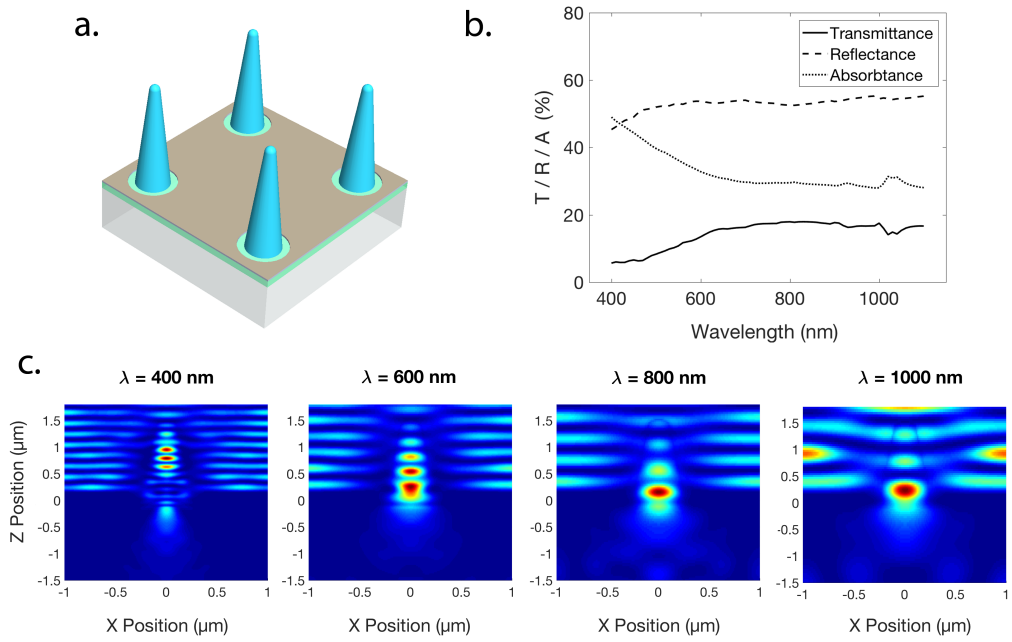

Figure 5.3: Finite-Difference Time-Domain simulations of IP-Dip nanocone array. (a) Tip radius of 100 nm and base radius of 250 nm, height 1.5 μm, square array with a 2 μm pitch. Ni and ITO thickness 50 nm and 150 nm, respectively. (b) Transmittance, reflectance, and absorptance simulations as a function of wavelength. (c) Vertical cross sections of simulated electric field intensity showing coupling into waveguide modes in the structure (arbitrary units).

SCE. During this process, the photoresist structures were slowly etched, decreasing the tip radius of the structure and pushing the expected waveguide modes further into the visible. **Figure 5.4** shows the structures after Ni electrodeposition. The structures were measured to have a base radius of ~250 nm, tip radius of ~100 nm, and were approximately 1.5 μm tall. As seen in **Figure 5.4a-c**, deposition did not occur in the area surrounding the base of the cone. The Ni hole created by this region had a radius of ~350 nm, which corresponds to the initial dimensions of the IP-Dip cone base. In **Figure 5.4c** the remnants of the photoresist can be seen around the base of the cone.

Twenty minutes of sonication in IPA solution was used to remove the photoresist from the Glass/ITO surface, as shown in **Figure 5.4d**. The resulting Ni hole array is shown in **Figure 5.4e**.

All measurements of transmission through Glass/ITO/Ni, for the nanocone

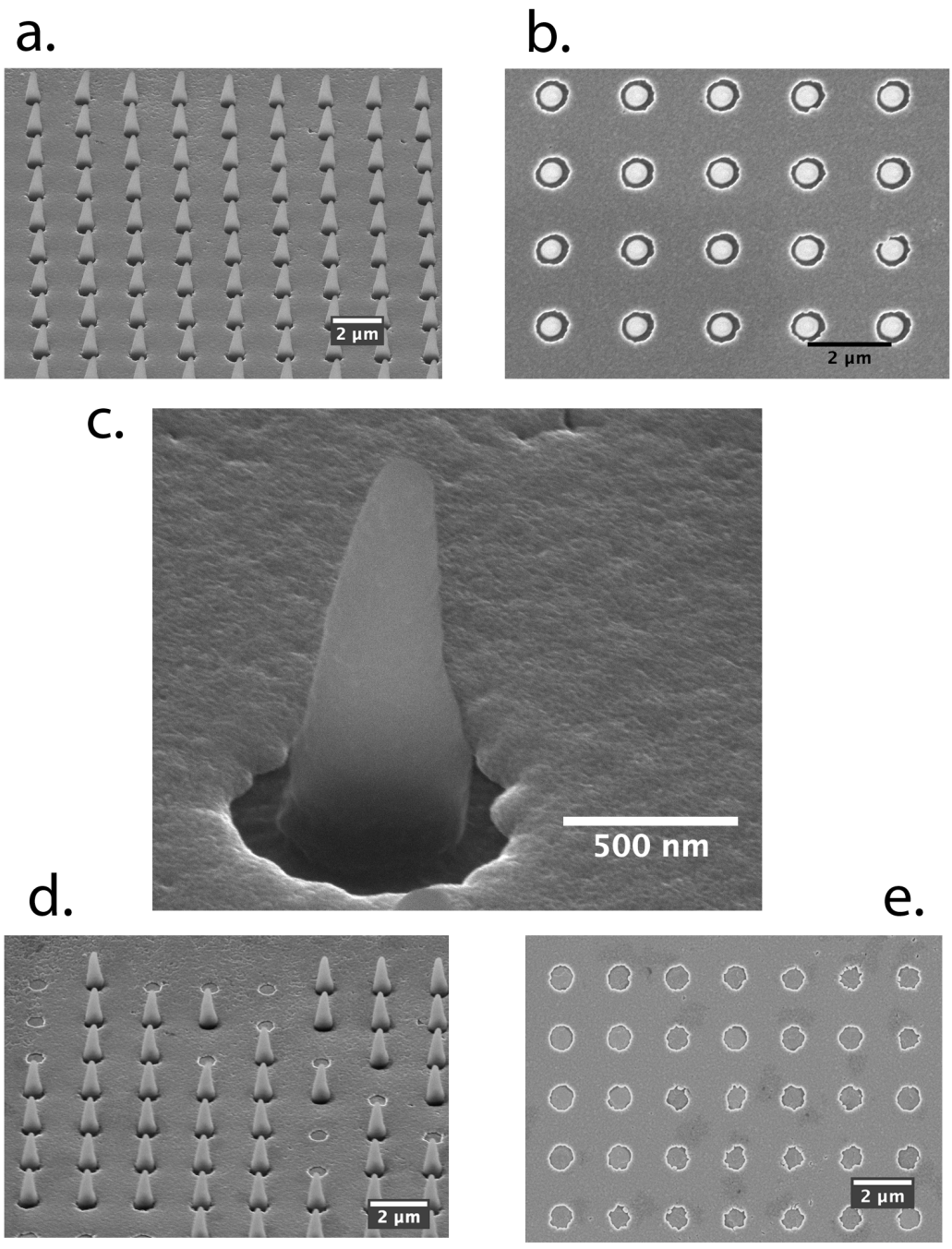

Figure 5.4: SEM images of IP-Dip nanocone array after Ni electrodeposition process. (a,b,c) 1.5 μm tall nanocones in 2 μm square array. Tip radius ~100 nm, base radius ~250 nm, and Ni hole radius ~350 nm. (d) Sonication process for removal of nanocones. (e) Ni hole array after IP-Dip removal.

and Ni hole arrays, were performed using an integrating sphere, as a function of illumination wavelength. These results are summarized in **Figure 5.5**, which

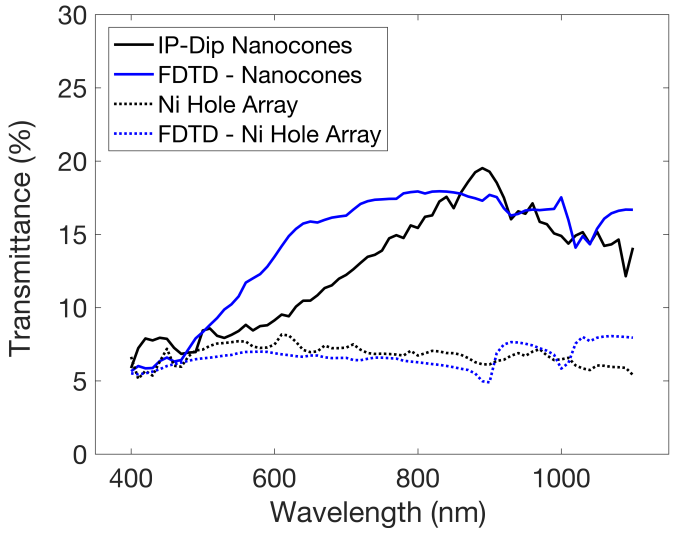

Figure 5.5: Transmittance through square array of IP-Dip nanocones on Glass/ITO surrounded by optically opaque ~110 nm thick Ni hole array. Integrating sphere measurements are shown in black, FDTD simulations in blue.

compares the transmittance measurement and simulation for both the nanocone and empty hole arrays.

These results show a >2-fold increase in transmittance for the nanocones compared to a corresponding Ni hole array in the λ = 850-1100 nm wavelength regime, and verifies beam coupling into waveguide modes that leads to transmission through the ITO layer into the underlying substrate. There is reasonably good agreement between simulation and experiment above λ = 850 nm, as well as for transmission through the Ni hole array. The discrepancy between FDTD simulation and experiment in the λ = 500-850 nm range is most likely due to inhomogeneity in the shape of tips of nanocones. This initial experimental result showing coupling into waveguide modes is in agreement with simulation and supports this approach as a promising direction for light management on PEC surfaces.

So far, we have increased transmission through a large catalytic filling fraction $f_c \approx 0.9$ using a sparse array of nanocones. By moving to a lower f_c and switching from a square to a hexagonal array, broadband transmission to the substrate can be increased well above 20% in the visible/near-IR. Nanocone height is also a parameter that plays a significant role in light coupling, as it is important for there to be a gradual transition between resonant radii. In the following sections we will show that increasing the aspect ratio of these structures enhances performance.

5.4 Hexagonal Array of IP-Dip Photoresist Nanocones

Next we performed FDTD simulations using high-aspect-ratio IP-Dip conical arrays to examine the effect of hexagonal pitch on transmission of light through the thick Ni film.

Figure 5.6 shows the simulation schematic and results. A height of 3 μm was chosen, and small 50 nm tip radius ensured coupling for short wavelengths into the guided modes. **Figure 5.6a** shows the increasing hexagonal pitch used in the simulations. As in previous simulations, a Ni hole array with a slightly larger radius (300 nm) was used. As a reference, in **Figure 5.6c** we plot pitch vs. geometric catalyst filling fraction f_c for the increasing hexagonal grid, where increasing pitch results in larger catalytic surface area.

As can be seen in **Figure 5.6b**, there is high transmission to the ITO surface for moderate values of f_c. In contrast, the conical array spaced at a 1.3 μm pitch with f_c = 81% shows high transmittance (>80%) from λ = 700-950 nm. Compare these results to simulations in **Figure 5.7** that use a bare Ni hole array, where even a close-packed hexagonal array does not result in high broad-band transmittance. The wavelength- and pitch-dependent features in transmission for the Ni hole array in **Figure 5.7b** are probably due to a combination of plasmonic modes and extraordinary optical transmission (EOT) [127–130], further complicated by the presence of the thin ITO layer. The rightmost band that starts at λ = 800 nm in **Figure 5.7b** disappears when the Glass/ITO substrate is replaced with a thick ITO substrate, leaving only the single band that starts at λ = 500 nm.

Additional wavelength and pitch-dependent diffraction bands are also observed in the presence of the nanocones due to the sub-wavelength spacing of the hexagonal lattice. The presence of the low-index (n $\approx$ 1.5) dielectric structures causes large oscillations in transmission and reflection due to the periodic nature of the waveguide array. Reflection bands mirror the transmission results, and correspond to a sharp increases in absorption in the Ni film, which absorbs ~40% of of the incident beam.

These features are most likely due to the low index of the photoresist which causes insufficient coupling into waveguide modes of the structure, which is detrimental for transmission to the surface. Since all simulations so far have been performed outside of solution (n = 1), this problem will only be exacerbated for measurements in solution, where the index contrast will be even less pronounced.

In order to design surfaces with broadband absorption on fully-immersed PEC

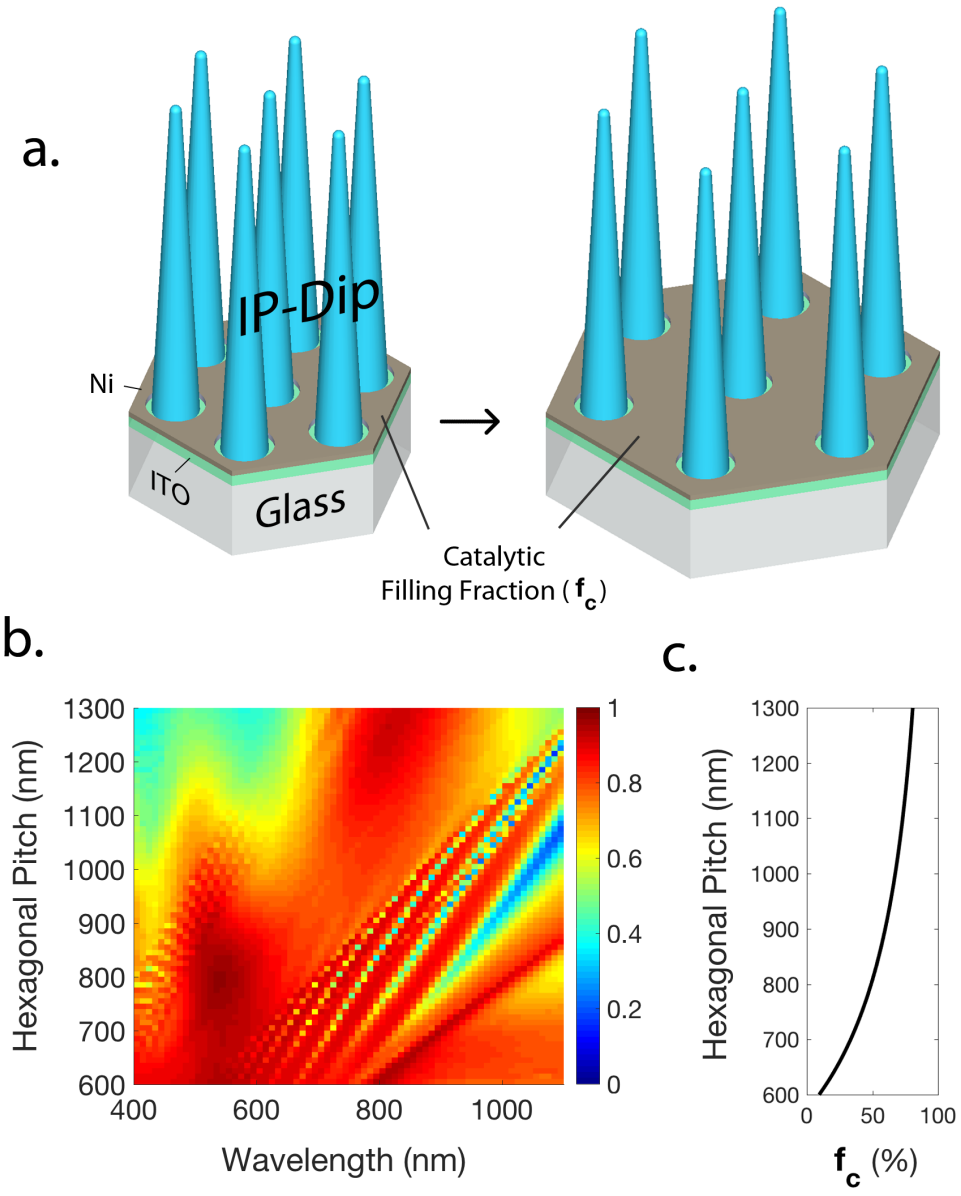

Figure 5.6: FDTD simulation of high-aspect-ratio IP-Dip nanocones in a hexagonal array of variable pitch on Glass/ITO. (a) Diagrams of 3 μm tall IP-Dip structures with 50 nm tip radius and 250 nm base radius with increasing lattice pitch of hexagonal array. Ni metal hole array with 300 nm radius and 50 nm thickness; 150 nm thick ITO film. (b) Plot of transmittance through the metal film as a function of wavelength and pitch. (c) Geometric filling fraction of catalytic surface area (f_c) for the corresponding hexagonal pitch.

surfaces, nanocone designs require a dielectric material that is high-index, transparent, earth-abundant, stable in solution, and can be deposited on planar surfaces using scalable methods.

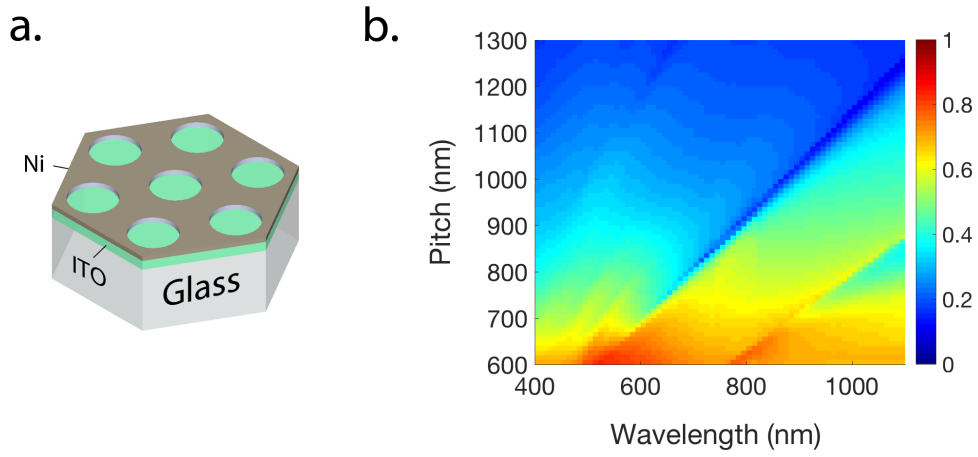

Figure 5.7: FDTD simulation of Ni hole array on Glass/ITO (a) Schematic of 50 nm thick Ni film hole array (r = 300 nm) and planar ITO film (150 nm), with increasing pitch size. (b) Transmittance through the metal array into the Glass/ITO substrate.

5.5 FDTD Simulations of TiO_2 Nanocones for Light Management on Si Surfaces

A promising candidate material to create these optical waveguides for use on PEC devices, TiO_2 has a higher refractive index than most dielectrics that were considered. Its refractive index can vary from around n = 2.1 for ALD TiO_2 to upwards of n = 2.6 for complex 3D photonic nanostructures fabricated using liquid-phase deposition [131]. It has a large band gap, is resistant to corrosion in both acid and base, and its previous use as a hole-conducting protection scheme and as an antireflective coating would facilitate adhesion of these TiO_2 structures to all previously reported ALD-TiO_2-coated surfaces.

FDTD simulations were performed for high-index TiO_2 nanostructures on Si. **Figure 5.8** shows the side-by-side comparison of transmittance through a TiO_2 nanocone array and Ni hole array on Si, with **Figure 5.8b** in air, and **Figure 5.8c** in solution.

The higher index of TiO_2 compared to IP-Dip photoresist increases coupling into waveguide modes. The index contrast between TiO_2 and Si is less severe than it would be with lower index materials, but simulations of TiO_2 nanocone arrays on an index-matched TiO_2 substrates show nearly identical transmission to those of **Figure 5.8b**, indicating that confinement in waveguide modes is more important than index matching of the Si-dielectric interface .

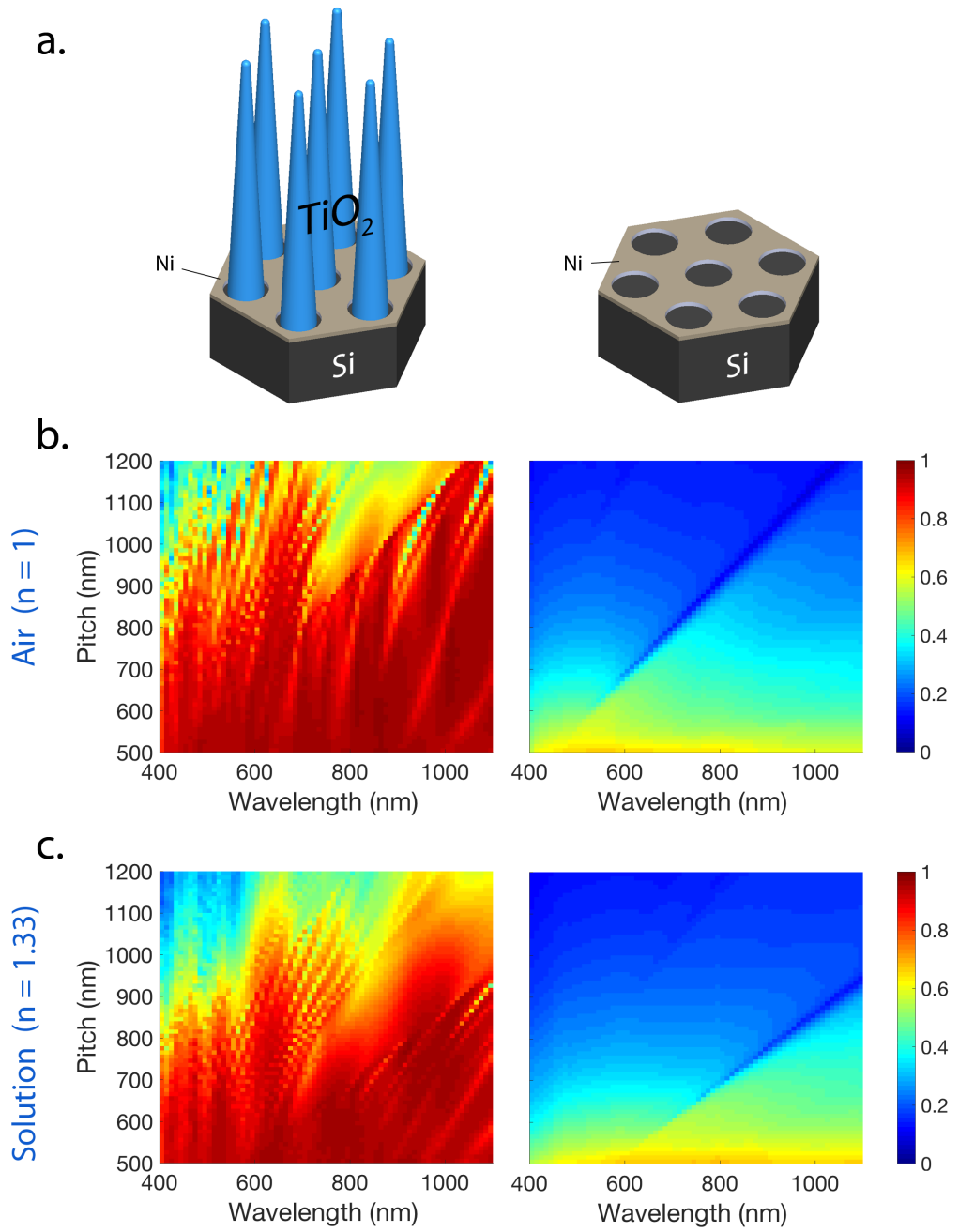

Figure 5.8: Light management using high-aspect-ratio TiO_2 nanocones on Si. (a) Schematic of nanocone array (left) and Ni hole array (right) for FDTD optical simulations. Nanocone height 2.5 μm, base radius 200 nm, tip radius 50 nm, Ni film thickness 50 nm. (b,c) Transmittance to the Si surface in air and in solution for nanocone array (left) and Ni hole array (right).

A disruption of the gradual slope of increasing radius down the length of the conical structure is shown in **Figure 5.9**, and causes a drastic reduction in

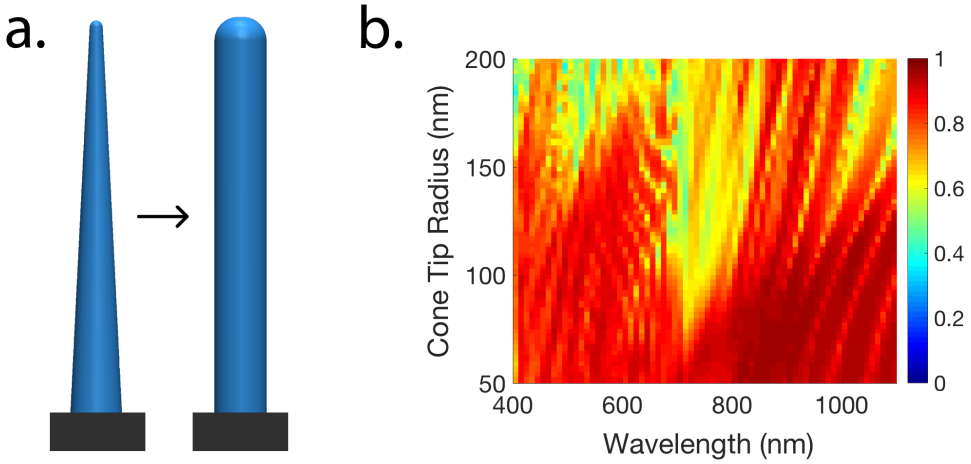

Figure 5.9: Transmittance to Si surface with varying nanocone tip radius in solution. (a) Hexagonal array (700 nm pitch) of 2.5 μm tall structures with r = 200 nm base surrounded by Ni hole array with r = 250 nm. Rounded tip radius ranged from 50-200 nm. (b) FDTD-simulated transmittance as a function of tip radius vs. wavelength.

transmission. The tip radius was increased from 50 to 200 nm to showcase the effect of a wider rounded tip. Simulations performed using truncated conical structures showed even more severe decrease in transmission, especially for short wavelengths.

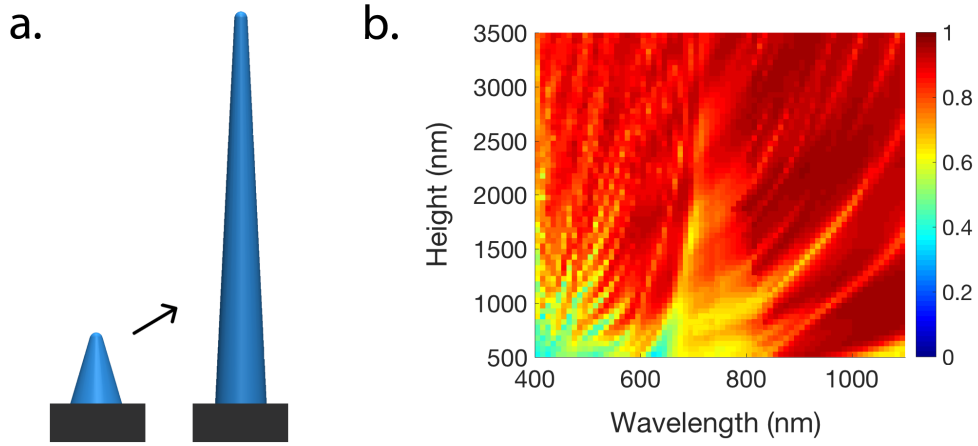

Figure 5.10: Transmittance to Si surface varying nanocone height in solution. (a) Hexagonal array (700 nm pitch) of 500 nm - 3.5 μm tall structures with r = 200 nm base and r = 50 nm tip surrounded by Ni hole array with r = 250 nm. (b) FDTD-simulated transmittance as a function of height vs. wavelength.

In **Figure 5.10** we vary the nanocone height from 500 nm to 3.5 μm. While high-aspect-ratio structures are beneficial for transmission to the electrode surface, there is not a significant reduction in the broadband waveguide coupling phenomenon

until around 1.5μm. Below this height, transmission in the 400-800 nm range shows a steady decline. For scalable fabrication processes, lower aspect ratio nanocones would present many advantages, including lower material costs and increased durability.

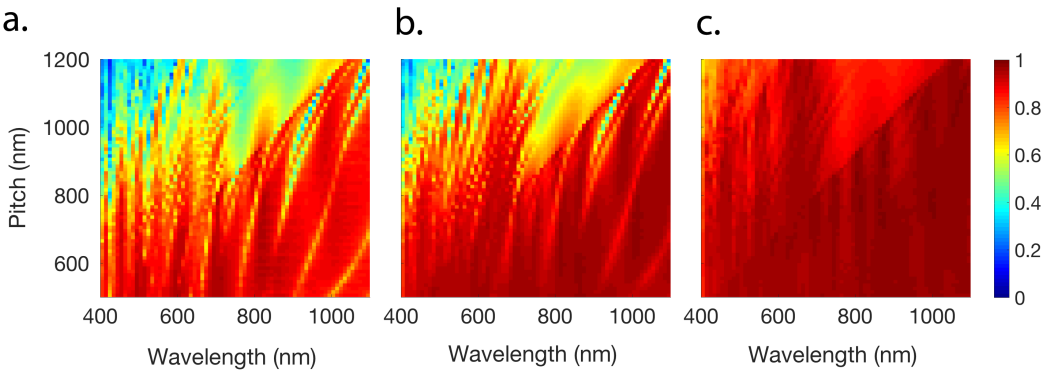

Figure 5.11: Effect of Ni film on transmission to Si through TiO_2 nanocone waveguides in air. Hexagonal array (700 nm pitch) of 2.5 μm tall cones with r = 200 nm base and r = 50 nm tip with (a) r = 200 nm and (b) r = 250 nm Ni hole array and, and with (c) bare Si surface.

As can be seen in **Figure 5.11**, the empty buffer between the base of the dielectric cone and the Ni metal is a significant factor in transmission to the Si substrate. **Figure 5.11a** shows simulation results for a cone array without this gap, where the Ni film is flush against the base of the TiO_2 nanocone. This is due to the field profile of the waveguide modes / Bloch modes which extend outside the nanocone into the surrounding medium. If the metal hole array is too close to the TiO_2 nanostructure, absorption in the metal film will cause a large decrease in transmission for any wavelength with a field profile that overlaps with the metal film.

The transition from a flush Ni film in **Figure 5.11a**, to a Ni hole array with a radius of 250 nm shown in **Figure 5.11b**, and to the complete absence of a Ni film in **Figure 5.11c**, reveals the source of many of the pitch-dependent bands that appear in these simulations. The presence of the Ni film causes increased absorption at specific wavelengths, and these absorption peaks shift according to pitch size. It is likely that plasmonic modes on the Ni surface play a role in the absorption process.

These results will be further explored in **Section 5.8** , where they will be compared to metal island arrays with an optimized antireflection coating for use on planar III-V devices.

5.6 Metal Island Array with a Double-Layer Antireflection Coating

Many III-V multijunction photovoltaics utilize multi-layer antireflective coatings to reach optimal absorption of the AM1.5 solar spectrum. Materials used in these layers include MgF_2, ZnS, Ta_2O_5, SiO_2, Al_2O_3, and TiO_2, among others [132, 133]. In order to transfer these materials for use in photoelectrochemistry, these coatings must be considered not only for their optical and electronic properties, but also for corrosion resistance in acidic, alkaline, and near-neutral aqueous electrolytes.

Amorphous ALD-TiO_2 is stable in pH 14, and functions both as a hole-conducting protection layer as well as a single-layer antireflection coating with the correct index for use on Si and III-V photoanodes. Our focus was to create a double-layer antireflection coating (DL-ARC) using ALD-TiO_2. To increase absorption in the devices from **Chapters 3** and **4** , the partner material must be index matched for multijunction devices that use an ALD-TiO_2 protective coating.

While choosing antireflection materials, many considerations must be taken into account, including the film's mechanical and electrical properties, as well as deposition techniques. If a material is not conductive to anodic current it will presents an energy barrier between semiconductor and catalyst, and hole conduction must be facilitated by gaps in the film. While electron tunneling through thin layers can occur, these layers would be too thin to function as an antireflection coating. Preferably these films would be made from earth-abundant materials with scalable deposition processes that do not damage the III-V epilayers, and would serve as a second layer of protection against corrosion. Many metal oxide coatings have been considered for photoanode and photocathode protection in different pH ranges, including ZrO_2, HfO_2, SnO_2, In_2O_3, FeO_x, MnO_x, WO_3, ZnO, Ta_2O_5, NbO_x, Al_2O_3, MgO, SiO_2, and BiO_x [31].

SiO_2 was selected as a viable candidate material for the creation of a DL-ARC for having a compatible index of refraction (n = 1.46) and being widely used for semiconductor device applications. While SiO_2 is not thermodynamically stable in alkaline conditions, it does not corrode appreciably under neutral and acidic conditions [31, 134]. In fact, many Si photocathodes have been shown to form a passivating oxide layer of SiO_2 that stabilizes the semiconductor surface, presenting a barrier to electron transfer [31]. Advancements in the stability of Si electrodes in aqueous solutions also benefit any device that includes SiO_2 as an antireflection coating. Although amorphous TiO_2 acts as a hole-conducting protection layer, thick films of SiO_2 are a barrier to electron transfer, and would require patterning and

liftoff after deposition on the planar TiO_2 surface.

Ellipsometry was performed on thin films ALD-TiO_2 and sputtered SiO_2 deposited on Si to provide accurate data for the index or refraction and extinction coefficients. The TiO_2/SiO_2 DL-ARC was optimized for use on an ideal InGaP (1.84 eV)/InGaAsP (1.2 eV) III-V water-splitting design from **Chapter 2** . To perform 1D optical simulations of transmission to and reflection from these surfaces, we used the model from **Section 2.6**, with an initial surface index of n = 1.33 to represent the surrounding solution.

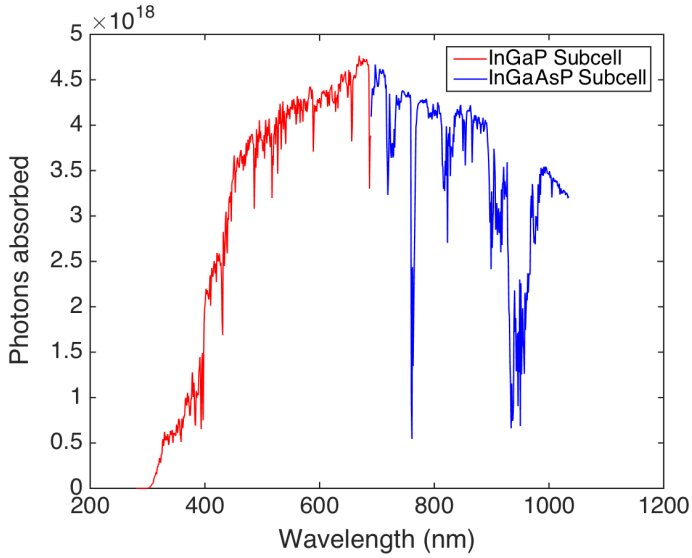

Figure 5.12: Detailed balance allocation of the AM1.5-weighted spectrum absorbed in the III-V device with optimal DL-ARC coating. All photons above the band edge of InGaP were allocated to the top junction.

The thickness of the DL-ARC film was designed using the short-circuit current density J_{SC} of the device as the figure of merit. A detailed balance model was used to calculate solar conversion efficiency using the AM1.5 spectrum. For each subcell in the stack, equation 5.2 was used to calculate short-circuit current density:

$$J_{sc} = q \int \frac{I(\lambda)}{E(\lambda)}(1 - R(\lambda))IQE(\lambda)d\lambda \tag{5.2}$$

where q is the elementary electric charge, $I(\lambda)$ is the irradiance as a function of wavelength, $E(\lambda)$ is the photon energy, $R(\lambda)$ the reflectance, and $IQE(\lambda)$ the internal quantum efficiency. All photons with energies above the band gap of InGaP were ascribed to the top junction of the device, as shown in **Figure 5.12**. Because the subcells are grown epitaxially in series, the lowest-performing subcell in the

multijunction device will be current-limiting. Thus, the lowest current density is used as a metric for device performance while varying DL-ARC coating thicknesses.

The short-circuit current density of the III-V device as a function of TiO_2/SiO_2 thicknesses is reported in **Figures 5.13**. The DL-ARC scheme shows significant improvement over the TiO_2 single-layer ARC, which can be seen as a function of TiO_2 thickness on the right hand side of the figure (zero SiO_2 thickness). The maximum current density is recorded as 18.9 mA cm^{-2} for TiO_2 (48 nm)/SiO_2 (84 nm). This corresponds to a increase in current density of 0.7 mA cm^{-2} or ~0.9% increase in η_{STH}.

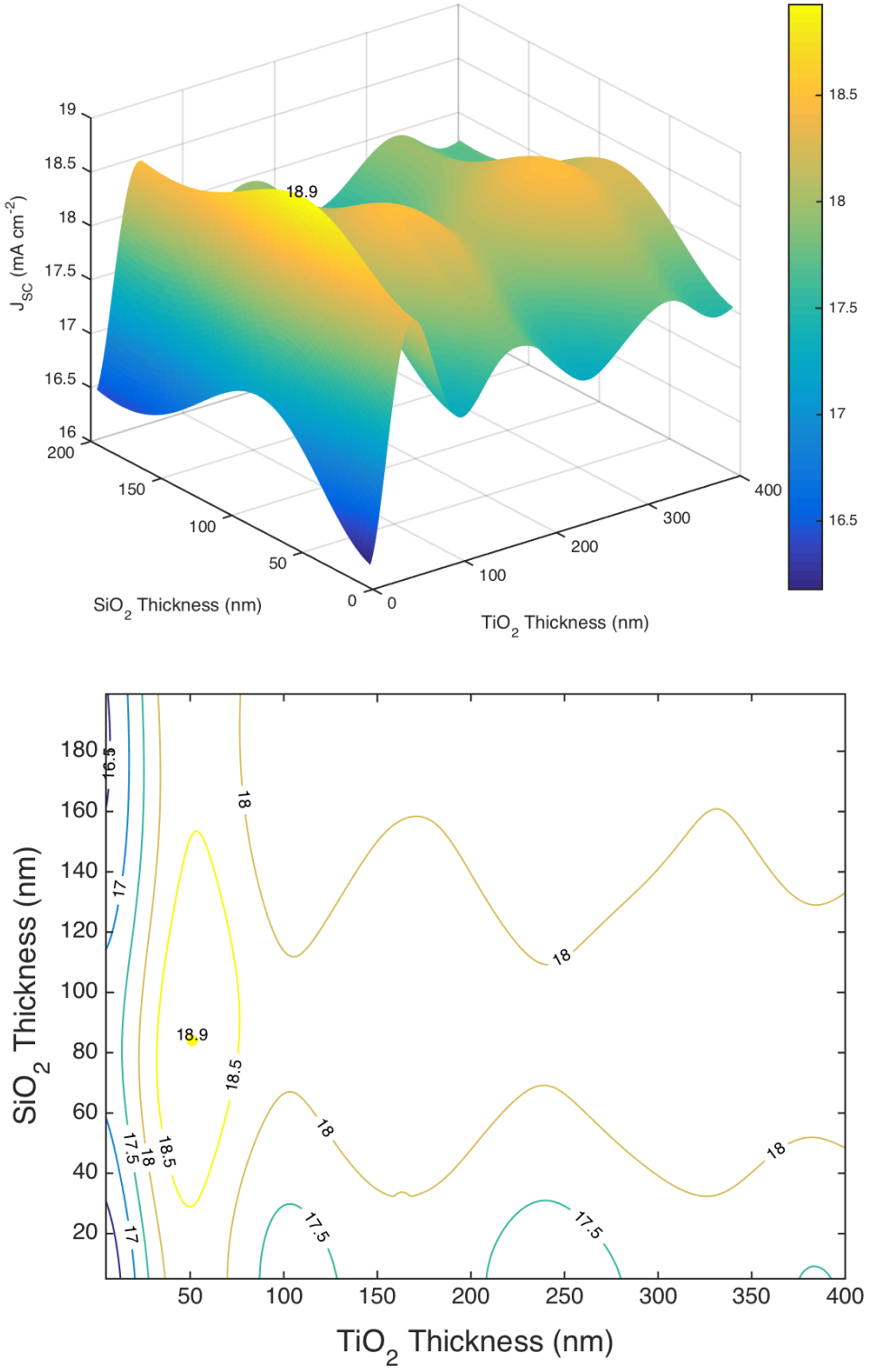

Figure 5.13: Current density versus SiO_2/TiO_2 DL-ARC thicknesses for the complete III-V PEC device. Represented in a surface plot (top) and contour plot (bottom).

5.7 Structured Metal Island Catalysts

The performance of the DL-ARC metal island design can also be improved by increasing catalyst loading. Large f_c can be achieved by raising the metal islands into higher aspect ratio structures. Recent work has shown effectively transparent contacts on the surfaces of optoelectronic devices, achieved by raising high-aspect-ratio triangular dielectric structures on top of metal busbars and selectively coating the inclined surfaces with reflective metal, which redirects incident light towards the semiconductor surface [135]. For use on PEC surfaces there is no need for raised structures to be continuous for the transport of electric charge; if the catalyst is reflective (e.g. Pt) the same effect can be achieved by using isolated metal cones coated in electrocatalyst.

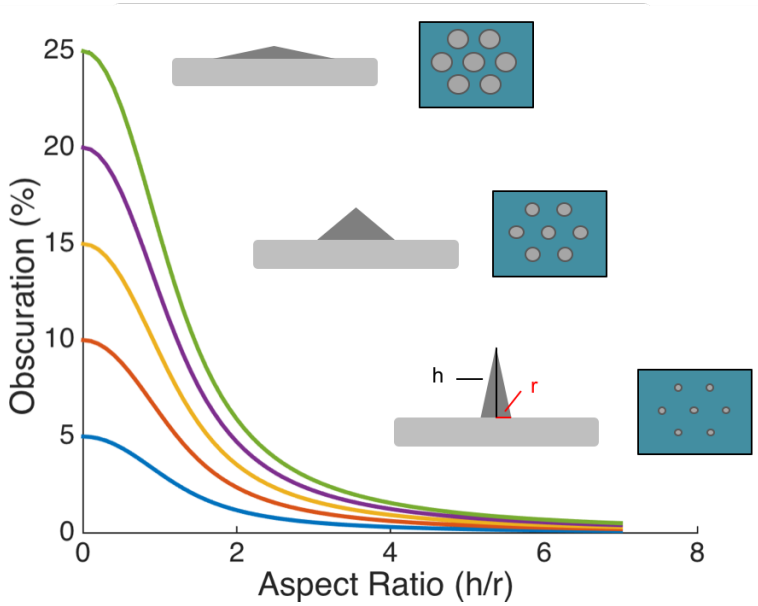

Figure 5.14: Obscuration of non-reflective conical structures with constant catalytic overpotential requirements. Starting with planar discs of 5-25% filling fraction, relatively modest aspect ratios will lead to a significant decrease in obscuration.

For these metal cones, there is no need to rely on the benefits from increased reflection towards the surface. As shown in **Figure 5.14**, for light of normal incidence, even the worst case scenario of a catalytic cone with 0% reflectance would benefit from a lower obscuration compared with metal islands of equivalent catalyst loading. The iso-overpotential plot in **Figure 5.14** starts with a hexagonal array of metal islands with the specified filling fraction (increasing at 5% intervals) and follows the geometric area shaded by cones with constant exterior surface area and increasing aspect ratio. A key takeaway from this simple calculation is that

low aspect ratios can yield significantly lower obscuration, without relying on gains from increased reflection to the surface.

Structured catalysts might also alleviate product buildup on the surface of the electrode. Until they are dislodged from the surface, bubbles of O_2(g) and H_2(g) adhere to reaction sites and limit the active surface area, negatively affecting electrochemical and optical properties of the electrode. It is likely that conical structures would facilitate bubble formation and removal.

5.8 Comparison of Optical Waveguides and DL-ARC Metal Island Arrays

In this chapter we have explored two light management schemes that would allow large f_c for non-transparent catalysts on planar PEC devices. In this section we compare the high-aspect-ratio dielectric waveguides to the DL-ARC metal island array.

Figure 5.15 shows the performance of the TiO_2 nanocone array, and the performance to the optimized DL-ARC with a metal island array, on planar GaAs in solution. **Figure 5.15a** shows the schematic of each structure, where both the metal hole and metal island arrays have a radius of 250 nm. Also in **Figure 5.15a**, the catalyst geometric filling fraction is plotted for both designs. Note that for a hexagonal island array, f_c decreases with increasing pitch, with 50% catalyst coverage occurring for both structures around a hexagonal lattice constant of 670 nm. Simulation results in **Figure 5.15b** cover transmission to the GaAs substrate as a function of pitch and wavelength for the nanocone array (left) and metal island scheme (right). For large f_c, there is a stark contrast in broadband transmission to the GaAs surface. The dotted line shows a pitch for both structures with f_c = 20%. The transmittance, reflectance, and absorptance for this catalyst loading, at 530 nm for the dielectric cones and 1060 nm for the metal island array, is plotted in **Figure 5.15c**. While transmission for the metal islands does not clear 80% transmittance, there is >90% transmittance for the TiO_2 waveguide array. Of course, the DL-ARC metal island scheme from **Figure 5.15** assumes a planar electrocatalyst disc, and is a lower limit for this design; the obscuration can be significantly reduced by structuring the electrocatalyst as seen in **Section 5.7** . With improvements from reflective catalysts, this scheme has the potential to surpass the waveguide design.

Using the transmittance for both strucutures, a detailed balance calculation was performed to determine the change in efficiency for a 1.84/1.2 eV bandgap III-V device using these light management schemes. For each pitch, the AM1.5

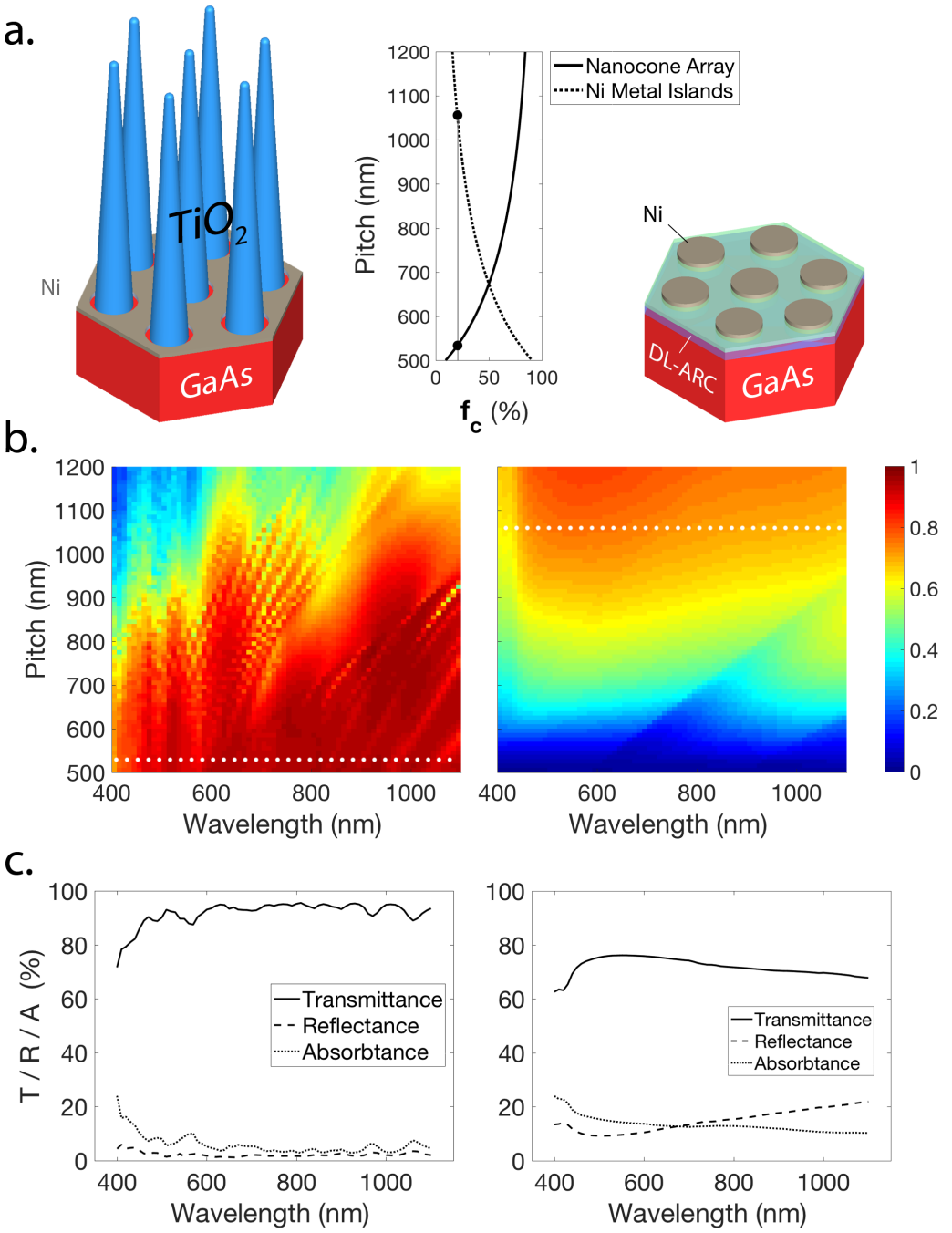

Figure 5.15: Performance of TiO_2 nanocone array on GaAs compared to a TiO_2(48 nm)/SiO_2(84 nm) DL-ARC with Ni metal island array. (a) Schematics and catalytic filling fraction of both structures. Cone base r = 200 nm, cone tip r = 50 nm, Ni hole and Ni island r = 250 nm, Ni film thickness 50 nm. (b) Transmittance as a function of hexagonal pitch and wavelength for nanocone array (left) and Ni island array (right). (c) Transmittance, reflectance, and absorptance for each array with f_c = 20%, at 530 nm / 1060 nm pitch (left/right) .

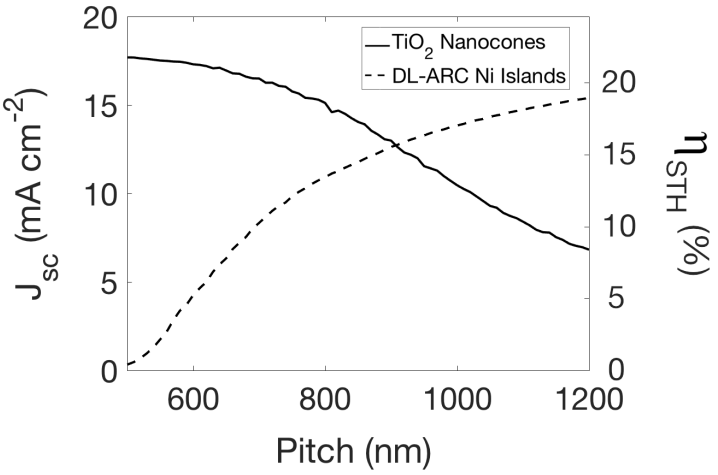

Figure 5.16: Short-circuit current density and solar-to-hydrogen efficiency of TiO_2 nanocone and DL-ARC Ni metal island arrays, using a detailed balance model with 1.84/1.2 eV bandgap combination.

solar spectrum was weighted by the transmittance vs. wavelength results, and the resulting spectrum was used to calculate the J_{sc} of the ideal tandem structure under 1-sun illumination. The device efficiency is plotted in **Figure 5.16**.

5.9 Strategies for TiO_2 Nanocone Fabrication

The ultrahigh optical transmission through thick metal films presented in the previous sections motivates further study of high-aspect-ratio dielectric waveguides. In this section we analyze promising methods for the fabrication of high-index TiO_2 nanocones.

A straight-forward approach that could easily yield high quality (and high-index) TiO_2 material is the deposition of planar films, either by reactive sputtering/e-vaporation of Ti metal in the presence of O_2(g), or by physical vapor deposition using a TiO_2 source. The resulting film must then be patterned and selectively etched away to expose the photoelectrode surface, leaving behind waveguide structures. Reasonably fast (>100 nm/min) fluorine-based dry etching recipes have been shown to etch TiO_2 films [136, 137]. These films could be patterned using a nanoscale photoresist mask, or by Langmuir-Blodgett assembly, which has previously been used to create Si nanocones uniformly on a 4-inch wafer [138]. However, these processes are likely to damage the underlying substrate due to low selectivity of TiO_2 over the Si/III-V epilayers [136]. There are many serious disadvantages that accompany etching of thick oxide films on optoelectronic surfaces, not least of which would be

the material costs of depositing ~3 μm of planar TiO_2 films only to etch away >90% of the material to form the desired nanostructures.

Alternatively, the patterning could be performed before deposition of these thick films, as it is possible to create tapered structures by means of PVD deposition into nanoscale patterns. Over the course of the deposition process, the edges of the sidewals get coated in material, encroaching on the deposition into the hole array and closing off the opening. If the sidewalls of the resist are large enough, this results in a tapered conical structure on the surface [139]. If successful, this process would offer limited control of the cone dimensions, and would require a liftoff step to remove the dielectric film. Preliminary results of e-beam evaporation of ~1 μm of TiO_2 on a Si surface patterned with e-beam lithography (~1 μm thick PMMA resist) are presented in **Figure 5.17**. Although the tapered TiO_2 structures were successfully grown on the surface, the liftoff process for these structures requires a thicker PMMA mask.

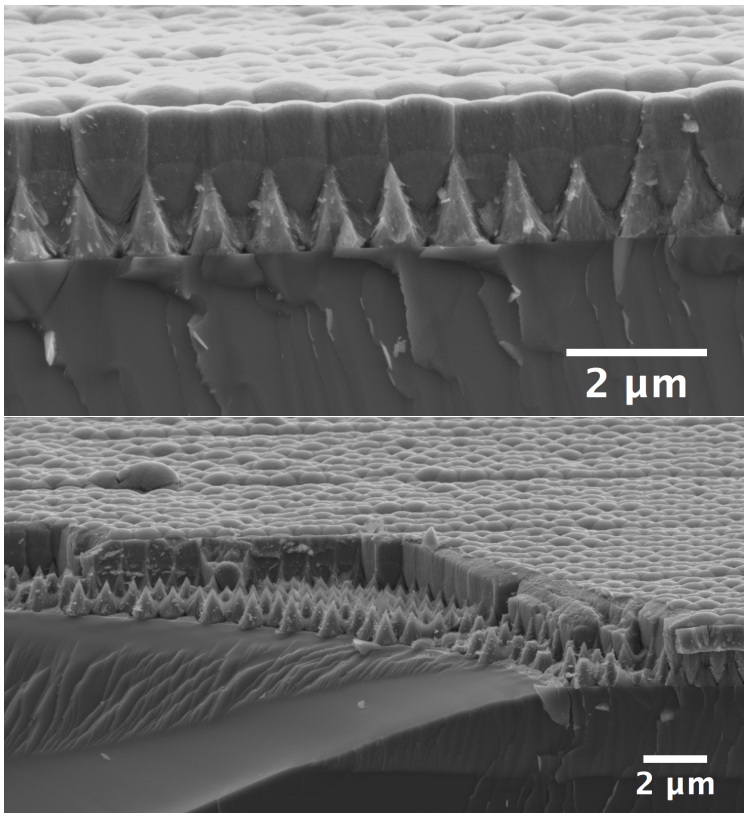

Figure 5.17: SEM images of TiO_2 nanocone fabrication using PVD on surfaces patterned with e-beam lithography.

A creative method for forming high-fidelity TiO_2 metasurfaces is atomic layer

deposition on a surface patterned with electron-beam lithography, which can yield high refractive index and very large aspect ratios [140]. The slow ~1200 nm ALD-TiO_2 growth is followed by RIE etching of the film to expose the resist layer. After removal of the resist, ~600 nm tall structures with relatively high refractive index (n > 2) [140]. While this could be useful for exploring optical properties of different TiO_2 nanostructures, this procedure would not be appropriate for industrial-scale adoption.

Nanoimprint lithography is a far more scalable process that can be used to produce high quality TiO_2 structures. Many sol-gel processes have been explored for the creation of dielectric hole arrays on Si and other semiconductors to increase absorption of optoelectronic interfaces, including nanoimprinted hole arrays of TiO_2 [137, 141, 142]. Nanopatterns made from photosensitive titanium di-n-butoxide bis(2-ethylhexanoate) have achieved refractive indices of anatase TiO_2 above n = 2.1 by using UV irradiation and high-temperature annealing treatments [142].

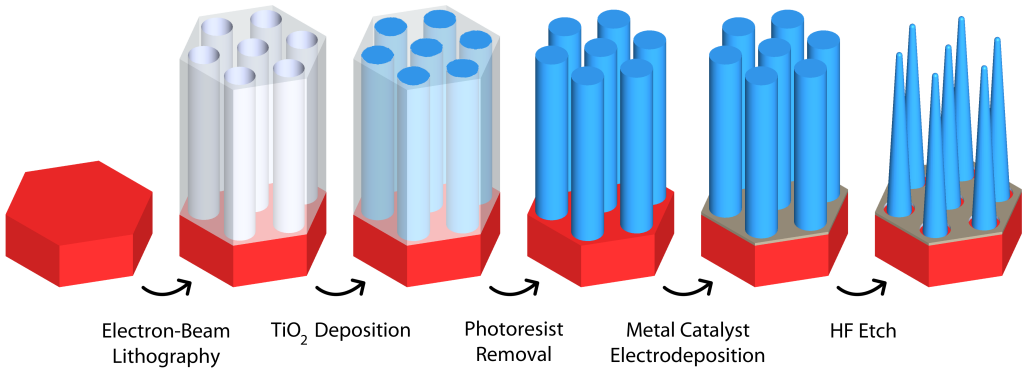

Figure 5.18: Suggested processing steps for TiO_2 dielectric waveguides on photoelectrode surface using electron-beam lithography.

Liquid-phase deposition of TiO_2 is an exciting approach to achieve nanostructures with high refractive index[131, 143]. In 2005, 2D and 3D photonic crystals of TiO_2 were made using supersaturated solutions of titanyl sulfate and hydrochloric acid at 60 °C [131]. The as-deposited refractive index of the structures reached n = 2.4, and was shown to exceed n = 2.6 after annealing at 700 °C. Because of the complexity of the 3D photonic crystals, the templates for these structures were made via deep x-ray lithography using a poly(methyl methacrylate) (PMMA) resist. However, e-beam lithography could easily be used in conjunction with the liquid-phase deposition process in order to create simpler cylindrical or conical structures on planar surfaces. **Figure 5.18** presents an overview of the cell processing steps for

the creation of TiO_2 nanocones using a liquid-phase growth. The final hydrofluoric (HF) acid etch should create the metal hole array buffer zone, as well as preferentially etch the wire tip due to increased exposure to solution. A tapered conical shape in the photoresist mask would encourage even sharper tips.

5.10 Summary and Outlook

Long-term stability of electrocatalytic films and a need for increased light absorption are two major challenges for PEC devices like those in **Chapter 3** and **Chapter 4**, and for CO_2R photocathodes. We have provided experimental evidence of broadband transmission through thick metal films using dielectric waveguides, and explored the optical properties of these structures using FDTD simulations. We have also designed an optimized ALD-TiO_2/SiO_2 DL-ARC that also functions as a protection layer. Finally, we have compared the capabilities of these structures to simultaneously increase absorption and to enable large f_c using opaque electrocatalysts. These light management strategies are not limited to III-V PEC devices; they can be modified for use on any planar photoelectrode surface.

Of particular interest is the high-index TiO_2 waveguide array. This versatile light management scheme shows potential benefits for a wide range of applications beyond solar fuels, including: solar PV, transparent antennas [144], electrodes for photosensors and light-emitting diodes (LEDs) [145], interconnects for fully transparent electronics [146], and current collectors for transparent batteries [147]. This provides motivation for future work on the fabrication of high-aspect-ratio dielectric nanocones.

Chapter 6

CONCLUSION

In this thesis, various approaches to highly efficient solar fuel production were explored. In order to achieve high efficiencies in a fully-integrated device, unstable III-V multijunction stacks were protected using hole-conducting TiO_2 and used to drive solar water splitting and CO_2 reduction reactions. An important aspect of this new photoelectrochemical protection scheme is the continued operation of an illuminated photoanode for water oxidation. Allowing the fuel-forming reactions to operate in the dark, this design alleviates constraints imposed by cathode-side illumination, enabling a variety of architectures that can yield stable long-term operation with increased efficiencies.

Three novel TiO_2-protected III-V photoelectrochemical devices were demonstrated with ~10 % efficiency for solar water splitting and CO_2 reduction to formate. A large-area fully-integrated solar water splitting prototype was also developed using an anion exchange membrane and earth-abundant electrocatalysts, and stable operation was demonstrated by collecting gas products under 1 sun illumination. The integration of these components into a device that demonstrated unassisted and intrinsically safe hydrogen evolution represents a significant step towards large-scale solar fuel production.

Additionally, the work in this thesis explored an opportunity to increase efficiencies by using two light management schemes designed to allow broadband transmission through an electrode surface with significantly large catalyst loading. Arrays of TiO_2 nanocone structures were shown to significantly outperform DL-ARC metal island arrays, resulting in > 85% broadband transmission with large geometric filling fractions of metal catalysts. Structured electrocatalysts would also significantly decrease obscuration and have the potential to facilitate product removal. Both schemes are widely applicable for use in many different electrolytes, and in conjunction with a variety of planar devices.

Future directions

- For solar water splitting, completion of the 1.8/1.2 eV bandgap combination could be experimentally shown using the epitaxial liftoff and wafer-bonding

procudure, and use of the ALD-TiO_2 protection scheme could yield higher efficiencies and similar stability compared to the water-splitting prototypes in this thesis.

- The bipolar membrane device demonstrations can be expanded to include existing material systems which are stable in many different electrolytes, including a pH 0/14 combination, as well as future CO_2 reduction environments.

- The work on stable DL-ARCs could be followed up with a search for new stable materials in alkaline and acidic conditions, and conduction through this material can be accomplished through photolithographic cell processing on TiO_2 surfaces. Also, fabrication of the conical reflective catalysts, when combined with an antireflective film, has the potential to outperform the waveguide design. The conical depositions are not required to be catalytically active, as electrocatalysts could be dropcast or electrodeposited on the metal surfaces.

- Fabrication of the TiO_2 nanocone arrays using one of the methods highlighted in **Chapter 5** would allow further experimental verification of the waveguide mode transmission through thick metal films. Successful demonstration of these waveguide arrays with high catalyst loading would provide many opportunities for increasing both efficiency and longevity of planar PEC devices. Protective films of thick metal catalysts that previously would have created unacceptable obscuration for photoelectrode surfaces could have the added benefit of providing a barrier to corrosion, and this method could be combined with the ALD-TiO_2 protection scheme, further increasing stability.

- Finally, dielectric nanocone arrays that allow transmission through thick metal films can be used in many fields beyond photoelectrochemistry. This light management scheme could have a large impact on photovoltaics, photosensors, LEDs, transparent batteries, photonic integrated circuits, and many other optoelectronic devices.

Solar fuel devices have come a long way in the past decade, but are still in the proof-of-concept stage. Further improvements are required to create systems that can be produced for commercial deployment, with a major goal being the development of stable materials for light absorption that can be combined with other cell components in a fully-integrated device for the production of solar fuel.

By increasing efficiency and stability, and decreasing manufacturing costs, these technologies have the potential to compensate for the intermittency of sunlight, providing a renewable source for fuel and offsetting carbon emissions.

Appendix A

METHODS

Ellipsometry

Complex refractive index (n, k) data for films of as-grown TiO_2 on Si were obtained using spectroscopic ellipsometry. The ellipsometric data were acquired using a J.A. Woolam V-VASE system. The non-absorbing (k 0) portion of the data was fit using a Cauchy model that assumed a TiO_2/SiO_2 bilayer structure on Si. The TiO_2 n, k values were extracted from a point-by-point fit, using fixed Cauchy and film-thickness parameters.

Finite Difference Time Domain (FDTD) Simulations

Lumerical FDTD, a commercial software, was used to perform 3D, full-field electromagnetic simulations of TiO_2 nanowire arrays. Arrays were constructed using a rectangular 3D simulation region, with periodic Bloch boundary conditions applied in the x and y directions and infinite boundary conditions, rendered as perfectly matched layers (PML), in the z direction. Parameter sweeps of the hexagonal arrays were illuminated with single-wavelength infinite plane wave sources at 10 nm intervals, with a long pulse time of 50 fs to simulate steady-state illuminated behavior. Transmittance, reflectance, and absorptance of the dielectric structure and Ni metal film was calculated using two transmission monitors, one directly above the nanostructure and one directly below on the surface of the substrate. The only exception was for transmittance of IP-Dip nanocones through ITO, where the transmission monitor was placed below the ITO film in the glass substrate.

Appendix B

MATLAB CODE FOR OPTICAL SIMULATIONS

The following code was written in collaboration with Alec Ho and Ke Sun.

Listing B.1: DLARCreflection.m

```
% DLARCreflection.m - reflection of multilayer
    structure
%
% Usage: refl = reflection(nk_tio2, nk_topl, nk_water,
    nk_gaas, t_tio2, t_topl, la)
%
% nk_tio2 = complex index of refraction of TiO2
% nk_topl = complex index of refraction of top layer
% nk_gaas = complex index of refraction of GaAs
% t_tio2_gradtop = top gradient tio2 thickness (nm)
% t_tio2_gradbot = bottom gradient tio2 thickness (nm)
% t_topl = top layer thickness (nm)
% la = wavelengths
%
% L = vector of optical lengths of layers, in units of
    lambda_0
%
% refl = reflection response at interface-1 into left
    medium evaluated at lambda

function refl = DLARCreflectionErik(nk_tio2_gradtop,
    nk_tio2_gradbot,...
      nk_topl, nk_water, nk_gaas1,nk_alinp1,nk_gainp1,...
      nk_alinp2,nk_gaas2,nk_algaas1,nk_gainp2,...
      nk_algaas2, t_tio2, t_topl, ...
      t_gaas1,t_alinp1,t_gainp1,t_alinp2,t_gaas2,...
      t_algaas1,t_gainp2,t_algaas2,la)
```

```
        la0 = 500;

        L_topl = nk_topl.*t_topl/la0;
        L_tio2_gradtop = nk_tio2_gradtop.*t_tio2/(2*la0
            );
        L_tio2_gradbot = nk_tio2_gradbot.*t_tio2/(2*la0
            );
        L_gaas1 = nk_gaas1.*t_gaas1/la0;
        L_alinp1 = nk_alinp1.*t_alinp1/la0;
        L_gainp1 = nk_gainp1.*t_gainp1/la0;
        L_alinp2 = nk_alinp2.*t_alinp2/la0;
        L_gaas2 = nk_gaas2.*t_gaas2/la0;
        L_algaas1 = nk_algaas1.*t_algaas1/la0;
        L_gainp2 = nk_gainp2.*t_gainp2/la0;
        L_algaas2 = nk_algaas2.*t_algaas2/la0;

        refl = abs(multidiel([nk_water,nk_topl,
            nk_tio2_gradtop,nk_tio2_gradbot,...
        nk_gaas1,nk_alinp1,nk_gainp1,nk_alinp2,nk_gaas2
            ,nk_algaas1,nk_gainp2,...
        nk_algaas2,nk_gaas1],[L_topl,L_tio2_gradtop,
            L_tio2_gradbot,L_gaas1,L_alinp1,...
        L_gainp1,L_alinp2,L_gaas2,L_algaas1,L_gainp2,
            L_algaas2],la/la0,0)).^2;

end
```

Listing B.2: DLARCShortCircuitCurrent.m

```
% DLARCShortCircuitCurrent.m - short circuit current of
    a multilayer structure
%
% Usage: [Jsc,Jtop,Jbot] = DLARCShortCircuitCurrent(
    top_photon_flux, ...
%     nk_tio2_gradtop_top, nk_tio2_gradbot_top,
```

```
    nk_topl_top, ...
%       nk_water_top, nk_gaas_top, top_wavelengths,
    bottom_photon_flux, ...
%       nk_tio2_gradtop_bottom, nk_tio2_gradbot_bottom,
    nk_topl_bottom, ...
%       nk_water_bottom, nk_gaas_bottom,
    bottom_wavelengths, t_tio2, t_topl)
%
% photon_flux = photon flux
% nk_tio2_gradtop = complex index of refraction of top
    gradient TiO2
% nk_tio2_gradbot = complex index of refraction of
    bottom gradient TiO2
% nk_topl = complex index of refraction of top layer
% nk_water = complex index of refraction of top layer
% nk_gaas = complex index of refraction of GaAs
% t_tio2 = tio2 thickness (nm)
% t_topl = top layer thickness (nm)
% wavelengths = wavelengths
%
% Jsc = short circuit current defined by the minimum of
     Jbot and Jtop
% (mA/cm^2)
% Jtop = current at top band edge (mA/cm^2)
% Jbot = current at bottom band edge (mA/cm^2)

function [Jsc,Jtop,Jbot] = DLARCShortCircuitCurrent(
    top_photon_flux, ...
      nk_tio2_gradtop_top, nk_tio2_gradbot_top,
         nk_topl_top, ...
      nk_water_top, nk_gaas_top, top_wavelengths,
         bottom_photon_flux, ...
      nk_tio2_gradtop_bottom, nk_tio2_gradbot_bottom,
         nk_topl_bottom, ...
      nk_water_bottom, nk_gaas_bottom, bottom_wavelengths
         , t_tio2, t_topl)
```

```
        [total_photons_top, ~] = DLARCPhotonsAbsorbed(
            top_photon_flux, ...
        nk_tio2_gradtop_top, nk_tio2_gradbot_top,
            nk_topl_top, ...
        nk_water_top, nk_gaas_top, t_tio2, t_topl,
            top_wavelengths);

        [total_photons_bottom, ~] =
            DLARCPhotonsAbsorbed(bottom_photon_flux, ...
        nk_tio2_gradtop_bottom, nk_tio2_gradbot_bottom,
             nk_topl_bottom, ...
        nk_water_bottom, nk_gaas_bottom, t_tio2, t_topl
            , bottom_wavelengths);

        Jtop = total_photons_top * 1.60217646e-19 / 10;
             %lm^2 to 1cm^2, A to mA
        Jbot = total_photons_bottom * 1.60217646e-19 /
            10; %lm^2 to 1cm^2, A to mA

        Jsc = min(Jtop, Jbot);

end
```

Listing B.3: DLARC.m

```
% Double Layer AR coating Optimal thickness calculator
    for III-V device

clc
close all

% Band gap wavelengths
lambda_top = 1240.8/1.8;
lambda_bottom = 1240.8/1.2;
```

```
% Thickness limits
tio2_tmin = 5;
tio2_tmax = 400;
topl_tmin = 5;
topl_tmax = 200;
jsc_min = 10;
jsc_max = 25;

% Name of Top Layer for plots and saving files
topfilename = '2016-10-11_sio2_on_TiO2_on_III-V_nk_data
    .txt';
topname = 'SiNx';
topnameString = 'SiN_{x}';
trialnum = '2';

% Load AM 1.5 Spectrum & photon flux
AM_data = importdata('AM15 Global Photon Flux.csv',',')
    ;
photon_flux = AM_data(:,2);
wavelengths = AM_data(:,1);

% Input Indices of Refraction & exctinction
    coefficients
water_data = importdata('water_nk.csv',',');
nalgaas = importdata('algaas_nk.txt');
nalinp = importdata('alinp_nk.txt');
ngainp = importdata('gainp_nk.txt');
gaas_data = importdata('gaas_nk.csv',',');
tio2_data = importdata('2015-08-26
    _TiO2_nk_gradient_on_Si.txt'); % Accounts for TiO2
    index gradient


n_water = interp1(water_data(:,1), water_data(:,2),
    wavelengths,'linear','extrap');
k_water = interp1(water_data(:,1), water_data(:,3),
```

```
    wavelengths,'linear','extrap');
n_gaas = interp1(gaas_data(:,1), gaas_data(:,2),
    wavelengths,'linear','extrap');
k_gaas = interp1(gaas_data(:,1), gaas_data(:,3),
    wavelengths,'linear','extrap');
n_tio2_gradtop = interp1(tio2_data(:,1), tio2_data(:,2)
    ,wavelengths,'linear','extrap');
k_tio2_gradtop = interp1(tio2_data(:,1),tio2_data(:,3),
    wavelengths,'linear','extrap');
n_tio2_gradbot = interp1(tio2_data(:,1), tio2_data(:,4)
    ,wavelengths,'linear','extrap');
k_tio2_gradbot = interp1(tio2_data(:,1),tio2_data(:,5),
    wavelengths,'linear','extrap');
n_algaas = interp1(nalgaas(:,1),nalgaas(:,2),
    wavelengths,'linear','extrap');
k_algaas = interp1(nalgaas(:,1),nalgaas(:,3),
    wavelengths,'linear','extrap');
n_alinp = interp1(nalinp(:,1),nalinp(:,2),wavelengths,'
    linear','extrap');
k_alinp = interp1(nalinp(:,1),nalinp(:,3),wavelengths,'
    linear','extrap');
n_gainp = interp1(ngainp(:,1),ngainp(:,2),wavelengths,'
    linear','extrap');
k_gainp = interp1(ngainp(:,1),ngainp(:,3),wavelengths,'
    linear','extrap');

% Allows for data with and without headers as input
[top_layer,delim,headers] = importdata(topfilename);
if headers == 0
    n_topl = interp1(top_layer(:,1), top_layer(:,2),
        wavelengths,'linear','extrap');
    k_topl = interp1(top_layer(:,1),top_layer(:,3),
        wavelengths,'linear','extrap');
else
    n_topl = interp1(top_layer.data(:,1), top_layer.
        data(:,2),wavelengths,'linear','extrap');
```

```
    k_topl = interp1(top_layer.data(:,1),top_layer.data
       (:,3),wavelengths,'linear','extrap');
end

% Separate variables by band gap
top_index = find(wavelengths <= lambda_top);
bottom_index = find(wavelengths >= lambda_top &
   wavelengths <= lambda_bottom);
top_wavelengths = wavelengths(top_index);
bottom_wavelengths = wavelengths(bottom_index);
top_photon_flux = photon_flux(top_index);
bottom_photon_flux = photon_flux(bottom_index);
top_tio2__gradtop_n = n_tio2_gradtop(top_index);
bottom_tio2__gradtop_n = n_tio2_gradtop(bottom_index);
top_tio2__gradbot_n = n_tio2_gradbot(top_index);
bottom_tio2__gradbot_n = n_tio2_gradbot(bottom_index);
top_topl_n = n_topl(top_index);
bottom_topl_n = n_topl(bottom_index);
top_gaas_n = n_gaas(top_index);
bottom_gaas_n = n_gaas(bottom_index);
top_water_n = n_water(top_index);
bottom_water_n = n_water(bottom_index);
top_tio2_gradtop_k = k_tio2_gradtop(top_index);
bottom_tio2_gradtop_k = k_tio2_gradtop(bottom_index);
top_tio2_gradbot_k = k_tio2_gradbot(top_index);
bottom_tio2_gradbot_k = k_tio2_gradbot(bottom_index);
top_topl_k = k_topl(top_index);
bottom_topl_k = k_topl(bottom_index);
top_gaas_k = k_gaas(top_index);
bottom_gaas_k = k_gaas(bottom_index);
top_water_k = k_water(top_index);
bottom_water_k = k_water(bottom_index);
top_algaas_n = n_algaas(top_index);
top_algaas_k = k_algaas(top_index);
top_alinp_n = n_alinp(top_index);
top_alinp_k = k_alinp(top_index);
```

```
top_gainp_n = n_gainp(top_index);
top_gainp_k = k_gainp(top_index);
bot_algaas_n = n_algaas(bottom_index);
bot_algaas_k = k_algaas(bottom_index);
bot_alinp_n = n_alinp(bottom_index);
bot_alinp_k = k_alinp(bottom_index);
bot_gainp_n = n_gainp(bottom_index);
bot_gainp_k = k_gainp(bottom_index);

% Reconstruct complex refractive index
j = sqrt(-1);
nk_water_top = top_water_n - j*top_water_k;
nk_topl_top = top_topl_n - j*top_topl_k;
nk_tio2_gradtop_top = top_tio2__gradtop_n - j*
   top_tio2_gradtop_k;
nk_tio2_gradbot_top = top_tio2__gradbot_n - j*
   top_tio2_gradbot_k;
nk_gaas_top = top_gaas_n - j*top_gaas_k;
nk_algaas_top = top_algaas_n - j*top_algaas_k;
nk_alinp_top = top_alinp_n - j*top_alinp_k;
nk_gainp_top = top_gainp_n - j*top_gainp_k;

nk_water_bottom = bottom_water_n - j*bottom_water_k;
nk_topl_bottom = bottom_topl_n - j*bottom_topl_k;
nk_tio2_gradtop_bottom = bottom_tio2__gradtop_n - j*
   bottom_tio2_gradtop_k;
nk_tio2_gradbot_bottom = bottom_tio2__gradbot_n - j*
   bottom_tio2_gradbot_k;
nk_gaas_bottom = bottom_gaas_n - j*bottom_gaas_k;
nk_algaas_bottom = bot_algaas_n - j*bot_algaas_k;
nk_alinp_bottom = bot_alinp_n - j*bot_alinp_k;
nk_gainp_bottom = bot_gainp_n - j*bot_gainp_k;

% Set substrate thicknesses
t_gaas1 = 7;
t_alinp1 = 30;
```

```
t_gainp1 = 270;
t_alinp2 = 20;
t_gaas2 = 20;
t_algaas1 = 20;
t_gainp2 = 20;
t_algaas2 = 250;

% Find optimal thicknesses
OptimizedJsc = 0;
opt_tio2 = 0;
opt_topl = 0;
TiO2Thicknesses = zeros(1,(tio2_tmax-tio2_tmin)*(
   topl_tmax-topl_tmin));
TopLayerThicknesses = zeros(1,(tio2_tmax-tio2_tmin)*(
   topl_tmax-topl_tmin));
JscOutputs = zeros(1,(tio2_tmax-tio2_tmin)*(topl_tmax-
   topl_tmin));
JtopOutputs = zeros(1,(tio2_tmax-tio2_tmin)*(topl_tmax-
   topl_tmin));
JbotOutputs = zeros(1,(tio2_tmax-tio2_tmin)*(topl_tmax-
   topl_tmin));

% Write Jsc output as an output for an array of
   thicknesses
for i = tio2_tmin:tio2_tmax;
    for j = topl_tmin:topl_tmax;
        TiO2Thicknesses((i - tio2_tmin)*(topl_tmax-
           topl_tmin) + j - topl_tmin + 1) = i;
        TopLayerThicknesses((i - tio2_tmin)*(topl_tmax-
           topl_tmin) + j - topl_tmin + 1) = j;
        [Jtot, Jt, Jb] = DLARCShortCircuitCurrent(
           top_photon_flux,...
            nk_tio2_gradtop_top, nk_tio2_gradbot_top,
               nk_topl_top, ...
            nk_water_top, nk_gaas_top,nk_alinp_top,
               nk_gainp_top,...
```

```
            nk_alinp_top,nk_gaas_top,nk_algaas_top,
               nk_gainp_top,...
            nk_algaas_top, top_wavelengths,...
            bottom_photon_flux, nk_tio2_gradtop_bottom
               ,...
            nk_tio2_gradbot_bottom, nk_topl_bottom,
               nk_water_bottom,...
            nk_gaas_bottom,nk_alinp_bottom,
               nk_gainp_bottom,...
            nk_alinp_bottom,nk_gaas_bottom,
               nk_algaas_bottom,...
            nk_gainp_bottom,nk_algaas_bottom,
               bottom_wavelengths,...
            t_gaas1,t_alinp1,t_gainp1,t_alinp2,t_gaas2,
               t_algaas1,...
            t_gainp2,t_algaas2, i, j);
        JscOutputs((i - tio2_tmin)*(topl_tmax-topl_tmin
           ) + j - topl_tmin + 1) = Jtot;
        JtopOutputs((i - tio2_tmin)*(topl_tmax-
           topl_tmin) + j - topl_tmin + 1) = Jt;
        JbotOutputs((i - tio2_tmin)*(topl_tmax-
           topl_tmin) + j - topl_tmin + 1) = Jb;
        % Find overall optimized Jsc
        if OptimizedJsc < Jtot;
            OptimizedJsc = Jtot;
            OptTiO2Thickness = i;
            OptTopLayerThickness = j;
        end
    end
end

% Get rid of random extra data point
JscOutputs(end) = [];
TiO2Thicknesses(end) = [];
TopLayerThicknesses(end) = [];
JtopOutputs(end) = [];
```

```
JbotOutputs(end) = [];

% Reformat for saving with column headers
JscOutputs = JscOutputs';
TiO2Thicknesses = TiO2Thicknesses';
TopLayerThicknesses = TopLayerThicknesses';
JtopOutputs = JtopOutputs';
JbotOutputs = JbotOutputs';

table_t_J = table(TiO2Thicknesses, TopLayerThicknesses,
    ...
    JscOutputs, JtopOutputs, JbotOutputs);
writetable(table_t_J, ['DLARC Jsc versus TiO2 and ',
   topname,' Thickness.txt']);

% Reshape data to be used in surf and contour plots
X = reshape(TiO2Thicknesses,topl_tmax-topl_tmin,
   tio2_tmax-tio2_tmin+1);
Y = reshape(TopLayerThicknesses,topl_tmax-topl_tmin,
   tio2_tmax-tio2_tmin+1);
Z = reshape(JscOutputs,topl_tmax-topl_tmin,tio2_tmax-
   tio2_tmin+1);
Jscstr = num2str(OptimizedJsc,3);

% Surface plot
surf(X,Y,Z,'EdgeColor','none');
text(OptTiO2Thickness,OptTopLayerThickness,OptimizedJsc
   ,Jscstr,'horizontalAlignment',...
    'center', 'verticalAlignment', 'base');
xlabel('TiO_{2} Thickness (nm) ');
ylabel([topnameString, ' Thickness (nm) ']);
zlabel('J_{SC} (mA cm^{-2}) ');
% title(['J_{sc} versus TiO_{2} and ', topname, '
   Thickness ']);
colorbar;
colormap('parula');
```

```
saveas(gcf,['Surface Plot Jsc Versus TiO2 and ',
   topname, ...
    ' Thickness Trial ', trialnum,'.png']);
hold off

% Surface plot - save to file
fid=fopen(['Surface Plot Jsc Versus TiO2 and ', topname
   , ...
    ' Thickness Trial ', trialnum,'.txt'],'w');
fprintf(fid, '%d %d %d \r\n', [X Y Z]');
fclose(fid);

% Contour Plot
v = [16 16.5 17 17.5 18 18.5 19];
[c,h] = contour(X,Y,Z,v,'LabelSpacing',350);
clabel(c,h,v);
colormap('parula');
hold on
s = scatter(OptTiO2Thickness,OptTopLayerThickness);
s.MarkerEdgeColor = 'y';
s.MarkerFaceColor = 'y';
text(OptTiO2Thickness,OptTopLayerThickness,Jscstr,'
   horizontalAlignment',...
    'center', 'verticalAlignment', 'base');
xlabel('TiO_{2} Thickness (nm)');
ylabel([topnameString, ' Thickness (nm)']);
% title(['J_{sc} Versus TiO_{2} and ', topnameString, '
    Thickness']);
saveas(gcf,['Contour Plot Jsc Versus TiO2 and ',
   topname, ...
    ' Thickness Device Trial ', trialnum,'.png']);
hold off

% Save figures of the reflection and photons absorbed
t_tio2_vec1 = (1:size(top_wavelengths,1))';
t_tio2_vec1(1:size(top_wavelengths,1)) =
```

```
    OptTiO2Thickness;
t_topl_vec1 = (1:size(top_wavelengths,1))';
t_topl_vec1(1:size(top_wavelengths,1)) =
    OptTopLayerThickness;

t_tio2_vec2 = (1:size(bottom_wavelengths,1))';
t_tio2_vec2(1:size(bottom_wavelengths,1)) =
    OptTiO2Thickness;
t_topl_vec2 = (1:size(bottom_wavelengths,1))';
t_topl_vec2(1:size(bottom_wavelengths,1)) =
    OptTopLayerThickness;

t_gaas_vec11 = (1:size(top_wavelengths,1))';
t_gaas_vec11(1:size(top_wavelengths,1)) = t_gaas1;
t_alinp_vec11 = (1:size(top_wavelengths,1))';
t_alinp_vec11(1:size(top_wavelengths,1)) = t_alinp1;
t_gainp_vec11 = (1:size(top_wavelengths,1))';
t_gainp_vec11(1:size(top_wavelengths,1)) = t_gainp1;
t_alinp_vec21 = (1:size(top_wavelengths,1))';
t_alinp_vec21(1:size(top_wavelengths,1)) = t_alinp2;
t_gaas_vec21 = (1:size(top_wavelengths,1))';
t_gaas_vec21(1:size(top_wavelengths,1)) = t_gaas2;
t_algaas_vec11 = (1:size(top_wavelengths,1))';
t_algaas_vec11(1:size(top_wavelengths,1)) = t_algaas1;
t_gainp_vec21 = (1:size(top_wavelengths,1))';
t_gainp_vec21(1:size(top_wavelengths,1)) = t_gainp2;
t_algaas_vec21 = (1:size(top_wavelengths,1))';
t_algaas_vec21(1:size(top_wavelengths,1)) = t_algaas2;

t_gaas_vec12 = (1:size(bottom_wavelengths,1))';
t_gaas_vec12(1:size(bottom_wavelengths,1)) = t_gaas1;
t_alinp_vec12 = (1:size(bottom_wavelengths,1))';
t_alinp_vec12(1:size(bottom_wavelengths,1)) = t_alinp1;
t_gainp_vec12 = (1:size(bottom_wavelengths,1))';
t_gainp_vec12(1:size(bottom_wavelengths,1)) = t_gainp1;
t_alinp_vec22 = (1:size(bottom_wavelengths,1))';
```

```
t_alinp_vec22(1:size(bottom_wavelengths,1)) = t_alinp2;
t_gaas_vec22 = (1:size(bottom_wavelengths,1))';
t_gaas_vec22(1:size(bottom_wavelengths,1)) = t_gaas2;
t_algaas_vec12 = (1:size(bottom_wavelengths,1))';
t_algaas_vec12(1:size(bottom_wavelengths,1)) =
   t_algaas1;
t_gainp_vec22 = (1:size(bottom_wavelengths,1))';
t_gainp_vec22(1:size(bottom_wavelengths,1)) = t_gainp2;
t_algaas_vec22 = (1:size(bottom_wavelengths,1))';
t_algaas_vec22(1:size(bottom_wavelengths,1)) =
   t_algaas2;

refl1 = arrayfun(@DLARCreflection,nk_tio2_gradtop_top
   ,...
    nk_tio2_gradbot_top, nk_topl_top, nk_water_top, ...
    nk_gaas_top,nk_alinp_top,nk_gainp_top,nk_alinp_top
       ,...
    nk_gaas_top,nk_algaas_top,nk_gainp_top,
       nk_algaas_top,...
    t_tio2_vec1, t_topl_vec1, t_gaas_vec11,
       t_alinp_vec11,t_gainp_vec11,...
    t_alinp_vec21,t_gaas_vec21,t_algaas_vec11,
       t_gainp_vec21,t_algaas_vec21,...
    top_wavelengths);
plot(top_wavelengths, refl1, '-b')
hold on
refl2 = arrayfun(@DLARCreflection,
   nk_tio2_gradtop_bottom,...
    nk_tio2_gradbot_bottom, nk_topl_bottom,
       nk_water_bottom, ...
    nk_gaas_bottom,nk_alinp_bottom,nk_gainp_bottom,
       nk_alinp_bottom,...
    nk_gaas_bottom,nk_algaas_bottom,nk_gainp_bottom,
       nk_algaas_bottom,...
    t_tio2_vec2, t_topl_vec2, t_gaas_vec12,
       t_alinp_vec12,t_gainp_vec12,...
```

```
    t_alinp_vec22,t_gaas_vec22,t_algaas_vec12,
       t_gainp_vec22,t_algaas_vec22,...
    bottom_wavelengths);
plot(bottom_wavelengths, refl2, '-b')

xlabel('wavelength (nm)')
ylabel('Reflectance')
title(['Reflectance of TiO_{2} /',topnameString,'
   DLARC'])
saveas(gcf,['Reflectance of TiO2 ',num2str(
   OptTiO2Thickness),'nm and ',...
    topname,' ', num2str(OptTopLayerThickness),'nm
       Device Trial ', trialnum,'.png']);

% Surface plot - save to file
fid=fopen(['Reflectance of TiO2 ',num2str(
   OptTiO2Thickness),'nm and ',...
    topname,' ', num2str(OptTopLayerThickness),'nm
       Device Trial ', trialnum,'.txt'],'w');
fprintf(fid, '%d %d \r\n', [top_wavelengths refl1]');
fprintf(fid, '%d %d \r\n', [bottom_wavelengths refl2]')
   ;
fclose(fid);

hold off

[TotPhot1, PhotAbs1] = DLARCPhotonsAbsorbed(
   top_photon_flux, ...
    nk_tio2_gradtop_top,nk_tio2_gradbot_top,
       nk_topl_top, ...
    nk_water_top, nk_gaas_top,nk_alinp_top,nk_gainp_top
       ,nk_alinp_top,...
    nk_gaas_top,nk_algaas_top,nk_gainp_top,
       nk_algaas_top, OptTiO2Thickness, ...
    OptTopLayerThickness,t_gaas1,t_alinp1,t_gainp1,
       t_alinp2,t_gaas2,t_algaas1,...
```

```
    t_gainp2,t_algaas2, top_wavelengths);
[TotPhot2, PhotAbs2] = DLARCPhotonsAbsorbed(
   bottom_photon_flux, ...
    nk_tio2_gradtop_bottom, nk_tio2_gradbot_bottom,
       nk_topl_bottom, ...
    nk_water_bottom, nk_gaas_bottom,nk_alinp_bottom,
       nk_gainp_bottom,...
    nk_alinp_bottom,nk_gaas_bottom,nk_algaas_bottom,
       nk_gainp_bottom,...
    nk_algaas_bottom, OptTiO2Thickness,
       OptTopLayerThickness,t_gaas1,...
    t_alinp1,t_gainp1,t_alinp2,t_gaas2,t_algaas1,
       t_gainp2,t_algaas2,...
    bottom_wavelengths);

plot(top_wavelengths,PhotAbs1,'-r',bottom_wavelengths,
   PhotAbs2,'-b')
xlabel('wavelength (nm)')
ylabel('photons absorbed')
% title('Photons Absorbed by Top and Bottom Band Edge')
legend('InGaP Subcell',...
    'GaAs Subcell', 'Location', 'south')
saveas(gcf,['Photons Absorbed TiO2 ',num2str(
   OptTiO2Thickness),'nm and ', ...
    topname,' ',num2str(OptTopLayerThickness),'nm
       Device Trial ', trialnum,'.png']);

display(OptTiO2Thickness)
display(OptTopLayerThickness)
display(OptimizedJsc)
```

BIBLIOGRAPHY

1. McKone, J. R., Lewis, N. S. & Gray, H. B. Will Solar-Driven Water-Splitting Devices See the Light of Day? *Chemistry of Materials* **26,** 407–414 (2014).
2. Xiang, C. X., Weber, A. Z., Ardo, S., Berger, A., Chen, Y. K., Coridan, R., Fountaine, K. T., Haussener, S., Hu, S., Liu, R., Lewis, N. S., Modestino, M. A., Shaner, M. M., Singh, M. R., Stevens, J. C., Sun, K. & Walczak, K. Modeling, Simulation, and Implementation of Solar-Driven Water-Splitting Devices. *Angewandte Chemie-International Edition* **55,** 12974–12988 (2016).
3. Jacobsson, T. J., Fjallstrom, V., Edoff, M. & Edvinsson, T. Sustainable solar hydrogen production: from photoelectrochemical cells to PV-electrolyzers and back again. *Energy & Environmental Science* **7,** 2056–2070 (2014).
4. Lewis, N. S. Research opportunities to advance solar energy utilization. *Science* **351.** doi:ARTNaad511710.1126/science.aad5117 (2016).
5. Marshall, A. T., Sunde, S., Tsypkin, A. & Tunold, R. Performance of a PEM water electrolysis cell using $Ir_xRu_yTa_zO_2$ electrocatalysts for the oxygen evolution electrode. *International Journal of Hydrogen Energy* **32,** 2320–2324 (2007).
6. Barbir, F. PEM electrolysis for production of hydrogen from renewable energy sources. *Solar Energy* **78,** 661–669 (2005).
7. Ivy, J. *Summary of Electrolytic Hydrogen Production: Milestone Completion Report* Report (NREL, 2004).
8. Newman, J., Hoertz, P. G., Bonino, C. A. & Trainham, J. A. Review: An Economic Perspective on Liquid Solar Fuels. *Journal of the Electrochemical Society* **159,** A1722–A1729 (2012).
9. NREL. *Research Cell Efficiency Records* Report (2016).
10. Jacobsson, T. J., Fjallstrom, V., Sahlberg, M., Edoff, M. & Edvinsson, T. A monolithic device for solar water splitting based on series interconnected thin film absorbers reaching over 10% solar-to-hydrogen efficiency. *Energy & Environmental Science* **6,** 3676–3683 (2013).
11. Cox, C. R., Lee, J. Z., Nocera, D. G. & Buonassisi, T. Ten-percent solar-to-fuel conversion with nonprecious materials. *Proceedings of the National Academy of Sciences of the United States of America* **111,** 14057–14061 (2014).
12. Luo, J. S., Im, J. H., Mayer, M. T., Schreier, M., Nazeeruddin, M. K., Park, N. G., Tilley, S. D., Fan, H. J. & Gratzel, M. Water photolysis at 12.3% efficiency via perovskite photovoltaics and Earth-abundant catalysts. *Science* **345,** 1593–1596 (2014).

13. Licht, S., Wang, B., Mukerji, S., Soga, T., Umeno, M. & Tributsch, H. Efficient Solar Water Splitting, Exemplified by RuO2-Catalyzed AlGaAs/Si Photoelectrolysis. *The Journal of Physical Chemistry B* **104,** 8920–8924 (2000).

14. Fujii, K., Nakamura, S., Sugiyama, M., Watanabe, K., Bagheri, B. & Nakano, Y. Characteristics of hydrogen generation from water splitting by polymer electrolyte electrochemical cell directly connected with concentrated photovoltaic cell. *International Journal of Hydrogen Energy* **38,** 14424–14432 (2013).

15. Peharz, G., Dimroth, F. & Wittstadt, U. Solar hydrogen production by water splitting with a conversion efficiency of 18%. *International Journal of Hydrogen Energy* **32,** 3248–3252 (2007).

16. Sapru, K., Stetson, N. T., Ovshinsky, S. R., Yang, J., Fritz, G., Fairlie, M. & Stuart, A. T. B. Development of a small scale hydrogen production-storage system for hydrogen applications. *Iecec-97 - Proceedings of the Thirty-Second Intersociety Energy Conversion Engineering Conference, Vols 1-4,* 1947–1952 (1997).

17. Arriaga, L. G., Martinez, W., Cano, U. & Blud, H. Direct coupling of a solar-hydrogen system in Mexico. *International Journal of Hydrogen Energy* **32,** 2247–2252 (2007).

18. Han, L. H., Abdi, F. F., van de Krol, R., Liu, R., Huang, Z. Q., Lewerenz, H. J., Dam, B., Zeman, M. & Smets, A. H. M. Efficient Water-Splitting Device Based on a Bismuth Vanadate Photoanode and Thin-Film Silicon Solar Cells. *Chemsuschem* **7,** 2832–2838 (2014).

19. Lipman, T. *An Overview of Hydrogen Production and Storage Systems with Renewable Hydrogen Case Studies* Report (DOE, 2011).

20. James, B. D., Baum, G. N., Perez, J. & Baum, K. N. *Technoeconomic analysis of photoelectrochemical (PEC) hydrogen production* Report (DOE, 2009).

21. Ager III, J. W., Shaner, M., Walczak, K., Sharp, I. D. & Ardo, S. Experimental Demonstrations of Spontaneous, Solar-Driven Photoelectrochemical Water Splitting. *Energy & Environmental Science* (2015).

22. Haussener, S., Hu, S., Xiang, C. X., Weber, A. Z. & Lewis, N. S. Simulations of the irradiation and temperature dependence of the efficiency of tandem photoelectrochemical water-splitting systems. *Energy & Environmental Science* **6,** 3605–3618 (2013).

23. Haussener, S., Xiang, C. X., Spurgeon, J. M., Ardo, S., Lewis, N. S. & Weber, A. Z. Modeling, simulation, and design criteria for photoelectrochemical water-splitting systems. *Energy & Environmental Science* **5,** 9922–9935 (2012).

24. Doscher, H., Geisz, J. F., Deutsch, T. G. & Turner, J. A. Sunlight absorption in water - efficiency and design implications for photoelectrochemical devices. *Energy & Environmental Science* **7,** 2951–2956 (2014).

25. Seitz, L. C., Chen, Z. B., Forman, A. J., Pinaud, B. A., Benck, J. D. & Jaramillo, T. F. Modeling Practical Performance Limits of Photoelectrochemical Water Splitting Based on the Current State of Materials Research. *ChemSusChem* **7,** 1372–1385 (2014).

26. Smotkin, E. S., Cerveramarch, S., Bard, A. J., Campion, A., Fox, M. A., Mallouk, T. & Webber, S. E. Bipolar Cdse/Cos Semiconductor Photoelectrode Arrays for Unassisted Photolytic Water Splitting. *Journal of Physical Chemistry* **91,** 6–8 (1987).

27. Cerveramarch, S., Smotkin, E. S., Bard, A. J., Campion, A., Fox, M. A., Mallouk, T., Webber, S. E. & White, J. M. Modeling of Bipolar Semiconductor Photoelectrode Arrays for Electrolytic Processes. *Journal of the Electrochemical Society* **135,** 567–573 (1988).

28. Deng, X. & Xu, L. *Integrated photoelectrochemical cell and system having a liquid electrolyte* Patent. 2010.

29. Wrighton, M. S., Wolczanski, P. T. & Ellis, A. B. Photoelectrolysis of Water by Irradiation of Platinized n-Type Semiconducting Metal Oxides. *Journal of Solid State Chemistry* **22,** 17–29 (1977).

30. Nozik, A. J. & Memming, R. Physical chemistry of semiconductor-liquid interfaces. *Journal of Physical Chemistry* **100,** 13061–13078 (1996).

31. Hu, S., Lewis, N. S., Ager, J. W., Yang, J. H., McKone, J. R. & Strandwitz, N. C. Thin-Film Materials for the Protection of Semiconducting Photoelectrodes in Solar-Fuel Generators. *Journal of Physical Chemistry C* **119,** 24201–24228 (2015).

32. Strandwitz, N. C., Comstock, D. J., Grimm, R. L., Nichols-Nielander, A. C., Elam, J. & Lewis, N. S. Photoelectrochemical Behavior of n-type Si(100) Electrodes Coated with Thin Films of Manganese Oxide Grown by Atomic Layer Deposition. *Journal of Physical Chemistry C* **117,** 4931–4936 (2013).

33. Fan, F. R. F., Keil, R. G. & Bard, A. J. Semiconductor Electrodes .48. Photo-Oxidation of Halides and Water on N-Silicon Protected with Silicide Layers. *Journal of the American Chemical Society* **105,** 220–224 (1983).

34. Chen, Y. W., Prange, J. D., Duhnen, S., Park, Y., Gunji, M., Chidsey, C. E. D. & McIntyre, P. C. Atomic layer-deposited tunnel oxide stabilizes silicon photoanodes for water oxidation. *Nature Materials* **10,** 539–544 (2011).

35. Lin, G. H., Kapur, M., Kainthla, R. C. & Bockris, J. O. One step method to produce hydrogen by a triple stack amorphous silicon solar cell. *Applied Physics Letters* **55,** 386 (1989).

36. Appleby, A. J., Delahoy, A. E., Gau, S. C., Murphy, O. J., Kapur, M. & Bockris, J. O. M. An Amorphous Silicon-Based One-Unit Photovoltaic Electrolyzer. *Energy* **10,** 871–876 (1985).

37. Appleby, J. A. *Photocell device for evolving hydrogen and oxygen from water* Patent. 1987.

38. Bolton, J. R., Strickler, S. J. & Connolly, J. S. Limiting and Realizable Efficiencies of Solar Photolysis of Water. *Nature* **316,** 495–500 (1985).

39. Jin, J., Walczak, K., Singh, M. R., Karp, C., Lewis, N. S. & Xiang, C. X. An experimental and modeling/simulation-based evaluation of the efficiency and operational performance characteristics of an integrated, membrane-free, neutral pH solar-driven water-splitting system. *Energy & Environmental Science* **7,** 3371–3380 (2014).

40. Singh, M. R., Papadantonakis, K. M., Xiang, C. & Lewis, N. An Electrochemical Engineering Assessment of the Operational Conditions and Constraints for Solar-Driven Water-Splitting Systems at Near-Neutral pH. *Energy & Environmental Science* (2015).

41. Reece, S. Y., Hamel, J. A., Sung, K., Jarvi, T. D., Esswein, A. J., Pijpers, J. J. H. & Nocera, D. G. Wireless Solar Water Splitting Using Silicon-Based Semiconductors and Earth-Abundant Catalysts. *Science* **334,** 645–648 (2011).

42. Suzuki, O., Takahashi, M., Fukunaga, T. & Kuboyama, J. *Novel cobalt oxide and an electrode having the cobalt oxide coating* Patent. 1968.

43. Shafirovich, V. Y. & Strelets, V. V. Catalytic-Oxidation of Water by Cobalt Complexes. *Nouveau Journal De Chimie-New Journal of Chemistry* **2,** 199–201 (1978).

44. Elizarova, G. L., Zhidomirov, G. M. & Parmon, V. N. Hydroxides of transition metals as artificial catalysts for oxidation of water to dioxygen. *Catalysis Today* **58,** 71–88 (2000).

45. Reece, S., Esswein, A., Sung, K., Green, Z. & Nocera, D. *Compositions, electrodes, methods, and systems for water electrolysis and other electrochemical techniques* Patent. 2011.

46. Minguzzi, A., Fan, F.-R. F., Vertova, A., Rondinini, S. & Bard, A. J. Dynamic potential–pH diagrams application to electrocatalysts for wateroxidation. *Chem. Sci.* **3,** 217–229 (2012).

47. Bediako, D. K., Costentin, C., Jones, E. C., Nocera, D. G. & Saveant, J. M. Proton-Electron Transport and Transfer in Electrocatalytic Films. Application to a Cobalt-Based O_2-Evolution Catalyst. *Journal of the American Chemical Society* **135,** 10492–10502 (2013).

48. Bard, A. J. & Faulkner, L. R. *Electrochemical Methods: Fundamentals and Applications, 2nd Edition* (2000).

49. Hernandez-Pagan, E. A., Vargas-Barbosa, N. M., Wang, T. H., Zhao, Y. X., Smotkin, E. S. & Mallouk, T. E. Resistance and polarization losses in aqueous buffer-membrane electrolytes for water-splitting photoelectrochemical cells. *Energy & Environmental Science* **5,** 7582–7589 (2012).

50. Miller, E. L., Rocheleau, R. E. & Deng, X. M. Design considerations for a hybrid amorphous silicon/photoelectrochemical multijunction cell for hydrogen production. *International Journal of Hydrogen Energy* **28,** 615–623 (2003).

51. McCrory, C. C. L., Jung, S., Peters, J. C. & Jaramillo, T. F. Benchmarking Heterogeneous Electrocatalysts for the Oxygen Evolution Reaction. *Journal of the American Chemical Society* **135,** 16977–16987 (2013).

52. Weber, A. Z. & Newman, J. Transport in polymer-electrolyte membranes - III. Model validation in a simple fuel-cell model. *Journal of the Electrochemical Society* **151,** A326–A339 (2004).

53. Yamada, Y., Matsukia, N., Ohmoria, T., Mametsukaa, H., Kondob, M., Matsudab, A. & Suzukia, E. One chip photovoltaic water electrolysis device. *International Journal of Hydrogen Energy* **28,** 1167–1169 (2003).

54. Kelly, N. & Gibson, T. Design and characterization of a robust photoelectrochemical device to generate hydrogen using solar water splitting. *International Journal of Hydrogen Energy* **31,** 1658–1673 (2006).

55. Miller, E. L., Paluselli, D., Marsen, B. & Rocheleau, R. E. Development of reactively sputtered metal oxide films for hydrogen-producing hybrid multijunction photoelectrodes. *Solar Energy Materials and Solar Cells* **88,** 131–144 (2005).

56. Khaselev, O. & Turner, J. A. A Monolithic Photovoltaic-Photoelectrochemical Device for Hydrogen Production via Water Splitting. *Science* **280,** 425–427 (1998).

57. Pourbaix, M. *Atlas of Electrochemical Equilibria in Aqueous Solutions* 2nd ed. (National Association of Corrosion Engineers, TX, 1974).

58. Walter, M. G., Warren, E. L., McKone, J. R., Boettcher, S. W., Mi, Q. X., Santori, E. A. & Lewis, N. S. Solar Water Splitting Cells. *Chemical Reviews* **110,** 6446–6473 (2010).

59. Kocha, S. S., Montgomery, D., Peterson, M. W. & Turner, J. A. Photoelectrochemical decomposition of water utilizing monolithic tandem cells. *Solar Energy Materials and Solar Cells* **52,** 389–397 (1998).

60. May, M. M., Lewerenz, H. J., Lackner, D., Dimroth, F. & Hannappel, T. Efficient direct solar-to-hydrogen conversion by in situ interface transformation of a tandem structure. *Nature Communications* **6** (2015).

61. Kumar, B., Llorente, M., Froehlich, J., Dang, T., Sathrum, A. & Kubiak, C. P. Photochemical and Photoelectrochemical Reduction of CO2. *Annual Review of Physical Chemistry, Vol 63* **63,** 541–+ (2012).

62. Hori, Y., Wakebe, H., Tsukamoto, T. & Koga, O. Electrocatalytic Process of Co Selectivity in Electrochemical Reduction of Co2 at Metal-Electrodes in Aqueous-Media. *Electrochimica Acta* **39,** 1833–1839 (1994).

63. Min, X. Q. & Kanan, M. W. Pd-Catalyzed Electrohydrogenation of Carbon Dioxide to Formate: High Mass Activity at Low Overpotential and Identification of the Deactivation Pathway. *Journal of the American Chemical Society* **137,** 4701–4708 (2015).

64. Schreier, M., Curvat, L., Giordano, F., Steier, L., Abate, A., Zakeeruddin, S. M., Luo, J. S., Mayer, M. T. & Gratzel, M. Efficient photosynthesis of carbon monoxide from CO2 using perovskite photovoltaics. *Nature Communications* **6** (2015).

65. Asadi, M., Kumar, B., Behranginia, A., Rosen, B. A., Baskin, A., Repnin, N., Pisasale, D., Phillips, P., Zhu, W., Haasch, R., Klie, R. F., Kral, P., Abiade, J. & Salehi-Khojin, A. Robust carbon dioxide reduction on molybdenum disulphide edges. *Nature Communications* **5** (2014).

66. Asadi, M., Kim, K., Liu, C., Addepalli, A. V., Abbasi, P., Yasaei, P., Phillips, P., Behranginia, A., Cerrato, J. M., Haasch, R., Zapol, P., Kumar, B., Klie, R. F., Abiade, J., Curtiss, L. A. & Salehi-Khojin, A. Nanostructured transition metal dichalcogenide electrocatalysts for CO2 reduction in ionic liquid. *Science* **353,** 467–470 (2016).

67. Zhang, B., Zheng, X. L., Voznyy, O., Comin, R., Bajdich, M., Garcia-Melchor, M., Han, L. L., Xu, J. X., Liu, M., Zheng, L. R., de Arquer, F. P. G., Dinh, C. T., Fan, F. J., Yuan, M. J., Yassitepe, E., Chen, N., Regier, T., Liu, P. F., Li, Y. H., De Luna, P., Janmohamed, A., Xin, H. L. L., Yang, H. G., Vojvodic, A. & Sargent, E. H. Homogeneously dispersed multimetal oxygen-evolving catalysts. *Science* **352,** 333–337 (2016).

68. McCrory, C. C. L., Jung, S., Ferrer, I. M., Chatman, S. M., Peters, J. C. & Jaramillo, T. F. Benchmarking Hydrogen Evolving Reaction and Oxygen Evolving Reaction Electrocatalysts for Solar Water Splitting Devices. *Journal of the American Chemical Society* **137,** 4347–4357 (2015).

69. Xiang, C. X., Papadantonakis, K. M. & Lewis, N. S. Principles and implementations of electrolysis systems for water splitting. *Materials Horizons* **3,** 169–173 (2016).

70. Arai, T., Sato, S. & Morikawa, T. A monolithic device for CO_2 photoreduction to generate liquid organic substances in a single-compartment reactor. *Energy & Environmental Science* **8,** 1998–2002 (2015).

71. Jeon, H. S., Koh, J. H., Park, S. J., Jee, M. S., Ko, D. H., Hwang, Y. J. & Min, B. K. A monolithic and standalone solar-fuel device having comparable efficiency to photosynthesis in nature. *Journal of Materials Chemistry A* **3,** 5835–5842 (2015).

72. Sugano, Y., Ono, A., Kitagawa, R., Tamura, J., Yamagiwa, M., Kudo, Y., Tsutsumi, E. & Mikoshiba, S. Crucial role of sustainable liquid junction potential for solar-to-carbon monoxide conversion by a photovoltaic photoelectrochemical system. *Rsc Advances* **5,** 54246–54252 (2015).

73. Kohl, P. A., Frank, S. N. & Bard, A. J. Semiconductor Electrodes .11. Behavior of N-Type and P-Type Single-Crystal Semiconductors Covered with Thin Normal-Tio_2 Films. *Journal of the Electrochemical Society* **124,** 225–229 (1977).

74. Lin, Y. J., Kapadia, R., Yang, J. H., Zheng, M., Chen, K., Hettick, M., Yin, X. T., Battaglia, C., Sharp, I. D., Ager, J. W. & Javey, A. Role of TiO_2 Surface Passivation on Improving the Performance of p-InP Photocathodes. *Journal of Physical Chemistry C* **119,** 2308–2313 (2015).

75. Qiu, J., Zeng, G. T., Ha, M. A., Ge, M. Y., Lin, Y. J., Hettick, M., Hou, B. Y., Alexandrova, A. N., Javey, A. & Cronin, S. B. Artificial Photosynthesis on TiO_2-Passivated InP Nanopillars. *Nano Letters* **15,** 6177–6181 (2015).

76. Scheuermann, A. G., Prange, J. D., Gunji, M., Chidsey, C. E. D. & McIntyre, P. C. Effects of catalyst material and atomic layer deposited TiO_2 oxide thickness on the water oxidation performance of metal-insulator-silicon anodes. *Energy & Environmental Science* **6,** 2487–2496 (2013).

77. Seger, B., Pedersen, T., Laursen, A. B., Vesborg, P. C. K., Hansen, O. & Chorkendorff, I. Using TiO_2 as a Conductive Protective Layer for Photocathodic H_2 Evolution. *Journal of the American Chemical Society* **135,** 1057–1064 (2013).

78. Hu, S., Shaner, M. R., Beardslee, J. A., Lichterman, M., Brunschwig, B. S. & Lewis, N. S. Amorphous TiO_2 coatings stabilize Si, GaAs, and GaP photoanodes for efficient water oxidation. *Science* **344,** 1005–1009 (2014).

79. Lichterman, M. F., Carim, A. I., McDowell, M. T., Hu, S., Gray, H. B., Brunschwig, B. S. & Lewis, N. S. Stabilization of n-cadmium telluride photoanodes for water oxidation to O_2(g) in aqueous alkaline electrolytes using amorphous TiO_2 films formed by atomic-layer deposition. *Energy & Environmental Science* **7,** 3334–3337 (2014).

80. Shaner, M. R., Hu, S., Sun, K. & Lewis, N. S. Stabilization of Si microwire arrays for solar-driven H_2O oxidation to O_2(g) in 1.0 M KOH(aq) using conformal coatings of amorphous TiO_2. *Energy & Environmental Science* **8,** 203–207 (2015).

81. Hu, S., Xiang, C. X., Haussener, S., Berger, A. D. & Lewis, N. S. An analysis of the optimal band gaps of light absorbers in integrated tandem photoelectrochemical water-splitting systems. *Energy & Environmental Science* **6,** 2984–2993 (2013).

82. Konagai, M., Sugimoto, M. & Takahashi, K. High-Efficiency GaAs Thin-Film Solar-Cells by Peeled Film Technology. *Journal of Crystal Growth* **45,** 277–280 (1978).

83. Yablonovitch, E., Gmitter, T., Harbison, J. P. & Bhat, R. Extreme Selectivity in the Lift-Off of Epitaxial GaAs Films. *Applied Physics Letters* **51,** 2222–2224 (1987).

84. Schermer, J. J., Mulder, P., Bauhuis, G. J., Voncken, M. M. A. J., van Deelen, J., Haverkamp, E. & Larsen, P. K. Epitaxial Lift-Off for large area thin film III/V devices. *Physica Status Solidi A - Applications and Materials Science* **202,** 501–508 (2005).

85. Tatavarti, R., Wibowo, A., Martin, G., Tuminello, F., Youtsey, C., Hillier, G., Pan, N., Wanlass, M. W. & Romero, M. InGaP/GaAs / InGaAs INVERTED METAMORPHIC (IMM) SOLAR CELLS ON 4 " EPITAXIAL LIFTED OFF (ELO) WAFERS. *35th IEEE Photovoltaic Specialists Conference,* 2125–2128 (2010).

86. Nakayama, K., Tanabe, K. & Atwater, H. A. Improved electrical properties of wafer-bonded p-GaAs/n-InP interfaces with sulfide passivation. *Journal of Applied Physics* **103** (2008).

87. Green, M. A., Emery, K., Hishikawa, Y., Warta, W. & Dunlop, E. D. Solar cell efficiency tables (Version 45). *Progress in Photovoltaics: Research and Applications* **23,** 1–9 (2015).

88. Orfanidis, S. J. *Electromagnetic Waves and Antennas* <http://www.ece.rutgers.edu/~orfanidi/ewa/> (2014).

89. McDowell, M. T., Lichterman, M. F., Carim, A. I., Liu, R., Hu, S., Brunschwig, B. S. & Lewis, N. S. The Influence of Structure and Processing on the Behavior of TiO_2 Protective Layers for Stabilization of n-Si/TiO_2/Ni Photoanodes for Water Oxidation. *ACS Applied Materials and Interfaces* **7,** 15189–15199 (2015).

90. Mei, B., Pedersen, T., Malacrida, P., Bae, D., Frydendal, R., Hansen, O., Vesborg, P. C. K., Seger, B. & Chorkendorff, I. Crystalline TiO_2: A Generic and Effective Electron-Conducting Protection Layer for Photoanodes and -cathodes. *The Journal of Physical Chemistry C* **119,** 15019–15027 (2015).

91. Lichterman, M. F., Hu, S., Richter, M. H., Crumlin, E. J., Axnanda, S., Favaro, M., Drisdell, W., Hussain, Z., Mayer, T., Brunschwig, B. S., Lewis, N. S., Liu, Z. & Lewerenz, H. J. Direct observation of the energetics at a semiconductor/liquid junction by operando X-ray photoelectron spectroscopy. *Energy & Environmental Science* **8,** 2409–2416 (2015).

92. Nunez, P., Roske, C., Richter, M., Piercy, B., Losego, M., Konezny, S. J., Hu, S., Brunschwig, B. S. & Lewis, N. S. Electronic Transport Through Amorphous ALD TiO2. *Submission Pending* (2017).

93. Trotochaud, L., Young, S. L., Ranney, J. K. & Boettcher, S. W. Nickel-Iron Oxyhydroxide Oxygen-Evolution Electrocatalysts: The Role of Intentional and Incidental Iron Incorporation. *Journal of the American Chemical Society* **136,** 6744–6753 (2014).

94. Chen, Y. K., Sun, K., Audesirk, H., Xiang, C. X. & Lewis, N. S. A quantitative analysis of the efficiency of solar-driven water-splitting device designs based on tandem photoabsorbers patterned with islands of metallic electrocatalysts. *Energy & Environmental Science* **8,** 1736–1747 (2015).

95. McKone, J. R., Sadtler, B. F., Werlang, C. A., Lewis, N. S. & Gray, H. B. Ni–Mo Nanopowders for Efficient Electrochemical Hydrogen Evolution. *ACS Catalysis* **3,** 166–169 (2012).

96. Warren, E. L., McKone, J. R., Atwater, H. A., Gray, H. B. & Lewis, N. S. Hydrogen-evolution characteristics of Ni-Mo-coated, radial junction, n(+)p-silicon microwire array photocathodes. *Energy & Environmental Science* **5,** 9653–9661 (2012).

97. Walczak, K., Chen, Y. K., Karp, C., Beeman, J. W., Shaner, M., Spurgeon, J., Sharp, I. D., Amashukeli, X., West, W., Jin, J., Lewis, N. S. & Xiang, C. X. Modeling, Simulation, and Fabrication of a Fully Integrated, Acid-stable, Scalable Solar-Driven Water-Splitting System. *Chemsuschem* **8,** 544–551 (2015).

98. Sathre, R., Greenblatt, J. B., Walczak, K., Sharp, I. D., Stevens, J. C., Ager, J. W. & Houle, F. A. Opportunities to improve the net energy performance of photoelectrochemical water-splitting technology. *Energy & Environmental Science* **9,** 803–819 (2016).

99. Sun, K., Moreno-Hernandez, I. A., Schmidt, W. C., Zhou, X., Crompton, J. C., Liu, R., Saadi, F. H., Papadantonakis, K. M., Brunschwig, B. S. & Lewis, N. S. A Comparison of the Chemical, Optical and Electrocatalytic Properties of Water-Oxidation Catalysts for Use in Integrated Solar-Fuels Generators. *Submitted for Publication* (2017).

100. Sun, K., Saadi, F. H., Lichterman, M. F., Hale, W. G., Wang, H. P., Zhou, X., Plymale, N. T., Omelchenko, S. T., He, J. H., Papadantonakis, K. M., Brunschwig, B. S. & Lewis, N. S. Stable solar-driven oxidation of water by semiconducting photoanodes protected by transparent catalytic nickel oxide films. *Proc Natl Acad Sci U S A* **112,** 3612–7 (2015).

101. Chen, Y. K., Xiang, C. X., Hu, S. & Lewis, N. S. Modeling the Performance of an Integrated Photoelectrolysis System with 10 x Solar Concentrators. *Journal of the Electrochemical Society* **161,** F1101–F1110 (2014).

102. Xiang, C. X., Chen, Y. K. & Lewis, N. S. Modeling an integrated photoelectrolysis system sustained by water vapor. *Energy & Environmental Science* **6,** 3713–3721 (2013).

103. Ayers, K. E., Anderson, E. B., Capuano, C. B., Carter, B. D., Dalton, L. T., Hanlon, G., Manco, J. & Niedzwiecki, M. Research Advances Towards Low Cost, High Efficiency PEM Electrolysis. *Polymer Electrolyte Fuel Cells 10, Pts 1 and 2* **33,** 3–15 (2010).

104. Geum, D. M., Park, M. S., Lim, J. Y., Yang, H. D., Song, J. D., Kim, C. Z., Yoon, E., Kim, S. & Choi, W. J. Ultra-high-throughput Production of III-V/Si Wafer for Electronic and Photonic Applications. *Scientific Reports* **6.** doi:ARTN2061010.1038/srep20610 (2016).

105. Jain, N. & Hudait, M. K. Design and Modeling of Metamorphic Dual-Junction InGaP/GaAs Solar Cells on Si Substrate for Concentrated Photovoltaic Application. *IEEE Journal of Photovoltaics* **4,** 1683–1689 (2014).

106. Hu, S., Chi, C. Y., Fountaine, K. T., Yao, M. Q., Atwater, H. A., Dapkus, P. D., Lewis, N. S. & Zhou, C. W. Optical, electrical, and solar energy-conversion properties of gallium arsenide nanowire-array photoanodes. *Energy & Environmental Science* **6,** 1879–1890 (2013).

107. Hu, S., Yao, M., Sun, K., Chi, C. Y., Lichterman, M., Zhou, C., Dapkus, P. D. & Lewis, N. S. TiO2-Protected, Defect-Tolerant, Tandem GaAs Nanowire Array/Planar Si Photoanodes for Water Oxidation. *Submitted for Publication* (2017).

108. McDonald, M. B., Ardo, S., Lewis, N. S. & Freund, M. S. Use of Bipolar Membranes for Maintaining Steady-State pH Gradients in Membrane-Supported, Solar-Driven Water Splitting Michael. *Chemsuschem* **7,** 3021–3027 (2014).

109. Unlu, M., Zhou, J. F. & Kohl, P. A. Hybrid Anion and Proton Exchange Membrane Fuel Cells. *Journal of Physical Chemistry C* **113,** 11416–11423 (2009).

110. Vermaas, D. A., Sassenburg, M. & Smith, W. A. Photo-assisted water splitting with bipolar membrane induced pH gradients for practical solar fuel devices. *Journal of Materials Chemistry A* **3,** 19556–19562 (2015).

111. Saadi, F. H., Carim, A. I., Verlage, E., Hemminger, J. C., Lewis, N. S. & Soriaga, M. P. CoP as an Acid-Stable Active Electrocatalyst for the Hydrogen-Evolution Reaction: Electrochemical Synthesis, Interfacial Characterization and Performance Evaluation. *The Journal of Physical Chemistry C* **118,** 29294–29300 (2014).

112. Fountaine, K. T., Kendall, C. G. & Atwater, H. A. Near-unity broadband absorption designs for semiconducting nanowire arrays via localized radial mode excitation. *Optics Express* **22,** A930–A940 (2014).

113. Ding, Y. & Magnusson, R. Band gaps and leaky-wave effects in resonant photonic-crystal waveguides. *Optics Express* **15,** 680–694 (2007).

114. Fountaine, K. T., Whitney, W. S. & Atwater, H. A. Resonant absorption in semiconductor nanowires and nanowire arrays: Relating leaky waveguide modes to Bloch photonic crystal modes. *Journal of Applied Physics* **116** (2014).

115. Sturmberg, B. C. P., Dossou, K. B., Botten, L. C., Asatryan, A. A., Poulton, C. G., McPhedran, R. C. & de Sterke, C. M. Optimizing Photovoltaic Charge Generation of Nanowire Arrays: A Simple Semi-Analytic Approach. *Acs Photonics* **1,** 683–689 (2014).

116. Jeong, S., Garnett, E. C., Wang, S., Yu, Z. G., Fan, S. H., Brongersma, M. L., McGehee, M. D. & Cui, Y. Hybrid Silicon Nanocone-Polymer Solar Cells. *Nano Letters* **12,** 2971–2976 (2012).

117. Kapadia, R., Fan, Z. Y., Takei, K. & Javey, A. Nanopillar photovoltaics: Materials, processes, and devices. *Nano Energy* **1,** 132–144 (2012).

118. Narasimhan, V. K., Hymel, T. M., Lai, R. A. & Cui, Y. Hybrid Metal-Semiconductor Nanostructure for Ultrahigh Optical Absorption and Low Electrical Resistance at Optoelectronic Interfaces. *Acs Nano* **9,** 10590–10597 (2015).

119. Garnett, E. & Yang, P. D. Light Trapping in Silicon Nanowire Solar Cells. *Nano Letters* **10,** 1082–1087 (2010).

120. Tian, B. Z., Zheng, X. L., Kempa, T. J., Fang, Y., Yu, N. F., Yu, G. H., Huang, J. L. & Lieber, C. M. Coaxial silicon nanowires as solar cells and nanoelectronic power sources. *Nature* **449,** 885–U8 (2007).

121. Wallentin, J., Anttu, N., Asoli, D., Huffman, M., Aberg, I., Magnusson, M. H., Siefer, G., Fuss-Kailuweit, P., Dimroth, F., Witzigmann, B., Xu, H. Q., Samuelson, L., Deppert, K. & Borgstrom, M. T. InP Nanowire Array Solar Cells Achieving 13.8% Efficiency by Exceeding the Ray Optics Limit. *Science* **339,** 1057–1060 (2013).

122. Mavrokefalos, A., Han, S. E., Yerci, S., Branham, M. S. & Chen, G. Efficient Light Trapping in Inverted Nanopyramid Thin Crystalline Silicon Membranes for Solar Cell Applications. *Nano Letters* **12,** 2792–2796 (2012).

123. Zhu, J., Hsu, C. M., Yu, Z. F., Fan, S. H. & Cui, Y. Nanodome Solar Cells with Efficient Light Management and Self-Cleaning. *Nano Letters* **10,** 1979–1984 (2010).

124. Yao, Y., Yao, J., Narasimhan, V. K., Ruan, Z. C., Xie, C., Fan, S. H. & Cui, Y. Broadband light management using low-Q whispering gallery modes in spherical nanoshells. *Nature Communications* **3.** doi:ARTN66410.1038/ncomms1664 (2012).

125. Grandidier, J., Callahan, D. M., Munday, J. N. & Atwater, H. A. Light Absorption Enhancement in Thin-Film Solar Cells Using Whispering Gallery Modes in Dielectric Nanospheres. *Advanced Materials* **23,** 1272–+ (2011).

126. Saive, R., Bukowsky, C. R. & Atwater, H. A. Three-dimensional nanoimprint lithography using two-photon lithography master samples. *arXiv.org - Mesoscale and Nanoscale Physics* **arXiv:1702.04012** (2017).

127. Ebbesen, T. W., Lezec, H. J., Ghaemi, H. F., Thio, T. & Wolff, P. A. Extraordinary optical transmission through sub-wavelength hole arrays. *Nature* **391,** 667–669 (1998).

128. Ghaemi, H. F., Thio, T., Grupp, D. E., Ebbesen, T. W. & Lezec, H. J. Surface plasmons enhance optical transmission through subwavelength holes. *Physical Review B* **58,** 6779–6782 (1998).

129. Burgos, S. P., Yokogawa, S. & Atwater, H. A. Color Imaging via Nearest Neighbor Hole Coupling in Plasmonic Color Filters Integrated onto a Complementary Metal-Oxide Semiconductor Image Sensor. *Acs Nano* **7,** 10038–10047 (2013).

130. Bravo-Abad, J., Degiron, A., Przybilla, F., Genet, C., Garcia-Vidal, F. J., Martin-Moreno, L. & Ebbesen, T. W. How light emerges from an illuminated array of subwavelength holes. *Nature Physics* **2,** 120–123 (2006).

131. Awazu, K., Wang, X. M., Fujimaki, M., Kuriyama, T., Sai, A., Ohki, Y. & Imai, H. Fabrication of two- and three-dimensional photonic crystals of titania with submicrometer resolution by deep x-ray lithography. *Journal of Vacuum Science & Technology B* **23,** 934–939 (2005).

132. Takamoto, T., Ikeda, E., Kurita, H. & Ohmori, M. Over 30% efficient InGaP/GaAs tandem solar cells. *Applied Physics Letters* **70,** 381–383 (1997).

133. Homier, R., Jaouad, A., Turala, A., Valdivia, C. E., Masson, D., Wallace, S. G., Fafard, S., Ares, R. & Aimez, V. Antireflection Coating Design for Triple-Junction III-V/Ge High-Efficiency Solar Cells Using Low Absorption PECVD Silicon Nitride. *Ieee Journal of Photovoltaics* **2,** 393–397 (2012).

134. Eriksen, G. F. & Dyrbye, K. Protective coatings in harsh environments. *Journal of Micromechanics and Microengineering* **6,** 55–57 (1996).

135. Saive, R., Borsuk, A. M., Emmer, H. S., Bukowsky, C. R., Lloyd, J. V., Yalamanchili, S. & Atwater, H. A. Effectively Transparent Front Contacts for Optoelectronic Devices. *Advanced Optical Materials* **4,** 1470–1474 (2016).

136. Norasetthekul, S., Park, P. Y., Baik, K. H., Lee, K. P., Shin, J. H., Jeong, B. S., Shishodia, V., Lambers, E. S., Norton, D. P. & Pearton, S. J. Dry etch chemistries for TiO2 thin films. *Applied Surface Science* **185,** 27–33 (2001).

137. Choi, J. H., Jo, H. B., Choi, H. J. & Lee, H. Fabrication of TiO2 nano-to-microscale structures using UV nanoimprint lithography. *Nanotechnology* **24.** doi:Artn19530110.1088/0957-4484/24/19/195301 (2013).

138. Hsu, C. M., Connor, S. T., Tang, M. X. & Cui, Y. Wafer-scale silicon nanopillars and nanocones by Langmuir-Blodgett assembly and etching. *Applied Physics Letters* **93.** doi:Artn13310910.1063/1.2988893 (2008).

139. Yu, Z. N., Gao, H., Wu, W., Ge, H. X. & Chou, S. Y. Fabrication of large area subwavelength antireflection structures on Si using trilayer resist nanoimprint lithography and liftoff. *Journal of Vacuum Science & Technology B* **21,** 2874–2877 (2003).

140. Devlin, R. C., Khorasaninejad, M., Chen, W. T., Oh, J. & Capasso, F. Broadband high-efficiency dielectric metasurfaces for the visible spectrum. *Proceedings of the National Academy of Sciences of the United States of America* **113,** 10473–10478 (2016).

141. Barbe, J., Thomson, A. F., Wang, E. C., McIntosh, K. & Catchpole, K. Nanoimprinted TiO2 sol-gel passivating diffraction gratings for solar cell applications. *Progress in Photovoltaics* **20,** 143–148 (2012).

142. Park, H. H., Zhang, X., Lee, S. W., Jeong, D. J., Lee, S. M., Kim, K. D., Choi, D. G., Choi, J. H., Lee, J., Lee, E. S., Kang, H. K., Park, H. H., Hill, R. H. & Jeong, J. H. Optical characterization of anatase TiO2 films patterned by direct ultraviolet-assisted nanoimprint lithography. *Microelectronic Engineering* **88,** 923–928 (2011).

143. Liu, B. & Aydil, E. S. Growth of Oriented Single-Crystalline Rutile TiO2 Nanorods on Transparent Conducting Substrates for Dye-Sensitized Solar Cells. *Journal of the American Chemical Society* **131,** 3985–3990 (2009).

144. Ryan, C. G. M. & Eleftheriades, G. V. Single- and Dual-Band Transparent Circularly Polarized Patch Antennas With Metamaterial Loading. *Ieee Antennas and Wireless Propagation Letters* **14,** 470–473 (2015).

145. Ellmer, K. Past achievements and future challenges in the development of optically transparent electrodes. *Nature Photonics* **6,** 808–816 (2012).

146. Liu, J., Buchholz, D. B., Hennek, J. W., Chang, R. P. H., Facchetti, A. & Marks, T. J. All-Amorphous-Oxide Transparent, Flexible Thin-Film Transistors. Efficacy of Bilayer Gate Dielectrics. *Journal of the American Chemical Society* **132,** 11934–11942 (2010).

147. Yang, Y., Jeong, S., Hu, L. B., Wu, H., Lee, S. W. & Cui, Y. Transparent lithium-ion batteries. *Proceedings of the National Academy of Sciences of the United States of America* **108,** 13013–13018 (2011).

INDEX